Preparing and characterizing quantum states of light using photon-number-resolving detectors

Guillaume Suresh Thekkadath
Oriel College, Oxford

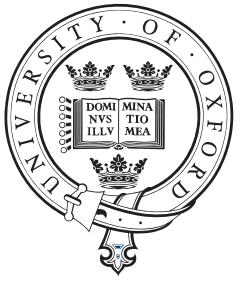

Submitted for the degree of Doctor of Philosophy

Trinity Term 2020

Supervised by
Prof. A. I. Lvovksy
Prof. I. A. Walmsley
Dr. R. B. Patel

Clarendon Laboratory
University of Oxford

Abstract

A longstanding goal in quantum optics has been to realize a photon-number-resolving detector that efficiently counts the number of photons in an optical field. This goal has been largely met with the development of transition edge sensors which can count up to roughly 20 photons with efficiencies over 95%. This thesis presents three experiments that employ these detectors to characterize and prepare quantum states of light.

Firstly, we develop a weak-field homodyne detector. By replacing the photodiodes conventionally used in homodyne detection with transition edge sensors, we experimentally implement a versatile measurement device that can tune between photon counting and quadrature measurements. We study the transition between these complementary measurement regimes and determine the minimum local oscillator strength needed to perform quadrature measurements.

Secondly, we use the weak-field homodyne detector as a quantum state engineering tool. We propose a scheme to prepare a wide range of definite parity states, including two- and four-component Schrödinger cat states of arbitrary size with nearly perfect fidelity.

Thirdly, we perform optical interferometry using quantum states of light with the aim of surpassing the maximal precision achievable with classical light, i.e. the shot-noise limit. We propose and experimentally implement a scheme that uses high-gain squeezed vacuum sources and transition edge sensors to prepare loss-tolerant entangled states containing up to 8 photons. While our achieved precision does not unconditionally (i.e. without post-selecting on certain measurement trials) surpass the shot-noise limit, our results do demonstrate the robustness of these entangled states to loss despite their size.

Acknowledgements

I gratefully acknowledge funding from the University of Oxford, Oriel College, and the Natural Sciences and Engineering Research Council of Canada.

I thank my supervisors, Prof. Ian Walmsley and Prof. Alex Lvovsky, who have both helped me become a better scientist. It was a pleasure to work in Ian's Ultrafast group which is rich in expertise and has an abundance of lab equipment. I am also grateful to Alex for agreeing to supervise me later in my DPhil. His guidance has been very helpful.

I worked with excellent colleagues and I thank all my co-authors. Notably, Dr. Chris Wade, Dr. Bryn Bell, and Dr. Raj Patel ensured the smooth progression of my DPhil, and I thank them for their patience and day-to-day supervision.

I wrote this thesis during the rather unusual time of the COVID-19 pandemic. Luckily, I was at home with my family. I am most grateful to my parents and my brother for their love, support, and encouragement.

List of publications

I was involved in the following publications during my DPhil. This thesis focuses on the first three.

1. G.S. Thekkadath, M.E. Mycroft, B.A. Bell, C.G. Wade, A. Eckstein, D.S. Phillips, R.B. Patel, A. Buraczewski, A.E. Lita, T. Gerrits, S.W. Nam, M. Stobinska, A.I. Lvovsky, I.A. Walmsley, "Quantum-enhanced interferometry with large heralded photon-number states", *npj Quantum Inf.* **6** 89 (2020).

2. G.S. Thekkadath, B.A. Bell, I.A. Walmsley, A.I. Lvovsky, "Engineering Schrödinger cat states with a photonic even-parity detector", *Quantum* **4** 239 (2020).

3. G.S. Thekkadath, D.S. Phillips, J.F.F. Bulmer, W.R. Clements, A. Eckstein, B.A. Bell, J. Lugani, T.A.W. Wolterink, A. Lita, S.W. Nam, T. Gerrits, C.G. Wade, I.A. Walmsley, "Tuning between photon-number and quadrature measurements using weak-field homodyne detection", *Phys. Rev. A* **101** 031801(R) (2020).

4. J. Sperling, D.S. Phillips, J.F.F. Bulmer, G. S. Thekkadath, A. Eckstein, T.A.W. Wolterink, J. Lugani, S.W. Nam, A. Lita, T. Gerrits, W. Vogel, G. S. Agarwal, C. Silberhorn, I.A. Walmsley "Detector-Agnostic Phase-Space Distributions", *Phys. Rev. Lett.* **124** 013605 (2020).

5. B.A. Bell, G.S. Thekkadath, R. Ge, X. Cai, I.A. Walmsley "Testing multiphoton interference on a silicon chip", *Opt. Express* **27** 35646 (2019).

6. G.S. Thekkadath, F. Hufnagel, J.S. Lundeen, "Determining complementary properties using weak-measurement: uncertainty, predictability, and disturbance", *New J. Phys.* **20** 113034 (2018).

7. K.T. Kaczmarek, P.M. Ledingham, B. Brecht, S.E. Thomas, G.S. Thekkadath, O. Lazo-Arjona, J.H.D. Munns, E. Poem, A. Feizpour, D.J. Saunders, J. Nunn, I.A. Walmsley, "High-speed noise-free optical quantum memory", *Phys. Rev. A* **97** 042316 (2018).

Author contributions

The work presented in Chapter 3 has been presented in the following paper:

- G.S. Thekkadath, D.S. Phillips, J.F.F. Bulmer, W.R. Clements, A. Eckstein, B.A. Bell, J. Lugani, T.A.W. Wolterink, A. Lita, S.W. Nam, T. Gerrits, C.G. Wade, I.A. Walmsley, "Tuning between photon-number and quadrature measurements using weak-field homodyne detection", *Phys. Rev. A* **101** 031801(R) (2020).

The project was initiated by W.R. Clements. D.S. Phillips and J.F.F. Bulmer operated the detectors while I built the sources with help from D.S. Phillips. I developed the theory model with help from D.S. Phillips and C.G. Wade. I wrote the manuscript with help from D.S. Phillips and input from all the authors.

The work presented in Chapter 4 has been presented in the following paper:

- G.S. Thekkadath, B.A. Bell, I.A. Walmsley, A.I. Lvovsky, "Engineering Schrödinger cat states with a photonic even-parity detector", *Quantum* **4** 239 (2020).

I initiated the project. The concept of the even-parity detector was developed by A.I. Lvovsky and me. B.A. Bell had the idea of concatenating the even-parity detector. I wrote the manuscript with input from all the authors.

The work presented in Chapter 5 has been presented in the following paper:

- G.S. Thekkadath, M.E. Mycroft, B.A. Bell, C.G. Wade, A. Eckstein, D.S. Phillips, R.B. Patel, A. Buraczewski, A.E. Lita, T. Gerrits, S.W. Nam, M. Stobinska, A.I. Lvovsky, I.A. Walmsley, "Quantum-enhanced interferometry with large heralded photon-number states", *npj Quantum Inf.* **6** 89 (2020).

The project was initiated by M. Stobinska and I.A. Walmsley. I performed the experiment with help from B.A. Bell and D.S. Phillips. I developed the theory model to fit the data. M.E. Mycroft calculated the curves in Fig. 5.3(b). I wrote the manuscript with help from M.E. Mycroft and input from all the authors.

Contents

Chapter 1

Introduction

Classical electromagnetism describes light as an oscillating electromagnetic wave. However, this description fails to explain some of the experimental and theoretical observations that emerged around the turn of the 20th century, notably the photoelectric effect and the ultraviolet catastrophe. Planck found that the catastrophe could be resolved by assuming that light is absorbed and emitted in packets of energy, i.e. quanta [1]. Einstein then showed that this idea of light quanta could also explain the photoelectric effect [2]. This was the birth of quantum physics.

The principle of discretizing the energies of fields into quanta is used in all quantum field theories such as quantum optics. These theories have been tremendously successful at explaining and predicting our observations of the world at microscopic scales. There has not yet been an experimental result that challenges the tenets of these theories. Rather, progress in quantum optics is mainly driven by the development of quantum technologies such as secure communication, quantum computers, simulators, and precise sensors. Realizing these technologies requires an increasingly sophisticated control of light and its interaction with matter at the quantum level.

One particularly significant advance in recent years is the development of photon-number-resolving detectors. Traditional photodetectors use large but noisy amplification effects to detect the tiny amount of energy carried by a single photon with an optical frequency. Like a Geiger counter, they "click" when they detect at least one photon but cannot tell you how many. In contrast, photon-number-resolving detectors have the unique ability to count the exact number of photons in an optical field.

This technology opens the door to new ways of manipulating and characterizing light at the quantum level, which is the subject of this thesis.

1.1 What is a quantum state of light?

After quantizing the electromagnetic field (see e.g. Ref. [3]), one finds that a general pure quantum state of a single light mode is described by a superposition of photon-number states $|n\rangle$:

$$|\psi\rangle = \sum_{n=0}^{\infty} c_n |n\rangle \tag{1.1}$$

with $\sum_n |c_n|^2 = 1$. Here c_n is the probability amplitude for the field to contain n photons. Each $|n\rangle$ is a Fock state having the same properties as the energy eigenstates of the quantum harmonic oscillator. The vector $|\psi\rangle$ describes the state of a particular mode of the electromagnetic field determined by its physical properties such as frequency, wave vector, and polarization.

The state can be represented in phase space in terms of the conjugate quadrature operators:

$$\begin{aligned} \hat{x} &= (\hat{a} + \hat{a}^\dagger)/\sqrt{2} \\ \hat{p} &= i(\hat{a} - \hat{a}^\dagger)/\sqrt{2} \end{aligned} \tag{1.2}$$

where $\hat{a}$ ($\hat{a}^\dagger$) are the annihilation (creation) operators with $[\hat{a}, \hat{a}^\dagger] = 1$. The quadrature operators are the analogue to the position and momentum of a harmonic oscillator. Because they do not commute ($[\hat{x}, \hat{p}] = i$), they satisfy an uncertainty principle,

$$\Delta x \Delta p \geq 1/2, \tag{1.3}$$

where Δx (Δp) is the standard deviation of $\hat{x}$ ($\hat{p}$) and $\hbar \equiv 1$. They also determine the in- and out-of-phase components of light's electric field:

$$\hat{E}(\boldsymbol{r}, t) = \mathcal{E}_0 \left(\hat{x} \cos\left[(\boldsymbol{k} \cdot \boldsymbol{r}) - \omega t\right] + \hat{p} \sin\left[(\boldsymbol{k} \cdot \boldsymbol{r}) - \omega t\right]\right) \tag{1.4}$$

where $\mathcal{E}_0 = (\omega/\epsilon_0 V)^{1/2}$ and V is the mode volume. In this example, the mode is a monochromatic plane wave with wave vector $\boldsymbol{k}$ and frequency ω. More general multi-mode fields such as pulses of light can be described by superpositions of such plane waves.

The average electric field of photon-number states vanishes, i.e. $\langle n|\hat{E}(\boldsymbol{r},t)|n\rangle = 0$. However, the variance of the electric field does not vanish since

$$\langle n|\hat{E}^2(\boldsymbol{r},t)|n\rangle = \mathcal{E}_0^2\left(n+\frac{1}{2}\right). \tag{1.5}$$

Therefore, when measuring the electric field of a particular light mode (using e.g. homodyne detection - see Sec. 3.2.1), one observes a spread in the measurement outcomes due to the non-zero variance of the field operator. This phenomenon is often referred to as electric field "fluctuations". In particular, the electric field of the vacuum state ($n = 0$) has fluctuations which is key for explaining phenomena such as the Lamb shift, Casimir effect, and spontaneous parametric down-conversion which we further describe in Sec. 2.2.

Coherent oscillations of the electric field arise from coherences between photon-number states. In particular, the quintessential classical state of light is the coherent state:

$$|\alpha\rangle = e^{-|\alpha|^2}\sum_{n=0}^{\infty}\frac{\alpha^n}{\sqrt{n!}}|n\rangle\,, \tag{1.6}$$

with complex amplitude $\alpha = |\alpha|e^{i\theta}$. This state has the unique property of being an eigenstate of the anhiliation operator: $\hat{a}\,|\alpha\rangle = \alpha\,|\alpha\rangle$. Using this property, its electric field can be evaluated using Eq. (1.4) and is given by

$$\langle\alpha|\hat{E}(\boldsymbol{r},t)|\alpha\rangle = 2|\alpha|\mathcal{E}_0\cos\left(\boldsymbol{k}\cdot\boldsymbol{r}-\omega t+\theta\right). \tag{1.7}$$

The coherent state recovers the classical property of light being an oscillating electromagnetic wave with an amplitude proportional to $|\alpha|$ and phase θ. However, certain features that are absent in the classical theory emerge from the discrete nature of $|\alpha\rangle$, notably fluctuations in its electric field,

$$\langle\alpha|\hat{E}^2(\boldsymbol{r},t)|\alpha\rangle - \langle\alpha|\hat{E}(\boldsymbol{r},t)|\alpha\rangle^2 = \mathcal{E}_0^2, \tag{1.8}$$

which is a consequence of the non-commutivity of $\hat{x}$ and $\hat{p}$. This electric field noise is independent of the phase θ and limits the precision of measurements such as optical interferometry using classical light. One of the motivations of preparing nonclassical

states of light is to surpass such limits, e.g. by using squeezed states which have reduced noise in one quadrature at the expense of increased noise in the conjugate quadrature.

1.1.1 Nonclassical states of light

Light with properties that cannot be explained using classical notions such as oscillating waves will be referred to as "nonclassical light". In contrast, "classical light" will refer to light with mostly classical properties, keeping in mind that all light is quantum and thus has nonclassical features at some level.

One of the pioneering contributions to quantum optics was by R. Glauber who introduced correlation functions to study statistical and coherence properties of light [4]. These functions quantify correlations in an electromagnetic field at different points in space and time. In particular, they can be used to identify nonclassical statistical properties. For example, the second-order correlation function quantifies correlations in the intensity of a field. Nonclassical intensity correlations lead to effects such as photon anti-bunching and sub-Poissonian statistics. We discuss how second-order correlation functions can be measured in Sec. 2.3.2.

The notion of a nonclassical state of light is made rigorous in phase space. Glauber [5] and Sudarshan [6] independently found that any quantum state of light $\hat{\rho}$ can be expressed as a statistical mixture of superpositions of coherent states:

$$\hat{\rho} = \iint d^2\alpha P(\alpha) \left|\alpha\right\rangle \left\langle\alpha\right| \tag{1.9}$$

where $P(\alpha)$ is the so-called P-representation and $\hat{\rho}$ is a general mixed state describing statistical mixtures of pure states like Eq. (1.1). The P-representation of classical states is positive everywhere and no more singular than a Dirac delta function. In this case, $\hat{\rho}$ is statistical mixture of coherent states, i.e. a mixture of coherent waves each having a random phase and amplitude according to the distribution $P(\alpha)$. This can be used to describe partially coherent or even incoherent light, just as in classical electromagnetism [7]. Any state whose P-representation $P(\alpha)$ has negativity or sharp singularities (e.g. a derivative of a Dirac delta function) is nonclassical.

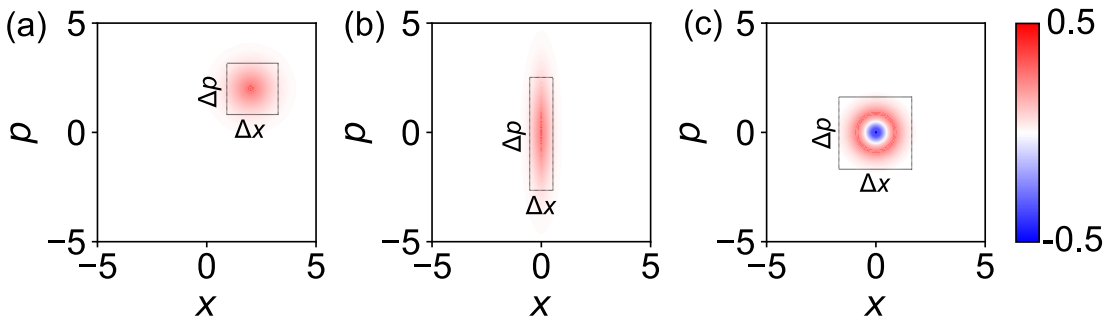

Figure 1.1: **Wigner functions**. (a) Coherent state. $\Delta x = \Delta p$. Classical and Gaussian. (b) Squeezed vacuum state. $\Delta x < \Delta p$. Nonclassical and Gaussian. Dashed lines show one standard deviation. The area of the dashed box is equal to $\Delta x \Delta p = 1/2$ (i.e. minimum uncertainty) in both cases. (c) $n = 1$ photon-number state. $\Delta x = \Delta p$ and $\Delta x \Delta p = 3/2$. Nonclassical and non-Gaussian.

The singular nature of the P-representation can be counter-intuitive. A friendlier phase-space representation is the Wigner function:

$$W(x,p) = \frac{1}{\pi} \int dy \, \langle x+y|\hat{\rho}|x-y\rangle \, e^{2ipy}. \tag{1.10}$$

One can show that the Wigner function is equal to the convolution of the P-representation with a Gaussian which smooths its singularities [8]. As such, the Wigner function is a useful tool to visualize quantum states in phase space. There are a number of sufficient but not necessary conditions for nonclassicality in the Wigner representation such as negativity [9] (e.g. photon-number states), or having a marginal distribution whose variance is smaller than that of vacuum (e.g. squeezed states). Examples are shown in Fig. 1.1.

1.1.2 Gaussianity

Gaussianity is a characteristic of light which has become especially important due to the development of optical quantum information processing [10, 11]. A quantum state whose Wigner function can be represented as a Gaussian distribution is a Gaussian state, and otherwise it is a non-Gaussian state. Pure non-Gaussian states are nonclassical (e.g. photon-number states). However, non-Gaussianity does not always imply nonclassicality nor the converse. For example, squeezed states are Gaussian

and nonclassical while phase-averaged coherent states are non-Gaussian and classical. Generally speaking, nonclassical non-Gaussian states are valuable resources for quantum information processing. For example, such states are essential in both gate-based [12] and measurement-based [13] approaches to optical quantum computing. However, "natural" sources of light (e.g. thermal sources and even lasers) produce statistical mixtures of coherent or thermal states and hence are classical. This begs the question of how to engineer nonclassical states of light.

1.2 Engineering the quantum state of light

Light is produced by the acceleration or deceleration of electric charges which are themselves quantum systems. As such, quantum states of light can be engineered by controlling matter and its interaction with the electromagnetic field at a microscopic level. For example, the spontaneous emission of a single excited atom produces a single photon [14]. Likewise, an excited solid-state emitter like a quantum dot [15] or a colour center in a crystal [16] can also produce single photons. By manipulating the state of single atoms trapped inside of cavities, the cavity field can be prepared in other nonclassical states such as Schrödinger cat states owing to the strong interaction between the cavity field and atoms [17–19]. Such states are further discussed in Chapter 4.

Quantum states of light are also prepared by tailoring the interaction between an electromagnetic field and an ensemble of atoms. Notably, through the process of stimulated emission inside of a cavity containing macroscopic numbers of excited atoms, a laser produces a coherent state of light, $|\alpha\rangle$. Moreover, nonclassical states can be prepared using optical nonlinearities inside nonlinear media [20]. Second-order optical nonlinearities (e.g. spontaneous parametric down-conversion) can produce nonclassical Gaussian states such as squeezed vacuum, which is further discussed in Sec. 2.2. However, because second-order nonlinearities have a quadratic dependence on field amplitudes, they cannot transform Gaussian states into non-Gaussian ones. Therefore, third-order (or higher) optical nonlinearities such as the Kerr effect are required

for directly preparing nonclassical non-Gaussian states from classical inputs [11].

1.2.1 Measurement-based state engineering

A fundamentally different approach that is explored in this thesis is to prepare light in a quantum state that is conditioned on the outcome of a measurement. Although this approach is probabilistic, one can post-select onto particular measurement outcomes to tailor the state of light in a controllable way.

Beam splitters are often employed in measurement-based state engineering schemes since they can introduce correlations between two initially uncorrelated modes. In this way, the measurement outcome obtained by measuring one mode can be correlated with the state of the unmeasured mode. For example, suppose a state of light $|\psi\rangle$ is combined with vacuum on a beam splitter. If a photon-number-resolving detector placed in one output port detects n photons, then the other output port is in the n-photon-subtracted state $\hat{a}^n |\psi\rangle$ (omitting normalization). Even though photon subtraction is a nonclassical operation, $\hat{a}^n |\psi\rangle$ is not necessarily a nonclassical state. For instance, a photon-subtracted coherent state remains a coherent state, i.e. $\hat{a}^n |\alpha\rangle = \alpha^n |\alpha\rangle$. This can be understood intuitively by recalling that a beam splitter transforms $|\alpha\rangle |0\rangle$ into two separable coherent states and hence the output modes are uncorrelated. In general, combining statistical mixtures of coherent states such as thermal states on a beam splitter produces classically-correlated fields at the beam splitter output [21] in which case conditional measurements can only engineer classical states, e.g. photon-subtracted thermal states [22]. In contrast, nonclassical states incident on a beam splitter are generally quantum-correlated (i.e. entangled) at the output, in which case conditional measurements can engineer nonclassical states. For example, photon-subtracted squeezed vacuum states approximate small Schrödinger cat states [23]. Another archetypal example (that is further discussed in Chapter 2) is preparing photon-number states by performing a "heralding" photon-number measurement on one of the modes of an entangled two-mode squeezed vacuum state [24]. These examples also demonstrate the ability to transform Gaussian states into non-Gaussian ones using photon-number measurements.

Measurement-based state engineering schemes have been studied and used since the early days of quantum optics in part due to the weakness of optical nonlinearities at the single photon level. These schemes often employ one of two conventional detection strategies: "click" detectors or homodyne detection, both of which are further discussed in Chapters 2 and 3. However, the development of photon-number-resolving detectors enables new state engineering schemes that exploit the number resolution of such detectors [25, 26]. For example, some recent works have considered multi-photon subtraction [27], addition [28], and catalysis [29–31]. In this thesis, we investigate ways of using photon-number-resolving detectors to engineer nonclassical states of light such as Schrödinger cat states (see Chapter 4) and higher-order photon-number states (see Sec. 2.4 and Chapter 5).

1.3 Thesis outline

The thesis is structured in the following way. Chapter 2 provides an overview of the experimental methods and presents background material that is used throughout the thesis. Chapter 3 presents a hybrid detection strategy known as weak-field homodyne that can tune between photon counting and quadrature measurements by employing photon-number-resolving detectors. Chapter 4 theoretically explores the state engineering capabilities of weak-field homodyne and presents a scheme to prepare states of definite parity. Chapter 5 employs nonclassical states of light prepared with photon-number-resolving detectors for quantum-enhanced optical interferometry. Chapter 6 summarizes the results and provides a brief outlook.

Chapter 2

Experimental methods

This chapter provides background material to better understand the projects presented in Chapters 3, 4, and 5. The chapter begins by discussing photon-number-resolving detectors and the physical operation of transition edge sensors. It then presents an overview of spontaneous parametric down-conversion in waveguides and the production of two-mode squeezed vacuum states. Finally, it discusses the imperfect preparation of photon-number states using photon-number-resolving detectors and two-mode squeezed vacuum states.

2.1 Photon-number-resolving detectors

Photodetectors are devices that create a measurable electrical response to incident light. To detect quantum states of light such as single photons, photodetectors operate with a very large electrical gain by using processes such as avalanche breakdown [32]. Since these amplification processes tend to be noisy, information about the amount of energy absorbed by the photodetector is lost. Instead, the device "clicks" when it detects at least one photon and cannot discern the number of photons it absorbed in a particular detection event.

A more versatile photodetector is able to count the number of photons in a field. Instead of simply "clicking", these detectors output a signal whose properties depend on the number of photons detected. Such a device can determine the photon-number distribution of the incident light, thereby directly measuring its statistical properties.

Detector type	**Operation temperature**	**Efficiency (wavelength)**	**Operation rate**	**Max photons counted**
Photomultipler tube [33, 34]	Room	25% (400nm) [34]	10 MHz	4 [34]
Hybrid photodetector [34]	Room	40% (550nm)	100 MHz	4
Time-multiplexed avalanche photodiode [35, 36]	Room	66% (780nm) [35]	10 kHz	8 [35]
Space-multiplexed avalanche photodiode [37]	Room	33% (1064nm)	25 kHz	1024
Multi-pixel photon counter [38]	Room	25-70% (400nm)	10 MHz	100-1600
Visible light photon counter [39–41]	6-8 K	85% (540nm) [40]	10 kHz	10
Charge integration photon detector [42, 43]	4 K	80% (1550nm)	40 Hz	14
Quantum dot field-effect transistor [44, 45]	4 K	68% (805nm) [44]	1 Hz	3 [45]
Parallel nanowires [46]	2 K	2% (1300nm)	1 GHz	4
Nanowire [47, 48]	2 K	85% (1550nm)	100 MHz	4 [47]
Microwave kinetic inductance detector [49, 50]	100 mK	10% (1550nm)	10 kHz	7 [50]
Transition edge sensor [51–55]	100 mK	98% (850/1550nm) [52, 55]	100 kHz	29 [54]

Table 2.1: A list of photon-number-resolving detector technologies. Note that the parameters listed correspond to the best achieved in the references provided. They do not necessarily represent the limit of the technology.

Table 2.1 lists some of the currently available technologies for photon-number-resolving detectors. This table includes schemes that multiplex click detectors. These schemes probabilistically split the incident light into modes each containing ideally no more than a single photon such that they can be measured by a click detector. The required number of such modes (e.g. spatial or temporal) scales roughly quadratically with the largest countable number of photons [56].

At the bottom of the list, the transition edge sensor stands out from the other technologies due to its exceptionally high efficiency η. This is a crucial consideration when measuring fields containing large numbers of photons since the detection probability scales as η^N for N photons.

2.1.1 Transition edge sensor

Initially developed for astronomical observations [57, 58], transition edge sensors (TESs) are superconducting photodetectors that have an exceptionally high energy resolution and efficiency. The TESs are designed and fabricated by our collaborators at the National Institute of Standards and Technology [51]. A TES consists of a tungsten film embedded inside an optical cavity designed to maximize absorption around 1550 nm. During operation, the TES is cooled to less than 100 mK in a dilution refrigerator so that the tungsten is below its superconducting transition temperature. The TES is then voltage-biased such that it operates in the transition region between its superconducting and normal state. As shown in Fig. 2.1(b), this voltage bias is achieved using a current source that is mostly shunted through $R_{\text{shunt}} \ll R_{\text{TES}}$. A single-mode optical fiber is used to guide light into the TES cavity. When light is absorbed by the TES, the deposited energy increases the tungsten resistance via heating. This reduces the current flowing through an inductor connected in series to the TES. The change in magnetic flux is sensed by an array of superconducting quantum interference devices (SQUIDs) which are very sensitive low-noise magnetometers. The SQUIDs output a μV-level voltage signal (i.e. the detection trace) that is readout and further amplified to mV levels using conventional low-noise amplifiers at room

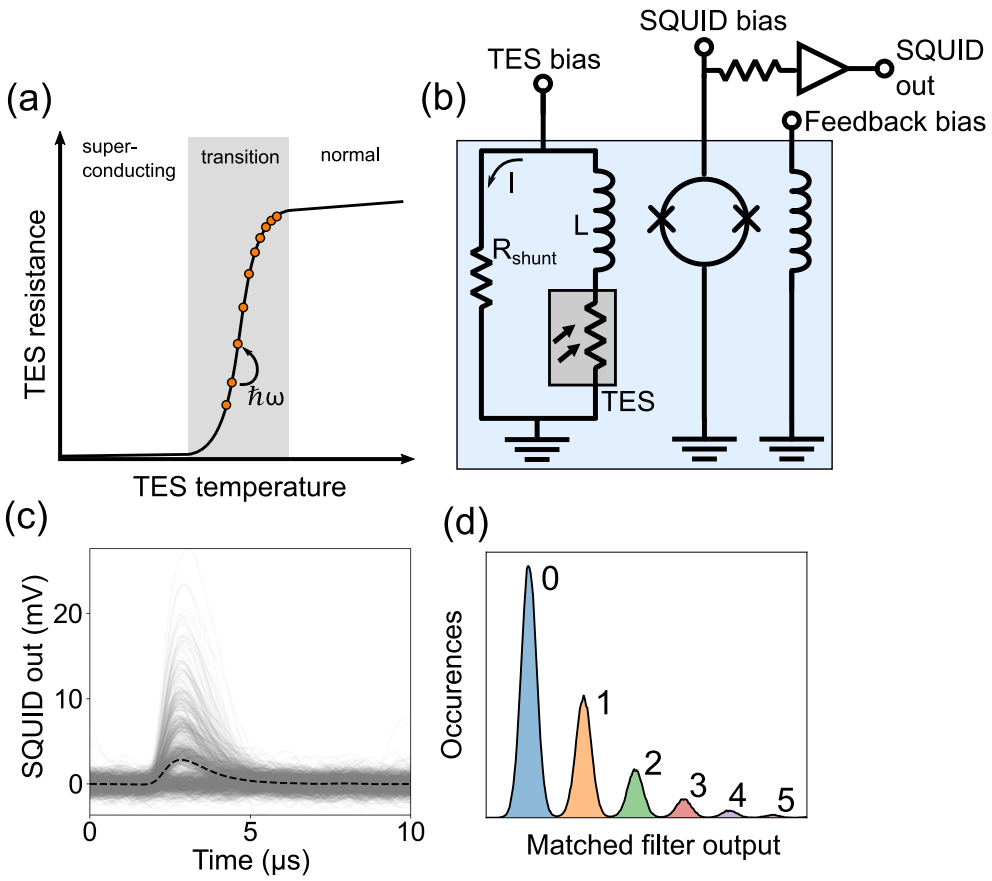

Figure 2.1: **Transition edge sensors**. (a) The detector operates in its transition region between a superconducting and normal state where it is most sensitive to temperature changes. The energy deposited by a single photon causes a significant increase in resistance. (b) The circuit for biasing and reading-out the TES. Components inside the blue box are held at < 100 mK. When light is absorbed, the magnetic flux generated by the inductor L is measured by an array of SQUIDs which act as low-noise amplifiers. Since SQUIDs have a sinusodial voltage-response to flux, they are set to their most sensitive point using a bias flux generated by the feedback inductor coil. Further amplification is performed at room temperature using conventional techniques. (c) Typical detection traces readout from the amplified SQUID output. The black dashed curve is the average trace and is used as a matched filter. (d) The histogram of the matched filter output shows clear bins corresponding to different photon numbers. This is an experimentally measured histogram for incident light in a thermal state.

temperature. Finally, the detection traces are recorded and processed on a computer using an analogue-to-digital card.

Usually TESs are used for detecting pulses of light. In a typical experiment, an electrical signal from the light source triggers a new acquisition of the detector trace each time a pulse is generated. In Fig. 2.1(c), we show the detection traces of roughly 1000 pulses of light in a thermal state[1]. The TESs return to their original state after roughly 5 μs which sets the maximum repetition rate for our experiments. The raw traces already show the quantized nature of absorbed energy, e.g. the trace heights are bunched in groups. Although using the trace height or area (i.e. integrating the traces) can be used to convert the detector output into a photon number, these approaches are more susceptible to electronic noise than the approach presented below [59].

To best extract information about the number of photons absorbed, we use a signal processing technique known as matched filtering [60]. The technique multiplies the noisy detection traces with a filter whose shape resembles that of the desired signal. In practice, our matched filter is created before data acquisition by averaging over at least 10^5 detection traces [black dashed line Fig. 2.1(c)]. This approach produces nearly the optimal filter as it gives the largest weight the desired spectral components of the signal [61]. In Fig. 2.1(d), we show a histogram of the scalar values obtained by taking the inner product of each trace with the matched filter.

2.1.2 Imperfect photon counting

Suppose the matched filtering process described above produces the scalar value s: how do we assign a photon number to s? The probability to obtain the outcome s is determined by $\mathrm{pr}(s) = \mathrm{Tr}(\hat{\rho}\hat{\Pi}^s)$, where $\hat{\Pi}^s$ is an element of the positive operator value measure of the detector and $\hat{\rho}$ is the measured signal. Ideally $\hat{\Pi}^s$ is a projector onto a single photon-number state in which case we can simply assign that photon number to the outcome s. However, in practice $\hat{\Pi}^s$ is a statistical distribution of

[1]The thermal light was generated by pumping a spontaneous parametric down-conversion source using a mode-locked laser with a repetition rate of 100 kHz. See Sec. 2.2 for further details.

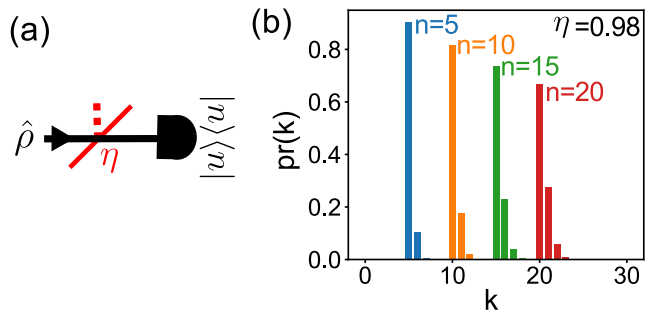

Figure 2.2: **Imperfect photon counting**. (a) A photon-number-resolving detector of efficiency η detecting n photons can be described by the measurement operator $\hat{\Pi}^n(\eta)$ [Eq. (2.2)]. (b) Plot of $\mathrm{pr}(k) = \langle k|\hat{\Pi}^n(\eta)|k\rangle$ for $\eta = 0.98$ which is roughly the efficiency of a TES.

photon-number states due to detector inefficiency and imperfect energy resolution. The positive operator value measure of a TES was experimentally reconstructed using detector tomography in Ref. [55]. Their results show that s can be converted into a photon number using rectangular bins whose widths are determined by the intersection of adjacent Gaussians [see coloured Gaussians in Fig. 2.1(d)]. The measurement operator for outcomes in the nth bin, $\hat{\Pi}^n$, corresponds to a good approximation to the measurement operator of an ideal detector counting n photons but with imperfect efficiency, which we now describe in detail.

Imperfect detection efficiency is modelled by placing a fictitious beam splitter of tranmissivity η before the detector and tracing over the reflected mode. If a signal $\hat{\rho}$ is sent to the detector, as shown in Fig. 2.2(a), the probability to detect n photons is given by [62, 63]:

$$\mathrm{pr}(n) = \sum_{k=n}^{\infty} \binom{k}{n} \eta^n (1-\eta)^{k-n} \mathrm{Tr}(\hat{\rho}\,|k\rangle\,\langle k|). \tag{2.1}$$

That is, when the detector outputs the outcome n, there may have in fact been $k \geq n$ photons in $\hat{\rho}$ and $k - n$ photons were lost, i.e. reflected at the beam splitter. The binomial distribution appears to include all possible ways in which n of the total k photons could have transmitted the beam splitter.

It will be useful to define an operator describing the action of a detector of effi-

ciency η counting n photons:

$$\hat{\Pi}^n(\eta) = \sum_{k=n}^{\infty} \binom{k}{n} \eta^n (1-\eta)^{k-n} \left|k\right\rangle \left\langle k\right| \tag{2.2}$$

such that $\mathrm{pr}(n) = \mathrm{Tr}(\hat{\rho}\hat{\Pi}^n(\eta))$. The Fock representation of this operator, $\mathrm{pr}(k) = \langle k|\hat{\Pi}^n(\eta)|k\rangle$, gives the probability for there being k photons in $\hat{\rho}$ when the detection outcome is n, assuming $\hat{\rho}$ has equal probability to be in any photon-number state. In Fig. 2.2(b), we plot $\mathrm{pr}(k)$ for a few examples cases of n using the estimated efficiency of the TESs, $\eta = 0.98$. The terms with $k > n$ determine the probability that the detector under-counted the true number of photons. These terms become more significant for larger n, which highlights the need for high-efficiency photon-number-resolving detectors when large photon numbers are being counted.

2.2 Spontaneous parametric down-conversion

Spontaneous parametric down-conversion (SPDC) is a three-wave mixing nonlinear optical process. Unlike other three-wave mixing processes, two of the three fields involved are initially in a vacuum state. A strong pump field parametrically amplifies vacuum fluctuations in these two fields, resulting in energy transfer from the pump into the two lower frequency fields.

SPDC should be treated quantum mechanically to fully describe the features of the down-converted light. A derivation from first principles is done in detail in a number of works (e.g. Ref. [64]) - I only give an overview here. The problem can be treated as a scattering process in which a pump photon of frequency ω_p scatters into two lower energy photons, conventionally called the signal (ω_s) and idler (ω_i) photons ($\omega_p > \omega_s \geq \omega_i$). This process must satisfy both energy and momentum conservation:

$$\begin{aligned} \omega_p &= \omega_s + \omega_i \\ \vec{k}(\omega_p) &= \vec{k}(\omega_s) + \vec{k}(\omega_i), \end{aligned} \tag{2.3}$$

where $\vec{k}$ is the wavevector.

Since the pump is typically from a pulsed laser and contains billions of photons, the pump field can be described by a classical complex spectral amplitude function

$\alpha(\omega_p)$ whose energy is approximately unchanged by the scattering process. We assume that all three fields propagate collinearly inside a nonlinear medium of length L. The Hamiltonian describing the interaction between the three fields is given by:

$$\hat{H} = \zeta \iint d\omega_s d\omega_i \alpha(\omega_s + \omega_i)\phi(\omega_s, \omega_i)\hat{a}^\dagger(\omega_s)\hat{a}^\dagger(\omega_i) + h.c., \tag{2.4}$$

where ζ is the strength of the interaction that depends on the material nonlinearity $\chi^{(2)}$, the pump field strength[2], and L. The term $\phi(\omega_s, \omega_i)$ is known as the phase-matching function and depends on the phase mismatch between the three fields as they travel at difference phase velocities in the material:

$$\phi(\omega_s, \omega_i) = \text{sinc}\left(\frac{\Delta k L}{2}\right) \tag{2.5}$$

with

$$\begin{aligned} \Delta k &= k(\omega_s + \omega_i) - k(\omega_s) - k(\omega_i) \\ &= n(\omega_s + \omega_i)[\omega_s + \omega_i]/c - n(\omega_s)\omega_s/c - n(\omega_i)\omega_i/c \end{aligned} \tag{2.6}$$

being the wavevector mismatch which depends on the material refractive index $n(\omega)$. The spectral properties of the down-converted light are determined by the so-called joint spectral amplitude $f(\omega_s, \omega_i) = \alpha(\omega_s + \omega_i) \times \phi(\omega_s, \omega_i)$ which is the product of the pump spectral amplitude $\alpha(\omega_s + \omega_i)$ and the phase-matching function $\phi(\omega_s, \omega_i)$. Frequency components with $\Delta k = 0$ maximize the phase-matching function amplitude and hence are dramatically brighter than those with $\Delta k \neq 0$.

2.2.1 Phase-matching engineering

Phase matching ($\Delta k = 0$) can be tricky to achieve because most lossless materials have normal dispersion, i.e. $n(\omega_1) > n(\omega_2)$ for $\omega_1 > \omega_2$. Usually, one employs material birefringence to overcome this issue by ensuring that the pump polarization is aligned with the crystal axis having the smaller refractive index. In general, the Sellmeier equations can be used to identify a combination of polarization and frequencies that

[2]We assumed $\alpha(\omega_p)$ is a dimensionless normalized function and absorbed the pump amplitude into ζ.

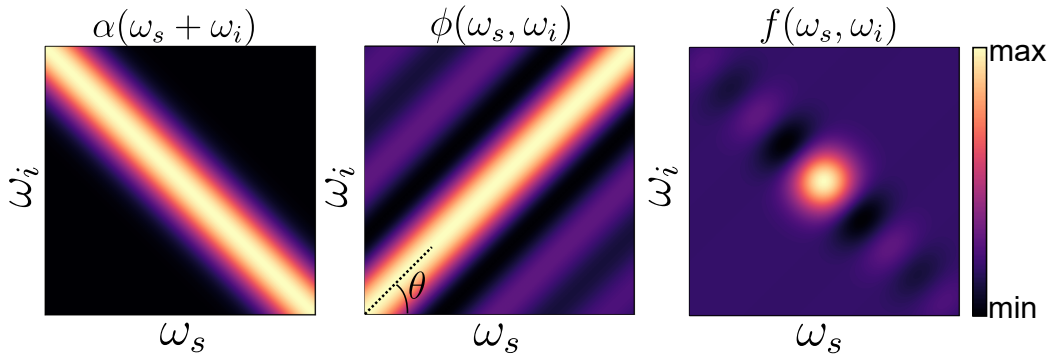

Figure 2.3: **Joint spectral amplitude**. The product of the pump spectral amplitude $\alpha(\omega_s+\omega_i)$ and the phase-matching function $\phi(\omega_s, \omega_i)$ determines the joint spectral amplitude $f(\omega_s, \omega_i)$. Materials with $\theta \in [0, \pi/2]$ can produce a spectrally decorrelated joint spectral amplitude, as is approximately the case in the figure.

achieve $\Delta k = 0$ in a given material. For additional flexibility, one can employ a quasi-phase-matching technique by periodically reversing the crystal axis of a material (e.g. by exposing it to a strong static electric field). To first order, this adds a term to the wavevector mismatch $\Delta k = k(\omega_s + \omega_i) - k(\omega_s) - k(\omega_i) - \Lambda/2\pi$, where the poling period Λ provides a new degree of controllability.

An important consideration for SPDC are signal-idler frequency correlations in the joint spectral amplitude $f(\omega_s, \omega_i)$. These correlations cause the down-converted modes to be spectrally entangled which is often undesirable. For example, a common application of SPDC is to prepare a heralded single photon in the signal mode by detecting the presence of a photon in the idler mode. Since this measurement is frequency insensitive, the signal mode is projected into a mixed state whose purity depends on the strength of the spectral correlations.

Spectrally decorrelated down-converted light can be produced if the joint spectral amplitude can be made factorable, i.e. $f(\omega_s, \omega_i) = f_s(\omega_s) f_i(\omega_i)$. The requirements to realize this property have been well-studied [65, 66] and achieved experimentally [67]. One important quantity to consider is the phase-matching function angle θ, as shown in Fig. 2.3. To first order in dispersion, this angle is determined by [68]:

$$\tan\theta = -\frac{v_p^{-1} - v_s^{-1}}{v_p^{-1} - v_i^{-1}} \tag{2.7}$$

where $v_x = \partial\omega/\partial k(\omega)|_{\omega_x}$ is light's group velocity at a frequency ω_x. Materials for

which $v_s \leq v_p \leq v_i$ have phase-matching functions with $\theta \in [0, \pi/2]$. Such materials can generally be used to produce an uncorrelated joint spectral amplitude by appropriately choosing the pump bandwidth for a given θ and L.

2.2.2 KTP waveguides

Optical waveguides are structures with an inhomogeneous refractive index that confine and guide light. They are also often used to enhance the strength of nonlinear optical processes. In the case of SPDC, this enhancement occurs for two main reasons. Firstly, waveguides give rise to a discrete set of guided modes determined by the waveguide boundary conditions. Rather than having a continuum of modes into which the SPDC process can scatter, as would be the case with a bulk material, the signal and idler fields in a waveguide occupy a limited number of modes. In particular, single-mode waveguides are designed to have a single guided spatial mode[3] which greatly increases the mode coupling between the pump and down-converted fields [69]. Secondly, SPDC is enhanced by confining the pump over the entire waveguide length which can be much longer than the Rayleigh length of a strongly focused field inside a bulk material. For these two reasons, SPDC in waveguides can be significantly brighter than in bulk materials. While a single photon pair might be produced once in every 25 pump pulses with bulk sources [70], the waveguide source presented below can produce more than one photon pair every pump pulse.

The experiments carried out in the thesis use a SPDC source based on the design in Refs. [71, 72]. The source is a 8 mm long z-cut biaxial potassium titanyl phosphate (KTP) crystal, purchased commercially from AdVR Inc. Waveguides are formed in the crystal by photomasking the material and exposing it to Rb vapour. Through ion-exchange (K $\leftrightarrow$ Rb), the refractive index of the crystal is locally modified and forms waveguides. The waveguides are then periodically poled such that phase matching is achieved when pumped at 775 nm and produces nearly degenerate and orthogonally polarized signal and idler photons around 1550 nm. These wavelengths are convenient

[3]Waveguides also have a continuum of unguided modes where light propagates with exponentially decaying energy. SPDC sometimes produces a photon in such a mode which gives rise to a background of uncorrelated photons that degrade the purity of the SPDC source - see Sec. 2.3.2

as a titanium sapphire laser can be used for the pump and the down-converted photons can be coupled into telecom fibers which have low propagation losses. Moreover, at these wavelengths the phase-matching function has an angle of $\theta \approx \pi/3$. Thus, by choosing the appropriate pump bandwidth, the KTP waveguides can in principle produce SPDC light with a decorrelated joint spectral amplitude.

2.2.3 Two-mode squeezed vacuum

When the joint spectrum amplitude is decorrelated, $f(\omega_s, \omega_i) = f_s(\omega_s) f_i(\omega_i)$, it is convenient to define operators that describe the creation of photons in the spectral modes f_s and f_i:

$$\begin{aligned} \hat{a}^\dagger_{f_s} &= \int d\omega_s f_s(\omega_s) \hat{a}^\dagger(\omega_s) \\ \hat{a}^\dagger_{f_i} &= \int d\omega_i f_i(\omega_i) \hat{a}^\dagger(\omega_i). \end{aligned} \tag{2.8}$$

Re-writing the SPDC interaction Hamiltonian in Eq. (2.4) in terms of these operators, we find the considerably simpler expression:

$$\hat{H} = \zeta \hat{a}^\dagger_{f_s} \hat{a}^\dagger_{f_i} + h.c. \tag{2.9}$$

The state produced by this SPDC interaction can be obtained by applying the unitary transformation $e^{i\hat{H}}$ on the initially empty signal and idler modes $|0_s, 0_i\rangle$[4]. The result is derived in Ref. [3] and is given by:

$$\begin{aligned} |\Psi\rangle &= e^{i(\zeta \hat{a}^\dagger_{f_s} \hat{a}^\dagger_{f_i} + h.c.)} |0_s, 0_i\rangle \\ &= \sum_{n=0}^{\infty} \frac{\left(i\zeta \hat{a}^\dagger_{f_s} \hat{a}^\dagger_{f_i} + i\zeta^* \hat{a}_{f_s} \hat{a}_{f_i}\right)^n}{n!} |0_s, 0_i\rangle \\ &= \sqrt{1-\lambda^2} \sum_{n=0}^{\infty} \lambda^n |n_{f_s}, n_{f_i}\rangle \end{aligned} \tag{2.10}$$

where $\lambda = \tanh(\zeta)$. Eq. (2.10) is a two-mode squeezed vacuum state. The parameter ζ is called the squeezing or parametric gain parameter. The average number of photons in the signal or idler mode is given by $\langle n \rangle = \sinh^2(\zeta) = \lambda^2/(1-\lambda^2)$. Importantly, the two modes are quantum-correlated and always have the same number of photons.

[4]We assumed $\hbar \equiv 1$ and absorbed the propagation time into ζ. Moreover, we are neglecting time-ordering effects which can modify the spectral properties of the down-converted light when the parametric gain is large [73–75].

If $f(\omega_s, \omega_i) \neq f_s(\omega_s) f_i(\omega_i)$, we can use a Schmidt decomposition to express $f(\omega_s, \omega_i)$ as a linear combination of decorrelated functions:

$$f(\omega_s, \omega_i) = \sum_{k=0}^{\infty} c_k \phi_k(\omega_s) \psi_k(\omega_i) \tag{2.11}$$

with $\sum_k |c_k|^2 = 1$ and the functions $\{\psi_k\}$ and $\{\phi_k\}$ form an orthonormal basis that can be determined by a singular value decomposition. The Schmidt number $K = (\sum_k |c_k|^4)^{-1}$ quantifies the strength of the spectral correlations, e.g. $K = 1$ indicates no spectral correlations. Following the same procedure as in Eq. (2.10), one finds that the output state of this SPDC process is:

$$|\Psi\rangle = \bigotimes_{k=0}^{\infty} \sqrt{1 - \lambda_k^2} \sum_{n_k=0}^{\infty} \lambda_k^{n_k} |n_{k_{\phi_k}}, n_{k_{\psi_k}}\rangle \tag{2.12}$$

where $\lambda_k = \tanh(c_k \zeta)$. Eq. (2.12) describes a tensor product state of effectively K two-mode squeezed vacuum states each occupying a different spectral mode. Crucially, since discerning between different spectral modes is not feasible with most detection techniques, this multi-modedness manifests itself as a reduction in modal purity $\mathcal{P}_m$ of the SPDC source, i.e. $\mathcal{P}_m = 1/K$.

2.3 Characterizing SPDC sources

In this section we describe the techniques used to characterize and optimize the performance the KTP waveguide sources. The goal is to use these sources to produce a pure two-mode squeezed vacuum state occupying a single spectral mode ($K = 1$). To do so, the pump spectrum must be adjusted until the joint spectral amplitude of the source is decorrelated, i.e. $f(\omega_s, \omega_i) = f_s(\omega_s) f_i(\omega_i)$. Unfortunately, this quantity is rather difficult to measure directly since special interferometeric techniques are necessary to retrieve its phase [76–78]. Instead, we perform various simpler measurements that each reveal different pieces of information about $f(\omega_s, \omega_i)$.

2.3.1 Spectral characterization

Although $f(\omega_s, \omega_i)$ is difficult to measure, the joint spectral intensity $|f(\omega_s, \omega_i)|$ can be measured rather easily. Because there could be correlations in the spectral phase of

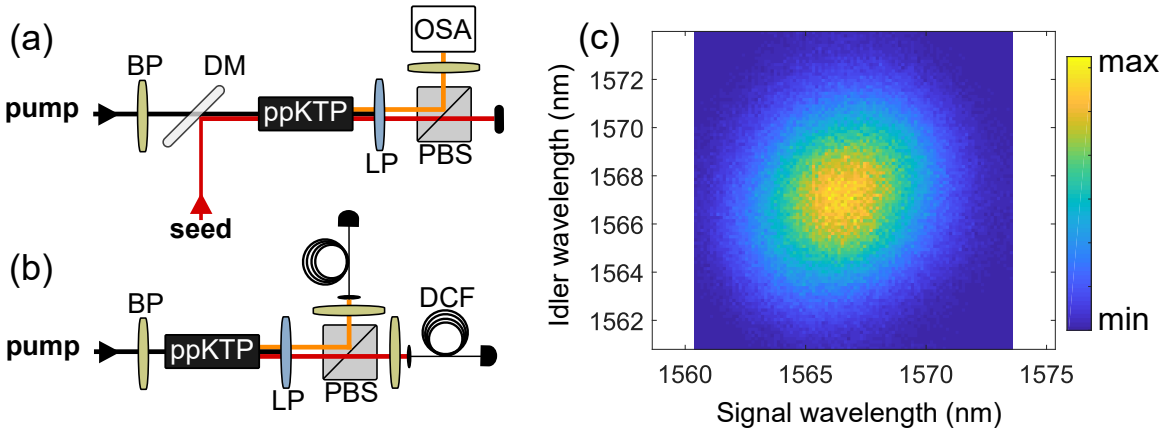

Figure 2.4: **Measuring the joint spectral intensity**. (a) Stimulated emission tomography. (b) Single photon time-of-flight spectrometer. A description of the experimental setup is provided in the main text. Both techniques are used to determine the optimal pump spectrum that ensures that $|f(\omega_s, \omega_i)|$ is spectrally decorrelated. (c) A typical joint spectral intensity measured with the latter method. The sinc sidelobes are filtered out by broad bandpass filters placed in signal and idler modes after the waveguide. BP: bandpass filter, DM: dichroic mirror, ppKTP: periodically poled potassium titanyl phosphate, LP: longpass filter, PBS: polarizing beam splitter, OSA: optical spectrum analyzer, DCF: dispersion compensation fiber.

$f(\omega_s, \omega_i)$ due to, e.g. chirp in the pump, it is a necessary but not sufficient requirement that $|f(\omega_s, \omega_i)|$ be uncorrelated to ensure the single-modedness of the SPDC sources. In practice, this measurement is used to determine the optimal pump bandwidth and central wavelength that minimizes K. Starting with broadband pulses from a mode-locked titanium sapphire laser, we carve out a pump spectrum using a pair of bandpass dieletric filters whose transmission window can be adjusted by angle-tuning the filters.

The first technique to determine $|f(\omega_s, \omega_i)|$ is shown in Fig. 2.4(a) and is known as stimulated emission tomography [79]. Both a strong pump and seed field are coupled into the KTP waveguide such that difference frequency generation occurs, i.e. the stimulated analogue to SPDC. The latter field is from a continuous-wave laser. Looking back at Eq. (2.4), the signal mode is now a bright classical monochromatic field and so we can invoke the approximation $\hat{a}^\dagger(\omega_s) \to \alpha\delta(\omega_s - \omega_{s_0})$ where α is the complex amplitude of the seed field of frequency ω_{s_0}. As a result, the Hamiltonian in

Eq. (2.4) is simplified to:

$$\begin{aligned}\hat{H}_{\mathrm{DFG}} &= \zeta \int d\omega_i f(\omega_{s_0}, \omega_i) \alpha \hat{a}^\dagger(\omega_i) + h.c. \\ &= \zeta\alpha \hat{a}^\dagger_{\bar{f}(\omega_i)} + \zeta\alpha^* \hat{a}_{\bar{f}(\omega_i)}\end{aligned} \tag{2.13}$$

where we defined the creation operator

$$\hat{a}^\dagger_{\bar{f}(\omega_i)} = \int d\omega_i f(\omega_{s_0}, \omega_i) \hat{a}^\dagger(\omega_i) \tag{2.14}$$

which describes the creation of a photon in the spectral mode $\bar{f}(\omega_i)$, a cross-section of the joint spectral amplitude evaluated at the seed frequency ω_{s_0} [79]. Eq. (2.13) describes a displacement operation in the idler mode of strength $\zeta\alpha$. Since the idler mode is initially in its vacuum state, the interaction prepares a coherent state of amplitude $\zeta\alpha$ with a spectrum given by $\bar{f}(\omega_i)$. Crucially, α can be made very large by using a bright seed laser. Moreover, the idler and seed fields are orthogonally polarized due to the phase matching conditions and hence can be spatially separated using a polarizing beam splitter. By scanning ω_{s_0} and measuring the spectrum of the idler field using a spectrometer, the entire function $|f(\omega_s, \omega_i)|$ can be determined. In our case, the spectral resolution of this technique was limited by the spectrometer which had a resolution of 0.02 nm (Yokagawa AQ6370D).

Another approach is to use a spectrometer sensitive to single photons [80, 81]. This is achieved in the lab by sending the signal and idler modes through long dispersive fibers (Corning DCM-B-060-0) such that the light's wavelength is mapped to its arrival time at a single photon detector, as shown in Fig. 2.4(b). For this measurement we employ fast nanowire click detectors. Since these have a timing resolution of 80 ps and the fiber has a dispersion of -997 ps/nm around 1550 nm, the time-of-flight spectrometer has a resolution of approximately 0.08 nm. The joint spectral intensity is determined by coincidence events at both detectors. The spectrometers can be calibrated using energy conservation: by simultaneously sending both signal and idler modes through the same dispersive fiber, the center between the two spectra corresponds to half the pump frequency.

Both methods were used to characterize the spectral properties of the KTP sources. When the signal and idler modes have similar frequencies, the second method is preferable since with the first method, light from the bright seed can leak into the spectrometer despite the polarization filtering. A typical joint spectrum intensity measured using the second method after optimizing the pump bandwidth is shown in Fig. 2.4(c). The difference frequency generation technique is also used to prepare a local oscillator for the experiment in Chapter 3.

2.3.2 Photon statistics characterization

The effective number of spectral modes K of a SPDC source can be determined by measuring the photon statistics of the signal and idler modes. By tracing over one of the modes of the two-mode squeezed vacuum state in Eq. (2.10) produced by a decorrelated ($K = 1$) SPDC source, we find that the signal and idler modes are in a thermal state occupying a single spectral mode:

$$\hat{\rho} = (1 - \lambda^2) \sum_{n=0}^{\infty} \lambda^{2n} |n\rangle \langle n| . \tag{2.15}$$

In this case, the photon-number distribution $\mathrm{pr}(n) = \mathrm{Tr}(\hat{\rho} |n\rangle \langle n|) = (1 - \lambda^2)\lambda^{2n}$ is a thermal distribution. In contrast, a spectrally-correlated SPDC source produces effectively K two-mode squeezed vacuum states in orthogonal spectral modes [Eq. (2.12)], and thus the signal and idler modes are in a product state of K thermal states like Eq. (2.15) each occupying a different spectral mode. Since photodetectors such as TESs simply convolve the signals from the different spectral modes, the measured $\mathrm{pr}(n)$ is a convolution of K thermal distributions. In Appendix A, we show that $\mathrm{pr}(n)$ tends towards a Poissonian distribution for $K \to \infty$.

In general, K can be determined from the relation between the mean $\langle n \rangle$ and variance $\langle (\Delta n)^2 \rangle$ of $\mathrm{pr}(n)$. This relation is characterized by the normalized second-order correlation function which describes intensity correlations in light [3]:

$$g^{(2)} = \frac{\langle \hat{a}^\dagger \hat{a}^\dagger \hat{a} \hat{a} \rangle}{\langle \hat{a}^\dagger \hat{a} \rangle \langle \hat{a}^\dagger \hat{a} \rangle} = \frac{\sum_n \mathrm{pr}(n)(n^2 - n)}{\left(\sum_n \mathrm{pr}(n) n\right)^2} = 1 + \frac{\langle (\Delta n)^2 \rangle - \langle n \rangle}{\langle n \rangle^2}, \tag{2.16}$$

where $\hat{a}$ is a single mode of the signal of interest. Light with $g^{(2)} = 1$ such as a coherent state has Poissonian statistics, meaning the probability of detecting a photon is independent of previous detection events but occurs at a fixed mean rate. In contrast, a thermal state has $g^{(2)} = 2$ and has "bunched" detection events.

The transformation of the signal and idler mode photon statistics from thermal to Poissonian with increasing K can be related to the $g^{(2)}$ [82]. In Appendix A, we derive that:

$$g^{(2)} = 1 + 1/K = 1 + \mathcal{P}_m. \tag{2.17}$$

where $\mathcal{P}_m = 1/K$ is the modal purity.

Unlike $\mathrm{pr}(n)$, $g^{(2)}$ is independent of the detector efficiency [83], as we now show. Assuming the signal mode after loss is given by $\hat{c} = \sqrt{\eta}\hat{a} + i\sqrt{1-\eta}\hat{b}$ where $\hat{a}$ is the signal mode before loss, $\hat{b}$ is a vacuum mode, and η is the detector efficiency, one finds:

$$\begin{aligned} g^{(2)} &= \frac{\langle \hat{c}^\dagger \hat{c}^\dagger \hat{c}\hat{c} \rangle}{\langle \hat{c}^\dagger \hat{c} \rangle \langle \hat{c}^\dagger \hat{c} \rangle} \\ &= \frac{\langle (\sqrt{\eta}\hat{a}^\dagger - i\sqrt{1-\eta}\hat{b}^\dagger)^2 (\sqrt{\eta}\hat{a} + i\sqrt{1-\eta}\hat{b})^2 \rangle}{\langle (\sqrt{\eta}\hat{a}^\dagger - i\sqrt{1-\eta}\hat{b}^\dagger)(\sqrt{\eta}\hat{a} + i\sqrt{1-\eta}\hat{b}) \rangle^2} \\ &= \frac{\langle \eta^2 \hat{a}^\dagger \hat{a}^\dagger \hat{a}\hat{a} \rangle}{\langle \eta \hat{a}^\dagger \hat{a} \rangle^2} \\ &= \frac{\langle \hat{a}^\dagger \hat{a}^\dagger \hat{a}\hat{a} \rangle}{\langle \hat{a}^\dagger \hat{a} \rangle \langle \hat{a}^\dagger \hat{a} \rangle} \end{aligned} \tag{2.18}$$

where in the third line we used the fact that normally-ordered terms such as $\hat{b}^\dagger \hat{b}$ vanish since $\hat{b}$ is in a vacuum state. The independence of $g^{(2)}$ to detector efficiency makes it a simple way of experimentally characterizing K. Moreover, it is worth noting that the $g^{(2)}$ can also be measured using click detectors by employing a Hanbury Brown and Twiss interferometer.

We measure $\mathrm{pr}(n)$ of the signal and idler modes of our KTP source using a TES from which we determine $g^{(2)}$ using Eq. (2.16). An example is shown in Fig. 2.5(b) which has $g^{(2)} = 1.85 \pm 0.01$. With an optimal pump bandwidth and some minimal signal/idler spectral filtering to eliminate the sinc sidelobes in the joint spectral intensity, the KTP sources tend to produce $g^{(2)}$ values between 1.80 and 1.85. This

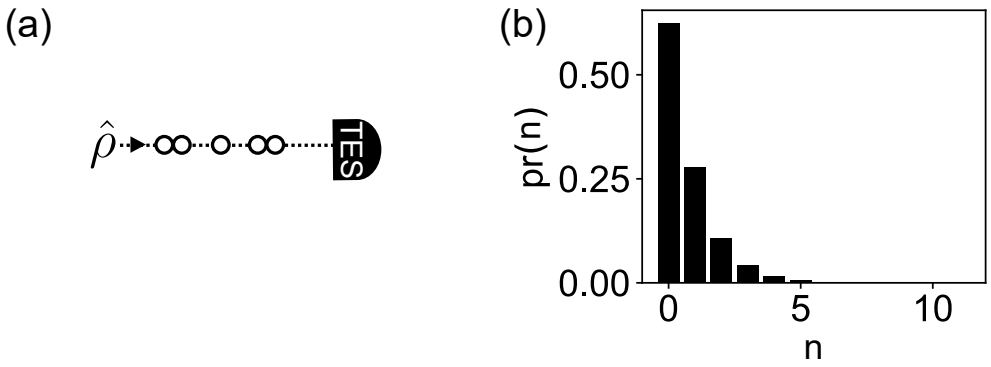

Figure 2.5: **Photon statistics measurement**. (a) The photon-number distribution pr(n) of the incident light can be directly measured using a transition edge sensor. This distribution fully determines its photon statistics including the second order correlation function $g^{(2)}$. (b) The measured pr(n) of one the down-converted modes produced by a KTP waveguide after optimizing its modal purity by adjusting the pump spectrum (see Fig. 2.6(a) for the experimental setup). Using pump pulses with a center wavelength of 783 nm and bandwidth (full-width at half maximum) of 2 nm, the down-converted light has $g^{(2)} = 1.85 \pm 0.01$ and shows thermal-like statistics.

spread in values is partly due to imperfections in the manufacturing process such as non-uniform poling periods or photomasks. The main causes for the overall reduction from the ideal value of 2 are fluorescence from colour centers and unguided SPDC processes in the waveguides [64], which both produce uncorrelated photons.

2.3.3 Efficiency characterization

It is possible to increase the modal purity of the two-mode squeezed vacuum source by strongly spectrally filtering the signal and idler modes. However, this comes at the cost of introducing loss. An equally important quantity for the experiments performed in this thesis is the end-to-end efficiency η of the source. This can be calculated via a Klyshko measurement [84].

In the absence of loss, a two-mode squeezed vacuum state [Eq. (2.10)] has an equal number of photons in the signal and idler mode. Klyshko measurements exploit these photon-number correlations to estimate the total efficiency of either mode. For example, in a simple case where the SPDC source only produces single photon pairs (i.e. low gain), the efficiency can be determined with click detectors by measuring the probability of detecting a photon in the signal mode conditioned on having detected

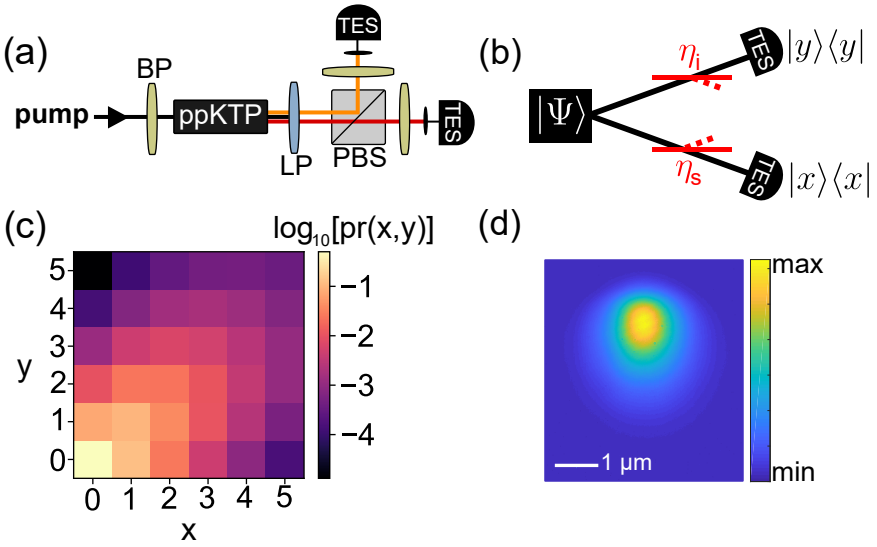

Figure 2.6: **Efficiency measurement**. (a) Setup for a Klyshko measurement. (b) Theory depiction of the setup to measure the joint photon-number distribution $\mathrm{pr}(x, y)$. Beam splitters model all losses in each mode. (c) Example of a measured joint photon-number distribution which can be fitted to Eq. (2.19) using $\lambda = 0.74$, $\eta_s = 0.49$, $\eta_i = 0.50$. (d) Typical intensity distribution of a waveguide spatial mode. Its non-Gaussian features limit the coupling into single-mode optical fiber to $\sim 70\%$ efficiency. Scale bar shows dimension in the object plane, i.e. at facet of waveguide.

one in the idler mode (and vice-versa). This is also termed the heralding efficiency.

With TESs, we are not restricted to low gain [85]. Rather, we can measure the full joint photon-number statistics of the signal and idler mode to estimate the efficiencies. The setup is shown in Fig. 2.6(a). The efficiency is determined by fitting the measured joint photon-number distribution to the following[5]:

$$\mathrm{pr}(x, y) = (1 - \lambda^2) \sum_{n=\max(x,y)}^{\infty} \binom{n}{x} \binom{n}{y} \lambda^{2n} \eta_s^x \eta_i^y (1 - \eta_s)^{n-x} (1 - \eta_i)^{n-y}, \tag{2.19}$$

where η_s and η_i are the transmissivities of the beam splitters shown in Fig. 2.6(b). These beam splitters model the combined losses in the setup, e.g. waveguide losses, optical elements like filters and mirrors, and the imperfect detector efficiencies. The main source of loss is in the coupling of the down-converted light into single-mode optical fibers. The spatial mode of the waveguide has non-Gaussian features [Fig. 2.6(d)] which limits fiber coupling efficiency to around 70%. The highest end-to-end efficiency

[5]This distribution can be obtained using Eq. (2.24) derived in the next section, i.e. $\mathrm{pr}(x, y) = \mathrm{Tr}(\hat{\rho}_s^{(y)} |x_s\rangle \langle x_s|)$.

achieved in the experiments presented in thesis was $\eta \sim 50\%$. An example of a measured joint photon-number distribution is shown in Fig. 2.6(c), which when fitted to Eq. (2.19) yields $\lambda = 0.74$, $\eta_s = 0.49$, $\eta_i = 0.50$.

2.4 Heralding photon-number states

The use of SPDC for preparing single photons is well established. Far fewer experiments [86–89] have used SPDC for heralding larger photon-numbers mainly due to a lack of photon-number-resolving detectors and limited squeezing. In this thesis, we take advantage of the TESs and the high gain of the KTP waveguide sources to herald large photon-number states. These states are used for the experiments described in Chapters 3 and 5.

The setup is shown in Fig. 2.7(a). Suppose the KTP waveguide produces a pure two-mode squeezed vacuum state

$$|\Psi_{si}\rangle = \sqrt{1-\lambda^2}\sum_{n=0}^{\infty}\lambda^n |n_s, n_i\rangle\,, \tag{2.20}$$

where we now include mode labels for additional clarity. If the TES measures j photons in the idler mode i, this measurement should ideally project the signal mode s into the corresponding photon-number state:

$$\hat{\rho}_s^{(j)} = \mathrm{Tr}_i\left(|j_i\rangle\langle j_i|\Psi_{si}\rangle\langle\Psi_{si}|\right) = \mathcal{N}\,|j_s\rangle\langle j_s| \tag{2.21}$$

where $\mathcal{N} = (1-\lambda^2)\lambda^{2j}$ is the probability of this measurement outcome occurring. However, losses in the signal and idler arm [Fig. 2.7(b)] cause $\hat{\rho}_s^{(j)}$ not be this straightforward.

Let us first consider loss in the idler mode, i.e. the heralding arm. A detector with efficiency η_i counting j photons performs the measurement $\hat{\Pi}_i^j(\eta_i)$ [Eq. (2.2)]. The state heralded by this measurement is

$$\begin{aligned}\hat{\rho}_s^{(j)} &= \mathrm{Tr}_i\left(\hat{\Pi}_i^j(\eta_i)\,|\Psi_{si}\rangle\langle\Psi_{si}|\right)\\ &= \left(1-\lambda^2\right)\sum_{k=j}^{\infty}\binom{k}{j}\eta_i^j(1-\eta_i)^{k-j}\lambda^{2k}\,|k_s\rangle\langle k_s|\,.\end{aligned} \tag{2.22}$$

This state has a binomial factor in its photon-number distribution due to the detection inefficiency as well as a factor of $(1-\lambda^2)\lambda^{2k}$ giving the probability to produce k photon pairs.

Next, we consider the effect of losses in the signal mode. As before, loss is modelled using a fictitious beam splitter of transmissivity η_s and tracing over the reflected modes, which transforms photon-number states in the following way:

$$|k_s\rangle\langle k_s| \to \sum_{l=0}^{k} \binom{k}{l} \eta_s^l (1-\eta_s)^{k-l} |l_s\rangle\langle l_s| . \tag{2.23}$$

Applying this transformation to the state in Eq. (2.22), one finds

$$\hat{\rho}_s^{(j)} = (1-\lambda^2) \sum_{k=j}^{\infty} \sum_{l=0}^{k} \binom{k}{j} \binom{k}{l} \lambda^{2k} \eta_i^j \eta_s^l (1-\eta_i)^{k-j} (1-\eta_s)^{k-l} |l_s\rangle\langle l_s| . \tag{2.24}$$

Eq. (2.24) is a statistical mixture of photon-number states whose distribution depends on λ and the losses. The photon-number purity of $\hat{\rho}_s^{(j)}$ is quantified by $\mathcal{P}_p = \mathrm{Tr}([\hat{\rho}_s^{(j)}]^2)$ and should not be confused with the previously mentioned modal purity $\mathcal{P}_m$. Simultaneously treating both modal impurity and losses is significantly more involved [89].

2.4.1 Nonclassicality of imperfectly heralded photon-number states

Ideal photon-number states $|j\rangle$ have sub-Poissonian statistics, as illustrated by their second-order correlation function[6]:

$$g^{(2)} = \begin{cases} 1, & \text{for } j = 0 \\ 1 - 1/j, & \text{for } j \geq 1. \end{cases} \tag{2.25}$$

We measure the photon-number distribution $\mathrm{pr}(n) = \mathrm{Tr}\left(\hat{\rho}_s^{(j)} |n_s\rangle\langle n_s|\right)$ of the heralded state using a second TES and employ the expression in Eq. (2.16) to calculate its $g^{(2)}$. The result is plotted in Fig. 2.7(c). Although the degree of nonclassicality is degraded by the losses, the heralded $\hat{\rho}_s^{(j)}$ has sub-Poissonian statistics for $j \geq 1$ and hence is nonclassical. For example, $\hat{\rho}_s^{(6)}$ has $g^{(2)} = 0.954 \pm 0.016$.

[6]The second order correlation function of the vacuum state is not well defined. Here we take its value to be 1 as a limiting case of a coherent state of vanishing amplitude.

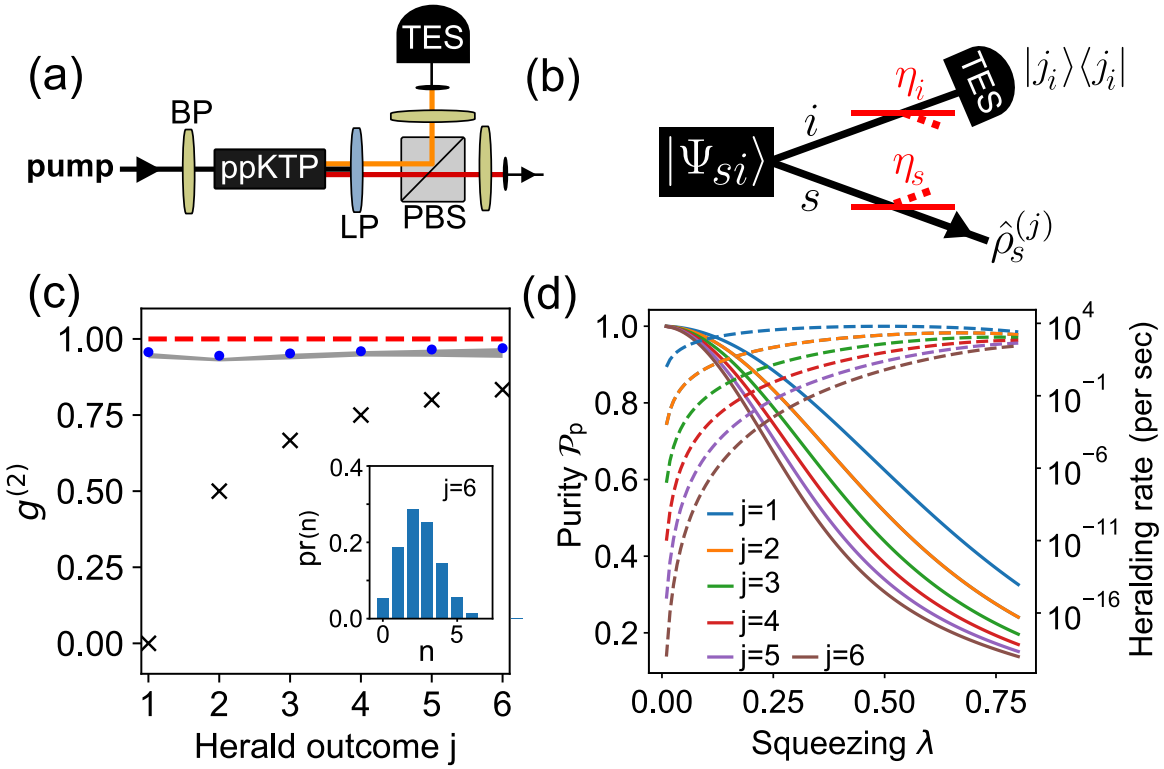

Figure 2.7: **Photon-number state heralding**. (a) Experimental setup used to prepare a heralded photon-number state $\hat{\rho}_s^{(j)}$. (b) Theory schematic of the setup. Due to losses in the idler and signal arms, the resulting state $\hat{\rho}_s^{(j)}$ may be quite different than an ideal photon-number state $|j\rangle$. (c) The measured second-order correlation function $g^{(2)}$ of the state $\hat{\rho}_s^{(j)}$ [grey]. The shaded area is one standard deviation in ten measurement trials. Despite the losses, $\hat{\rho}_s^{(j)}$ has sub-Poissonian statistics ($g^{(2)} < 1$) for $j \geq 1$. Blue circles show expected values for our experimental parameters (here $\eta_s = 0.31$, $\eta_i = 0.39$, $\lambda = 0.80$) and black crosses show the values for an ideal photon-number state [Eq. (2.25)]. The inset shows the measured photon-number distribution used to determine the $g^{(2)}$ for $j = 6$. (d) Theory plot showing the effect of squeezing λ on the photon-number purity $\mathcal{P}_p = \mathrm{Tr}([\hat{\rho}_s^{(j)}]^2)$ of the heralded state [continuous lines] and heralding rate [dashed lines]. Note the log scale on the right axis. We assumed $\eta_i = 0.5$ and a laser repetition rate of 100 kHz.

There are two important remarks regarding the effect of losses on the nonclassicality of $\hat{\rho}_s^{(j)}$. Firstly, the $g^{(2)}$ of $\hat{\rho}_s^{(j)}$ is not affected by η_s [Eq. (2.18)], and rather depends only on η_i and λ. Secondly, the effect of $\eta_i < 1$ on $\hat{\rho}_s^{(j)}$ can be minimized by reducing the squeezing of the SPDC source, i.e. reducing λ [89]. The intuition is that this minimizes the probability that the herald detector under-counted the true number of pairs produced by the SPDC source. However, this comes at the cost of also reducing the heralding rate. In Fig. 2.7(d), we show the trade-off between the photon-number purity $\mathcal{P}_p = \mathrm{Tr}([\hat{\rho}_s^{(j)}]^2)$ and heralding rate as a function of λ for different j values, assuming $\eta_i = 0.5$ and a laser repetition rate of 100 kHz.

2.4.2 Interfering heralded photon-number states

Nonclassical intereference can occur when nonclassical light such as photon-number states are combined on a beam splitter. For example, two indistinguishable single photons incident on different ports of a balanced beam splitter always exit the device from the same port, as first observed by Hong, Ou, and Mandel in 1987 [90]. In other words, one never detects light in both output ports simultaneously and light exits from one of the two ports randomly. This interference phenomenon has no classical explanation and has played a central role in the development of quantum optics [91].

The visibility of the interference between heralded photon-number states depends on their (i) modal purity, (ii) photon-number purity, (iii) indistinguishability, and (iv) a number of more minor experimental imperfections such as detector dark counts and non-ideal beam splitters. Therefore, nonclassical interference measurements provide a general benchmark of the quality of heralded photon-number states.

In Chapter 5, we study the interference of higher-order photon-number states. For now, we focus on the single photon case where Hong-Ou-Mandel interference occurs. We prepare two heralded single photons using the experimental setup shown in Fig. 2.8(a). By using a small squeezing parameter, we maximize their photon-number purity (i.e. minimize the probability of either source producing more than one photon pair). Hence, we assume that the heralded single photons can be described by a statistical mixture of single-photon states in various spectral modes, i.e. $\hat{\rho}_1$ and

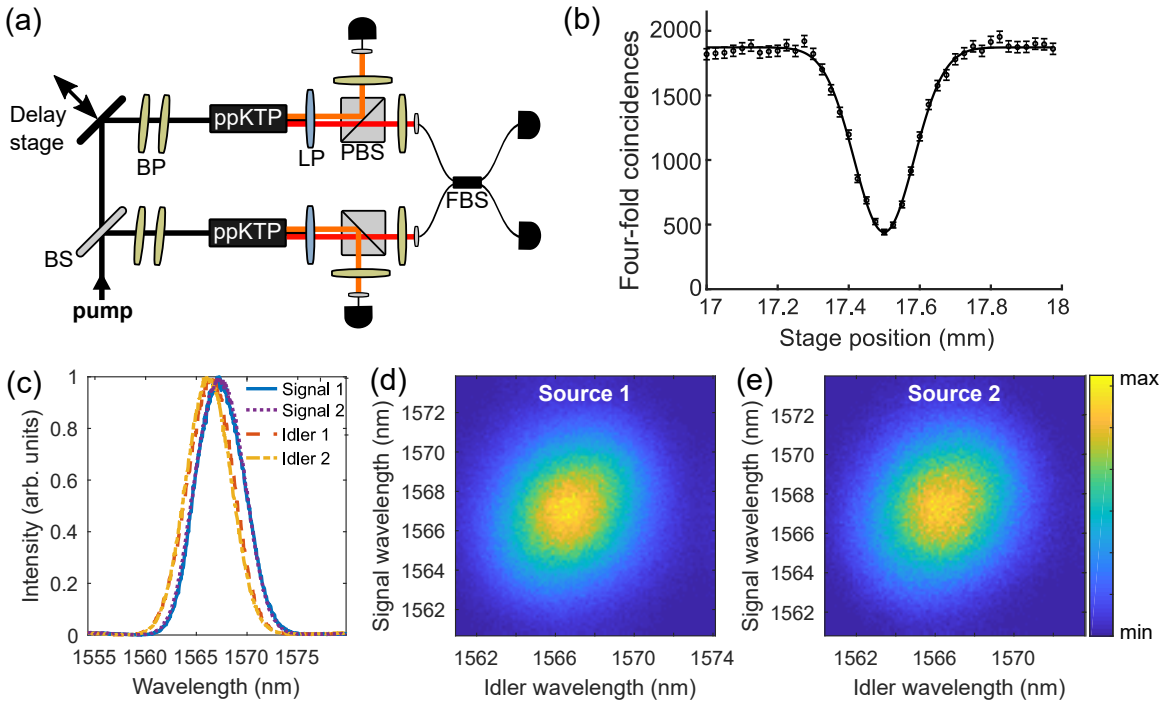

Figure 2.8: **Hong-Ou-Mandel interference measurement.** (a) Experimental setup. We herald a single photon using each source and combine the two on a balanced fiber beam splitter. (b) Measured four-fold coincidences in 30 s as a function of the delay stage position. Errors are one standard deviation assuming Poissonian counting statistics and the continuous line is a Gaussian fit. The visibility of the dip is $\mathcal{V} = 76 \pm 2\%$. (c) Spectrum of each mode in the measurement. The two signal modes have high spectral indistinguishability. (d) and (e) Joint spectral intensity of source 1 and 2, respectively.

$\hat{\rho}_2$ for sources 1 and 2, respectively. The photons are coupled into a polarization-maintaining single-mode fiber beam splitter, and the temporal delay between the two is adjusted using a delay stage. When the photons arrive at the beam splitter at the same time, we observe a dip in the four-fold coincidence rate[7] [Fig. 2.8(b)]. The visibility $\mathcal{V}$ of the dip is given by [67]

$$\mathcal{V} = \frac{C_{max} - C_{min}}{C_{max}} = \mathrm{Tr}(\hat{\rho}_1 \hat{\rho}_2) = \frac{1}{2}\left(\mathrm{Tr}(\hat{\rho}_1^2) + \mathrm{Tr}(\hat{\rho}_2^2) - ||\hat{\rho}_1 - \hat{\rho}_2||\right) \tag{2.26}$$

where C_{min} (C_{max}) is the minimum (maximum) measured coincidence rate. This equation shows the dependence of $\mathcal{V}$ on both the modal purity $\mathcal{P}_m = \mathrm{Tr}(\hat{\rho}_i^2)$ as well as indistinguishability $||\hat{\rho}_1 - \hat{\rho}_2||$ ($||\bullet||$ denotes the trace norm) of the photons. We find that $\mathcal{V} = 76 \pm 2\%$. This value is consistent with the modal purities obtained from a $g^{(2)}$ measurement [Eq. (2.17)], i.e. 0.76 ± 0.001 for source 1 and 0.79 ± 0.001 for source 2. Thus, the interference visibility is limited mainly by the modal purity of the sources. Indeed, the marginal spectra in Fig. 2.8(c) show that the interfering signal modes have a high spectral indistinguishability. Moreover, by replacing the pump with a continuous-wave laser having the signal's center wavelength (1567 nm) and polarization, we measured classical interference fringes with a visibility of over 98% which indicates high polarization and spatial indistinguishability in the interferometer formed by the two beam splitters in Fig. 2.8(a).

How could the modal purity be improved? Although the measured joint spectral intensities [Fig. 2.8(d)-(e)] appear well decorrelated, this measurement is insensitive to spectral phase. Correlations in spectral phase can be reduced by eliminating pump chirp. However, this was likely not the main issue in this measurement since our pump laser produces nearly chirp-free pulses. Another important issue is unguided SPDC processes in the waveguide. These produce uncorrelated photons occupying different spectral modes and hence reduce the modal purity [64]. The rate of such unguided processes depends on the waveguide propagation losses, which is likely the main reason for the reduced modal purity in this measurement compared to the ~ 0.85 obtained

[7] Note that this measurement employed click detectors for convenience since number resolution was not required. For an analogous measurement using TESs, see Chapter 5.

in Sec. 2.3.2 with a different waveguide. Reducing waveguide propagation losses is an active area of research. For example, fabrication techniques such as diamond-blade dicing can produce ridges in an in-diffusion waveguide, leading to stronger mode confinement and lower propagation losses [92].

Chapter 3

Weak-field homodyne detection

3.1 Introduction

There are two main strategies to measure a quantum optical signal. The first is to project the signal onto discrete non-Gaussian photon-number states using click or photon-number-resolving detectors. The second is to combine the signal with a phase reference and perform homodyne detection which projects the signal onto continuous Gaussian field quadrature states [93]. The complementary properties of these two strategies are listed in Table 3.1.

In this chapter, we investigate a hybrid detection strategy known as weak-field homodyne detection that encompasses aspects of both types of detectors. We perform an experiment demonstrating the ability to tune between photon counting and quadrature measurements with a single experimental setup. The regime in-between these two complementary measurement strategies enables novel techniques for characterizing and engineering quantum states of light.

Photon counting	Homodyne
Discrete outcomes	Continuous outcomes
Non-Gaussian	Gaussian
Phase-insensitive	Phase-sensitive

Table 3.1: List of key properties of the conventional detection strategies in quantum optics.

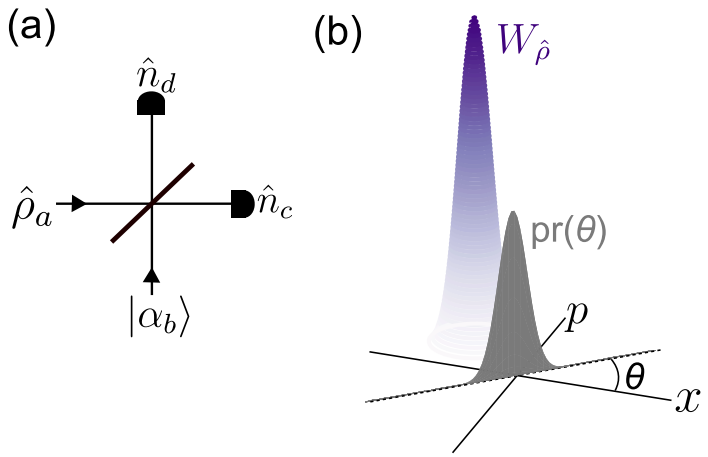

Figure 3.1: **Homodyne detection**. (a) In homodyne detection, a quantum state of light $\hat{\rho}$ is combined with a phase-reference field $|\alpha\rangle$ on a beam splitter. Typically, photodiodes are used to measure the difference in photocurrent which is proportional to $\hat{n}_c - \hat{n}_d$. When the phase reference $|\alpha\rangle$ is a bright classical field, this difference photocurrent determines the quadrature distribution $\mathrm{pr}(\theta)$, where θ is the phase of the reference field. (b) $\mathrm{pr}(\theta)$ is a projection of the Wigner function of $\hat{\rho}$ (i.e. $W_{\hat{\rho}}$) onto an axis at an angle θ from the origin. By repeating this measurement for various θ values, these "shadows" can be used to unambiguously reconstruct the state $\hat{\rho}$ via quantum state tomography.

3.2 Background

3.2.1 Homodyne detection

Homodyne detection is the standard experimental technique to fully characterize quantum states of light. The idea is depicted in Fig. 3.1(a). A quantum state $\hat{\rho}$ is combined with a phase-reference field (i.e. local oscillator) on a balanced beam splitter. The output fields are then detected with photodiodes and the difference photocurrent is recorded, which is proportional to the difference in photon number:

$$\Delta\hat{n} = \hat{n}_c - \hat{n}_d = i(\hat{a}^\dagger\hat{b} - \hat{a}\hat{b}^\dagger). \tag{3.1}$$

where $\hat{a}$ and $\hat{b}$ are the input field annihilation operators. To overcome electronic noise in the photodiodes, one typically uses a phase-reference field in a coherent state having a very large amplitude such as from a bright laser. In this case, we can invoke a classical field approximation [8]

$$\hat{b} \to |\alpha|e^{i\theta}, \tag{3.2}$$

where $|\alpha|$ and θ are the strength and phase of the coherent state, respectively. Eq. (3.1) becomes

$$\Delta\hat{n}_{\text{classical}} = i|\alpha|(\hat{a}^\dagger e^{i\theta} + \hat{a}e^{-i\theta}) = i|\alpha|\hat{X}(\theta) \tag{3.3}$$

where we used the quadrature operator $\hat{X}(\theta) = \hat{a}^\dagger e^{i\theta} + \hat{a}e^{-i\theta}$. By repeating the measurement of $\Delta\hat{n}_{\text{classical}}$ on an ensemble of identical copies of $\hat{\rho}$, homodyne detection determines the quadrature distribution $\text{pr}(\theta) = \text{Tr}(\hat{X}(\theta)\hat{\rho})$ which is the projection of the Wigner function of $\hat{\rho}$ onto an axis at an angle θ from the origin, as shown in Fig. 3.1(b). By measuring quadrature distributions for different values of θ, the Wigner function of $\hat{\rho}$ can be reconstructed via quantum state tomography [94, 95]. Quadrature measurements are also essential for quantum information processing when information is encoded in continuous-variable degrees of freedom of light [10, 96, 97].

3.2.2 Photon-number sensitivity in homodyne

Although homodyne detection and its variants such as heterodyne or eight-port homodyne [98] usually employ photodetectors without photon-number resolution (e.g. regular photodiodes), some early works investigated the potential applications of a homodyne-like detection scheme employing photon-number-resolving detectors. Henceforth, we refer to any such detection scheme as weak-field homodyne detection (WFHD) with the assumption that the phase reference is weak due to the dynamic range of photon-number-resolving detectors. The versatility of WFHD arises from the combination of photon-number resolution and the phase-sensitivity provided by the phase reference.

Perhaps the earliest example of work on WFHD is the Kennedy [99] and Dolinar [100] receivers. These are designed to discriminate between two coherent states $|\pm\alpha\rangle$ with a smaller error than conventional homodyne. The idea is to use a local oscillator to displace the incident light by $+\alpha$ such that the encoding is mapped onto $|2\alpha\rangle$ and $|0\rangle$. By detecting this displaced field with a photon-number-resolving detector and using an adaptive measurement strategy, the Dolinar receiver performs the opti-

mal measurement. These receivers have applications in both classical and quantum communication [11] and have recently been experimentally demonstrated [101–103].

By combining phase-sensitive displacements with photon counting, WFHD can also directly characterize quantum states without having to perform a complete reconstruction, e.g. by measuring the displaced parity operator [104]. This idea was used to characterize quantum states in the microwave domain in the groups of Haroche [105] and Wineland [106], and more recently in the optical domain [107–111].

Finally, WFHD has the unique ability to project light onto phase-sensitive non-Gaussian states, as experimentally demonstrated in Refs. [112–114]. This provides a powerful state engineering tool which is further explored in Chapter 4. Moreover, phase-sensitive non-Gaussian measurements can reveal nonclassical correlations that would be hidden from conventional detection strategies. For example, WFHD can be used to violate a Bell inequality with entangled Gaussian states (e.g. two-mode squeezed vacuum) while photon counting or homodyne alone cannot [115–117].

3.3 Tuning between photon-number and quadrature measurements

The fact that homodyne measures the quadrature operator emerges from the classical field approximation in Eq. (3.2). When does this approximation become valid? Refs. [118, 119] estimate the required $|\alpha|$ to be $|\alpha| \gg N$, where N is the average number of photons in $\hat{\rho}_a$. This condition ensures that photon-number fluctuations in the coherent state are larger than N. If these fluctuations were smaller than N, i.e. $|\alpha| < N$, a measurement of $\Delta\hat{n}$ would reveal some information about $\hat{a}^\dagger\hat{a}$, the photon number of $\hat{\rho}_a$. This information gained about $\hat{a}^\dagger\hat{a}$ comes at the cost of disturbing the measurement of $\hat{X}(\theta)$ since these two operators do not commute.

The phase-reference amplitude $|\alpha|$ provides a knob to transition between a non-Gaussian ($|\alpha| < N$) and Gaussian ($|\alpha| \gg N$) measurement. We briefly mention one potential application for this tunability in optical quantum information processing. Quantum circuits containing only Gaussian elements (i.e. input states, transforma-

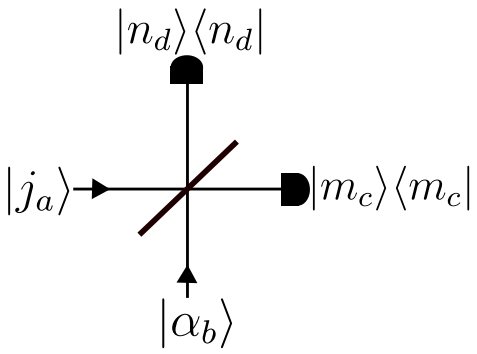

Figure 3.2: **Weak-field homodyne with photon-number state**. A schematic of the problem being considered.

tions, and measurements) can be efficiently simulated on a classical computer and hence are insufficient for quantum computing [120, 121]. Certain quantum information processing protocols introduce non-Gaussianity only in the measurement stage of the circuit in order to enable quantum computational power, such as in measurement-based architectures employing Gaussian cluster states [122] or Gaussian boson samplers [123]. By employing WFHD as the measurement device in such circuits, $|\alpha|$ provides a knob to tune the difficulty with which the circuit can be simulated classically, which could be useful for e.g. verifying the output of the circuit or studying how quantum complexity emerges. We do not investigate this topic further in this thesis but note that it could be interesting for future work.

While some recent experiments have performed quadrature measurements using WFHD [124, 125], no work has yet demonstrated the full tunability of WFHD. That is, no prior experiment achieved both photon counting and quadrature measurements in the same setup. This is the main subject of the remainder of this chapter.

3.3.1 Theory

We investigate the transition in the photon-number difference statistics measured by WFHD in the particular case of a pure photon-number state, $\hat{\rho}_a = |j_a\rangle\langle j_a|$, as shown in Fig. 3.2. Here we will assume that $\hat{\rho}_a$ and $|\alpha_b\rangle$ occupy the same spatio-temporal mode and ignore optical loss. We extend the model below to include mode mismatch and losses in Appendix B. The joint probability of detecting m photons in mode c

and n photons in mode d [i.e. the outcome (m,n)] at the output of the beam splitter, $\mathrm{pr}^{(j,\alpha)}(m,n)$, is given by:

$$\begin{aligned}\mathrm{pr}^{(j,\alpha)}(m,n) &= \left|\langle m_c, n_d | j_a, \alpha_b\rangle\right|^2 \\ &= \frac{1}{m!n!}\left|\langle 0_c, 0_d | \hat{c}^m \hat{d}^n | j_a, \alpha_b\rangle\right|^2,\end{aligned} \tag{3.4}$$

where $\hat{c}$ ($\hat{d}$) is the photon annihilation operator in mode c (d). The input and output modes of the beam splitter are related through the following transformation:

$$\begin{aligned}\hat{c} &= (\hat{a} + i\hat{b})/\sqrt{2}, \\ \hat{d} &= (\hat{b} + i\hat{a})/\sqrt{2},\end{aligned} \tag{3.5}$$

Inserting these expressions into Eq. (3.4), we find:

$$\begin{aligned}\mathrm{pr}^{(j,\alpha)}(m,n) &= \frac{1}{2^{m+n}m!n!}\left|\langle 0_c, 0_d | (\hat{a} + i\hat{b})^m (\hat{b} + i\hat{a})^n | j_a, \alpha_b\rangle\right|^2 \\ &= \frac{1}{2^{m+n}m!n!}\left|\langle 0_c, 0_d | \sum_{l=0}^{m}\sum_{k=0}^{n}\binom{m}{l}\binom{n}{k} i^{l+k}\hat{a}^{m-l+k}\hat{b}^{l+n-k} | j_a, \alpha_b\rangle\right|^2.\end{aligned} \tag{3.6}$$

The non-zero terms in the first sum satisfy $l = m+k-j$. Furthermore, $\hat{b}\,|\alpha_b\rangle = \alpha\,|\alpha_b\rangle$. Using these two facts, Eq. (3.6) can be simplified to:

$$\mathrm{pr}^{(j,\alpha)}(m,n) = \frac{e^{-|\alpha|^2} j!|\alpha|^{2(m+n-j)}}{2^{m+n}m!n!}\left|\sum_{k=0}^{j}\binom{m}{m+k-j}\binom{n}{k}(-1)^k\right|^2, \tag{3.7}$$

and $\mathrm{pr}^{(j,\alpha)}(m,n) = 0$ when $m+n < j$. The difference photon-number statistics are then obtained by summing over all possible outcomes yielding $\Delta n = m - n$:

$$\mathrm{pr}^{(j,\alpha)}(\Delta n) = \sum_{m=\max(0,\Delta n)}^{\infty}\frac{e^{-|\alpha|^2} j!|\alpha|^{2(2m-\Delta n-j)}}{2^{2m-\Delta n}m!(m-\Delta n)!}\left|\sum_{k=0}^{j}\binom{m}{m+k-j}\binom{m-\Delta n}{k}(-1)^k\right|^2. \tag{3.8}$$

Evaluating the sums for some example j values, we find:

$$\mathrm{pr}^{(j,\alpha)}(\Delta n) = \begin{cases} e^{-|\alpha|^2} I_{\Delta n}, & \text{for } j=0 \\ e^{-|\alpha|^2}|\alpha|^{-2}\Delta n I_{\Delta n}, & \text{for } j=1 \\ e^{-|\alpha|^2}|\alpha|^{-4}\left(\left[\Delta n(1+\Delta n)\right) I_{\Delta n} - |\alpha|^{-2} I_{(1-\Delta n)}\right], & \text{for } j=2 \end{cases}$$

where $I_{\Delta n}$ is the modified Bessel function of the first kind of order Δn evaluated at $|\alpha|^2$. Unfortunately, we could not find a closed expression for arbitrary j.

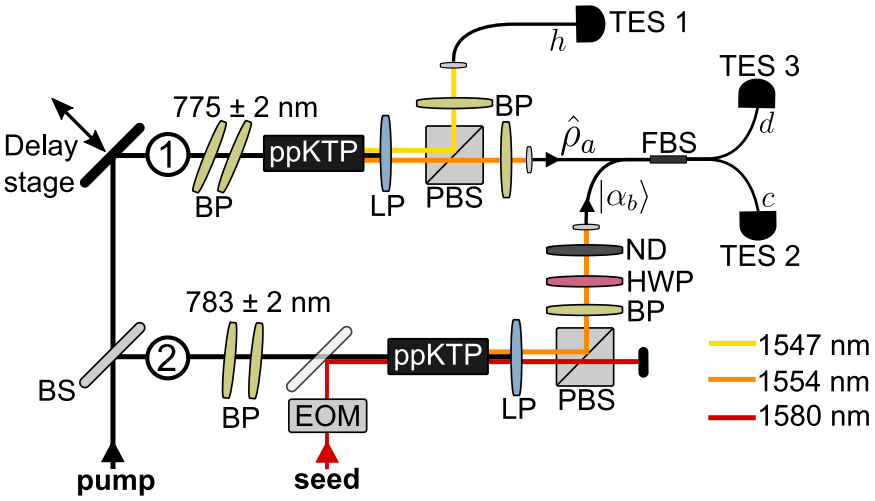

Figure 3.3: **Experimental setup.** Details can be found in the text. BS: beam splitter, BP: bandpass filter, EOM: electro-optic modulator, ppKTP: periodically-poled potassium titanyl phosphate (waveguide), LP: longpass filter, PBS: polarizing beam splitter, HWP: half-wave plate, ND: neutral-density filter, FBS: fiber beam splitter, TES: transition edge sensor.

For $|\alpha| \gg j$, we expect that Eq. (3.8) converges to the statistics obtained by invoking the classical field approximation $\hat{b} \to |\alpha| e^{i\theta}$, namely:

$$\mathrm{pr}^{(j,\alpha)}_{\mathrm{classical}}(\Delta n) = \frac{1}{\sqrt{2\pi}|\alpha|} \frac{1}{2^j j!} \left| H_j\left(\frac{\Delta n}{\sqrt{2}\alpha}\right) e^{-\Delta n^2/4\alpha^2} \right|^2, \tag{3.9}$$

where H_j is a Hermite polynomial of order j. This expression is derived in Ref. [126]. Notably, Eq. (3.9) is simply the quadrature distribution of a j photon-number state scaled by α, i.e. $\Delta n \to \Delta n/\alpha$ [127].

3.3.2 Experimental setup

The experimental setup is shown in Fig. 3.3. The pump is a titanium sapphire oscillator followed by a regenerative amplifier that outputs $\sim$ 30 fs pulses (780 $\pm$ 20 nm [full width at half maximum]) at a rate of 100 kHz. This rate is chosen to accommodate the thermal relaxation time of the TES detectors. The pump pulses are split into two paths, labelled ① and ② in Fig. 3.3.

In path ①, we prepare the signal $\hat{\rho}_a$. The pump is filtered to 775 $\pm$ 2 nm using two angle-tuned bandpass filters. The filtered pump is then coupled into a ppKTP waveguide and generates a two-mode squeezed vacuum state. The pump spectrum is

chosen such that the down-converted signal (1554 nm) and idler (1547 nm) modes are approximately spectrally decorrelated ($g^{(2)} = 1.849 \pm 0.007$ in idler mode). The pump is then discarded with a longpass filter and the orthogonally-polarized signal and idler modes are spatially separated with a polarizing beam splitter. The two modes are sent through a bandpass filter and coupled in fibers. The idler mode is sent directly to a TES detector for heralding, whereas the signal mode is sent to a polarization-maintaining fiber beam splitter. Due to losses and imperfect detection efficiency in the herald mode ($\eta_h = 0.395 \pm 0.002$), we do not herald a pure photon-number state $|j_a\rangle$. Rather, we herald a signal $\hat{\rho}_a^{(j)}$ which is a statistical mixture of photon-number states [Eq. (2.24)]. Despite the losses, $\hat{\rho}_a^{(j)}$ is still a nonclassical signal. Namely, we measure that $\hat{\rho}_a^{(j)}$ has sub-Poissonian photon-number statistics when $j \geq 1$ (see Sec. 2.4).

In path ②, we prepare the coherent state $|\alpha_b\rangle$. The pump is filtered to 783 ± 2 nm and coupled into a second ppKTP waveguide. In contrast to the previous path, we also couple 1580 nm light from a continuous-wave laser in order to seed the down-conversion process. Through difference frequency generation (see Sec. 2.3.1), light with Poissonian photon-number statistics ($g^{(2)} = 1.005 \pm 0.002$) is generated in the polarization mode orthogonal to the seed, i.e. $|\alpha_b\rangle$. The seed and pump spectra are chosen to optimize the spectral overlap between the signal $\hat{\rho}_a$ and $|\alpha_b\rangle$ given that there are small differences between the phase matching properties of the two waveguides. Then, $|\alpha_b\rangle$ is separated from the bright seed light using a polarization beam splitter and bandpass filter. To further minimize the amount of seed light leakage, we carve 5 ns long pulses from the continuous-wave seed laser using an electro-optic modulator. We measured the signal-to-noise ratio in $|\alpha_b\rangle$ (i.e. the total number of photons detected with both seed and pump on divided by the number of photons detected with only the seed on) to be 10^5. $|\alpha_b\rangle$ is sent through a half-wave plate to match its polarization to that of the signal. The intensity $|\alpha|^2$ is adjusted using a neutral-density filter wheel. Finally, $|\alpha_b\rangle$ is coupled into fiber and sent to the fiber beam splitter. The pulses $\hat{\rho}_a^{(j)}$ and $|\alpha_b\rangle$ are temporally overlapped in the fiber beam splitter using a delay stage. The output modes of this beam splitter are then

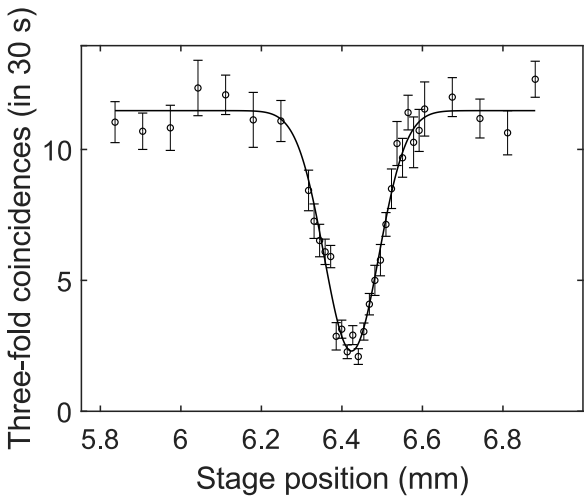

Figure 3.4: **Interference between our signal and phase reference.** When combining a single photon with a coherent state on a beam splitter, the output fields should never both contain a single photon, i.e. $\mathrm{pr}^{(1,\alpha)}(1,1)$ vanishes [Eq. (3.7)]. Here we measure the visibility of this interference effect (using click detectors) to estimate the mode overlap between our signal and phase reference. We find $\mathcal{V} = 0.800 \pm 0.060$. The temporal delay between $\hat{\rho}_a$ and $|\alpha_b\rangle$ is scanned by moving a stage.

sent to two TESs. We measured the total system efficiency (i.e. coupling, transmission and detection efficiencies combined) in modes c and d to be $\eta_c = 0.274 \pm 0.001$ and $\eta_d = 0.354 \pm 0.002$, respectively, using the Klyshko method outlined in Sec. 2.3.3. Since $\hat{\rho}_a^{(j)}$ has no defined phase relative to $|\alpha_b\rangle$, $\mathrm{pr}^{(j,\alpha)}(\Delta n)$ and $\mathrm{pr}^{(j,\alpha)}_{\mathrm{classical}}(\Delta n)$ do not depend on θ and hence we do not require control of θ.

To quantify the mode overlap $\mathcal{M}$ between our phase reference and signal, we measure an interference signal. In theory, when $\hat{\rho}_a$ is a single photon, the probability to detect only one photon at both outputs of the beam splitter, $\mathrm{pr}^{(1,\alpha)}(1,1)$, vanishes [Eq. (3.7)]. In practice, this probability does not vanish due to experimental imperfections such as background counts, the photon-number purity of $\hat{\rho}_a$, and imperfect mode overlap between $\hat{\rho}_a$ and $|\alpha_b\rangle$. Moreover, for this particular measurement we employed nanowire click detectors rather than TESs and measured a three-photon coincidence probability which does not discern between higher-photon events, i.e. $\mathrm{pr}^{(x,\alpha)}(y,z)$ for $x, y, z \geq 1$ are convolved into our interference signal. These higher-photon events were minimized by reducing the pump power and α. For all these reasons, the visibility $\mathcal{V}$ of this interference signal provides a lower bound on $\mathcal{M}$. By scanning the

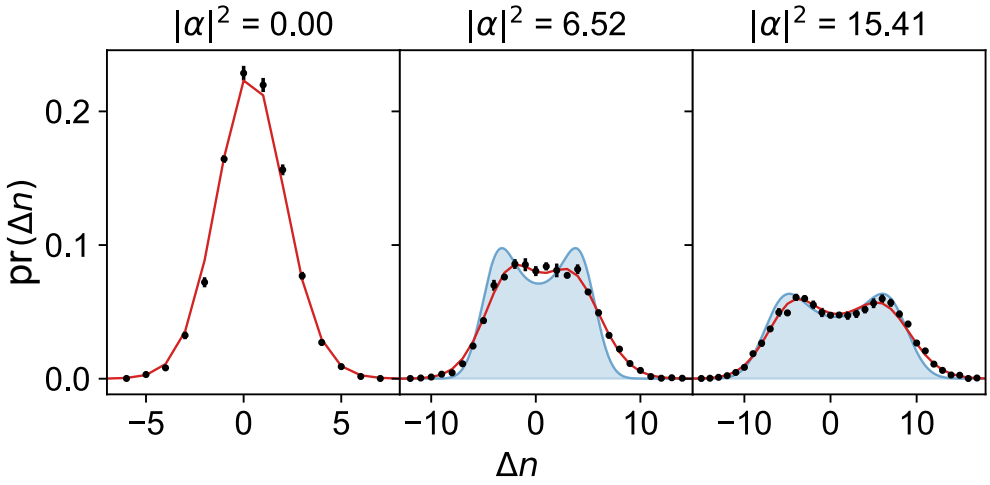

Figure 3.5: **Transition from a photon-number to a quadrature measurement.** We plot the probability $\mathrm{pr}(\Delta n)$ to measure a photon-number difference Δn with the signal $\hat{\rho}_a^{(6)}$. As $|\alpha|^2$ increases, the agreement between the black data points and the expected quadrature distributions (blue regions) improves, indicating that our detector is performing a quadrature measurement. The red curves [blue curves] are calculated from $\mathrm{pr}^{(j,\alpha)}(\Delta n)$ [$\mathrm{pr}^{(j,\alpha)}_{\mathrm{classical}}(\Delta n)$], and include the effects of experimental imperfections (see Appendix B for further details including the model parameters). Error bars represent one standard deviation in 10 trials. Both the red and blue models are discrete; the lines interpolating between model points are merely to distinguish them from the data.

temporal delay between $\hat{\rho}_a$ and $|\alpha_b\rangle$, we measure a Hong-Ou-Mandel-type dip in the three-photon coincidence probability from which we determined an interference visibility of $\mathcal{V} = 0.800 \pm 0.060$ [Fig. 3.4]. We found that our model (see Appendix B) agrees best with the data by using $\mathcal{M} = 0.82$.

3.3.3 Results

In Fig. 3.5, we show the measured photon-number difference statistics for $j = 6$ and three different values of $|\alpha|^2$. The measured statistics [black points] can be compared with the statistics expected from the theory model with and without the classical field approximation, i.e. $\mathrm{pr}^{(j,\alpha)}_{\mathrm{classical}}(\Delta n)$ [blue curves] and $\mathrm{pr}^{(j,\alpha)}(\Delta n)$ [red curves], respectively. Both models include the effects of experimental imperfections such as detection inefficiencies and mode mismatch. For $|\alpha|^2 = 0$, $\mathrm{pr}^{(j,\alpha)}(\Delta n)$ is obtained by projecting $\hat{\rho}_a^{(6)}$ onto photon-number states. In this case, $\mathrm{pr}^{(j,\alpha)}_{\mathrm{classical}}(\Delta n)$ is not defined. For $|\alpha|^2 = 6.52$, the data points agree with $\mathrm{pr}^{(j,\alpha)}(\Delta n)$ but not with $\mathrm{pr}^{(j,\alpha)}_{\mathrm{classical}}(\Delta n)$, indicat-

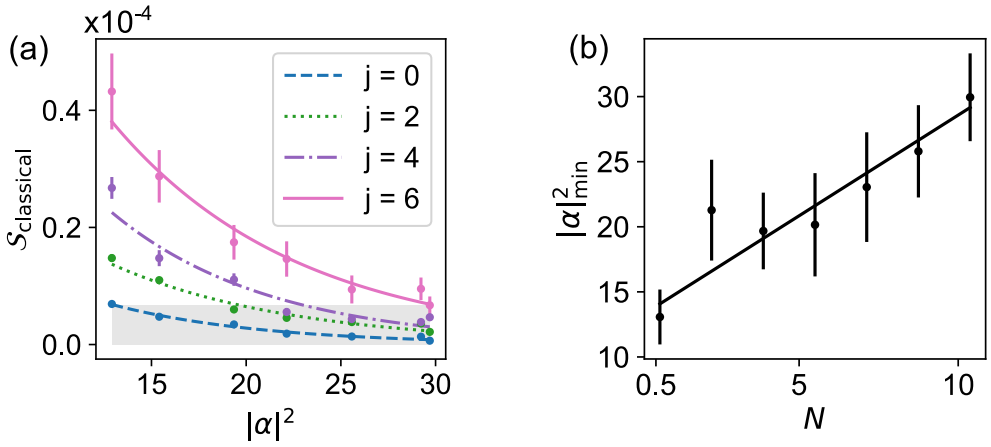

Figure 3.6: **Quantifying the transition towards a quadrature measurement.** (a) We plot $\mathcal{S}_{\text{classical}}$, the discrepancy between our measured data and an ideal quadrature measurement, as a function of $|\alpha|^2$ for various herald outcomes j. As $|\alpha|^2$ increases, our measurement becomes more quadrature-like and so $\mathcal{S}_{\text{classical}}$ decreases. The grey box is the threshold used to define $|\alpha|^2_{\text{min}}$. Error bars are one standard deviation in 10 trials. (b) The minimum coherent state strength, $|\alpha|^2_{\text{min}}$, required for a quadrature measurement. The black line is a linear fit of $|\alpha|^2_{\text{min}}$ as a function of the average photon number in the signal, N. The error bars are obtained from the uncertainty in the fit parameters A and B.

ing that the classical field approximation is not yet valid. However, for $|\alpha|^2 = 15.41$, there is good agreement between the data and both $\text{pr}^{(j,\alpha)}(\Delta n)$ and $\text{pr}^{(j,\alpha)}_{\text{classical}}(\Delta n)$. This suggests that we are projecting $\hat{\rho}_a^{(6)}$ onto quadrature states for a weaker $|\alpha|$ than expected, i.e. before the regime where $|\alpha| \gg N$ [118, 119] (note that $N = 10.4$ for $j = 6$ due to loss in the herald mode).

To understand why, we quantify the transition from $\Delta\hat{n}$ to $\Delta\hat{n}_{\text{classical}}$ by computing the sum of the squared residuals,

$$\mathcal{S}_{\text{classical}} = \frac{1}{\nu}\sum_{\Delta n} |\text{pr}^{(j,\alpha)}_{\text{exp}}(\Delta n) - \text{pr}^{(j,\alpha)}_{\text{classical}}(\Delta n)|^2, \tag{3.10}$$

where ν is the number of data points. $\mathcal{S}_{\text{classical}}$ quantifies the discrepancy between the measured data $\text{pr}^{(j,\alpha)}_{\text{exp}}$ and the classical model $\text{pr}^{(j,\alpha)}_{\text{classical}}(\Delta n)$. Ideally, $\mathcal{S}_{\text{classical}}$ smoothly converges to zero for increasing $|\alpha|^2$ as the validity of the classical field approximation improves. In Fig. 3.6(a), we plot $\mathcal{S}_{\text{classical}}$ for four different herald outcomes j. We found heuristically that an exponential curve adequately models $\mathcal{S}_{\text{classical}}$ for sufficiently large $|\alpha|^2$. Thus, for each j, we fit $\mathcal{S}_{\text{classical}}$ to $A\exp(-B|\alpha|^2)$ from which we determine $|\alpha|^2_{\text{min}}$, the coherent state strength required to reach below

$\mathcal{S}_{\text{classical}} = 6.7 \times 10^{-6}$. This threshold corresponds to the sum of the squared residuals obtained with the quantum model [i.e. replacing $\text{pr}^{(j,\alpha)}_{\text{classical}}(\Delta n)$ with $\text{pr}^{(j,\alpha)}(\Delta n)$ in Eq. (3.10)], averaged over all j and $|\alpha|$. We plot $|\alpha|^2_{\text{min}}$ for $j = 0$ to 6 in Fig. 3.6(b). Interestingly, we observe an approximately linear scaling between $|\alpha|^2_{\text{min}}$ and the average photon-number in the signal, N, instead of a quadratic scaling [119, 128]. We believe this relaxed requirement on $|\alpha|^2_{\text{min}}$ is due to our detector inefficiency which smooths the fine features in the quadrature distribution of $\hat{\rho}^{(j)}_a$. This reasoning agrees with the findings of Ref. [129], which showed that a smaller $|\alpha|^2_{\text{min}}$ is required for states with smooth quadrature distributions such as coherent states. Thus, the transition from photon-number to quadrature measurement in Fig. 3.5 occurred for a weaker $|\alpha|$ than might be expected (i.e. before the regime $|\alpha| \gg N$) since the quadrature distribution of $\hat{\rho}^{(6)}_a$ is smooth.

3.4 State engineering

So far, we have demonstrated that WFHD can tune between performing photon-number and quadrature measurements. Here, we show it can also be used as a state engineering tool by projecting one part of a photon-number entangled state onto a particular measurement basis, thus steering the possible measurement outcomes on the other part of the entangled state. The concept is shown schematically in Fig. 3.7(a). Mode a of the two-mode squeezed vacuum state

$$|\Psi_{ha}\rangle = \sum_{n=0}^{\infty} \lambda^n |n_h, n_a\rangle \tag{3.11}$$

is sent to the WFHD. The detector projects mode a onto a state $|\chi_a\rangle$ which depends on the detection outcome (m, n) and α [112]:

$$|\chi_a\rangle = \frac{e^{-|\alpha|^2/2}}{\sqrt{2^{(m+n)} m! n!}} \left(\alpha - i\hat{a}^\dagger\right)^m \left(\hat{a}^\dagger - i\alpha\right)^n |0_a\rangle \,. \tag{3.12}$$

This measurement transforms mode h to the state $|\psi_h\rangle = \mathcal{N} \langle\chi_a|\Psi_{ha}\rangle$, where $\mathcal{N}$ is a normalization factor. Many different classes of states $|\psi_h\rangle$ can be heralded since $|\chi_a\rangle$ can be continuously tuned between photon-number and quadrature-like states.

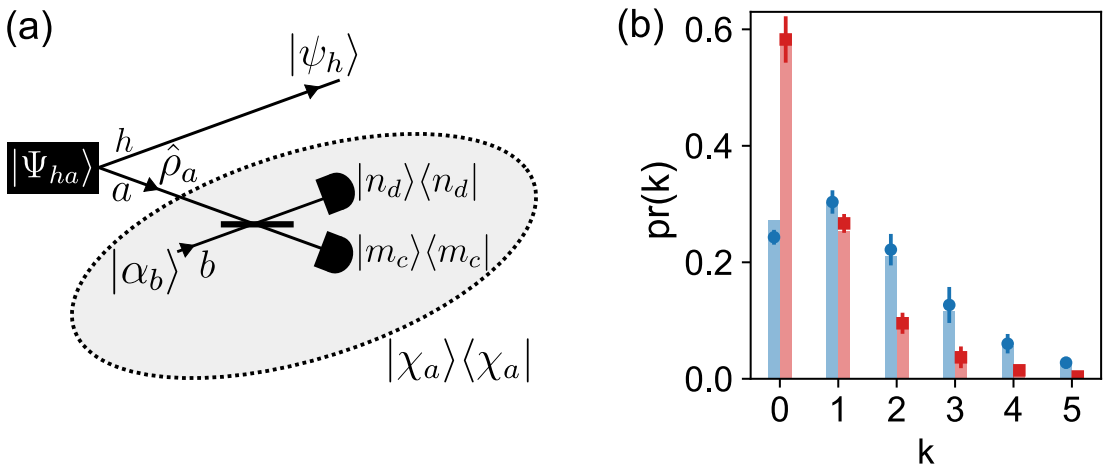

Figure 3.7: **State engineering using weak-field homodyne.** (a) A schematic of the concept. The weak-field homodyne detector, shown in the grey circle, projects the signal $\hat{\rho}_a$ onto the state $|\chi_a\rangle$ that depends on m, n, and α. (b) Measured photon-number distribution of the state in the herald mode $\mathrm{pr}(k) = |\langle k_h|\psi_h\rangle|^2$ conditioned on obtaining the detection outcome $(m,n) = (6,0)$ when $|\alpha|^2 = 15.41$. The blue circles are measured when $\hat{\rho}_a$ and $|\alpha_b\rangle$ are temporally overlapped and thus interfere at the beam splitter. The red squares are measured when there is no temporal overlap between the two. Error bars are the standard deviation in 10 trials. The bars are theoretical predictions.

This versatility makes WFHD a powerful state engineering tool. For example, in Chapter 4 we show that $|\psi_h\rangle$ can have nearly perfect fidelity with a Schrödinger cat state $|\alpha\rangle + |-\alpha\rangle$ of arbitrary amplitude α.

3.4.1 Results

In our experiments, we do not have control over the phase θ of our local oscillator since the pump and seed lasers are not phase-locked. Thus we do not have the ability to fully characterize $|\psi_h\rangle$. As such, we only present a proof-of-principle demonstration of the state engineering concept here. We consider the detection outcome $(m,n) = (6,0)$ when $|\alpha|^2 = 15.4$. The measured photon-number distribution $\mathrm{pr}(k) = |\langle k_h|\psi_h\rangle|^2$ is shown in Fig. 3.7(b), which we use to calculate the second-order correlation function $g^{(2)} = \sum_k (k^2 - k)\mathrm{pr}(k)/(\sum_k k\mathrm{pr}(k))^2$. When $\hat{\rho}_a$ and $|\alpha_b\rangle$ are not temporally overlapped (using a temporal delay much smaller than the detection window), the two do not interfere and $\mathrm{pr}(k)$ is a thermal-like distribution (red squares, $g^{(2)} = 1.59 \pm 0.15$). This is because the average number of photons in mode b (15.4) is much larger than in mode a (1.74), and so the detection outcome provides little information about the

number of photons in mode a. In contrast, when $\hat{\rho}_a$ and $|\alpha_b\rangle$ are temporally overlapped, pr(k) changes drastically and resembles a Poisson distribution (blue circles, $g^{(2)} = 1.19 \pm 0.11$). This demonstrates that the heralded state is strongly modified by the interference between $\hat{\rho}_a$ and $|\alpha_b\rangle$.

3.5 Conclusions

Weak-field homodyne detection is an old idea in quantum optics that has numerous applications, notably in state characterization and engineering. However, experimental demonstrations of these ideas have been hindered by limitations in the efficiency, noise, and dynamic range of photon-number-resolving detectors. By using transition edge sensors, we were able to experimentally demonstrate the ability to tune between photon number and quadrature measurements with quantum signals having up to 11 photons.

Another achievement of our experiment is performing state engineering using weak-field homodyne detection for the first time. In particular, we showed that the photon-number distribution of a state heralded using weak-field homodyne can be modified by the interference between the local oscillator and the signal. This paves the way towards applications in hybrid discrete- and continuous-variable quantum information processing protocols [130]. For example, in the next chapter we show that weak field homodyne can be used to herald two and four-component Schrödinger cat states. An exciting prospect would be to verify the nonclassical features of this heralded state using a second instance of a weak-field homodyne detector. This second weak-field homodyne detector could project the heralded state directly onto nonclassical phase-sensitive states thereby enabling a more efficient characterization than with regular homodyne detection [109, 111, 131]. Moreover, the same experimental setup (i.e. a weak-field homodyne detector in each mode of a two-mode squeezed vacuum state) can certify the quantum nature of the correlations in an entangled Gaussian state by testing a Bell-type inequality [114–117, 132].

Chapter 4

An even-parity detector

4.1 Introduction

By counting the number of photons in a field, one can determine a fundamental property of the field known as parity. If a field has an even (odd) number of photons, it is said to have even (odd) parity. With the exception of the vacuum state, fields in classical (e.g. coherent, thermal) states possess uncertainty in their parity, i.e. they have a non-zero probability to have both even and odd photon numbers. Conversely, states of light with a definite parity have nonclassical features. For example, single-mode squeezed vacuum is a superposition of only even photon numbers and has reduced quantum fluctuations in its electric field compared to classical light [133]. This reduction in noise makes squeezed vacuum a valuable resource for optical quantum information processing [10, 11] and quantum sensing [134]. Other notable examples of definite parity states that have found uses in quantum technologies include Schrödinger cats [135], Holland-Burnett [136], and Gottesman-Kitaev-Preskill states [137]. The ability to prepare these and other definite parity optical states in a scalable and robust manner is highly desirable for developing quantum technologies. To this end, in this chapter we discuss a novel technique for preparing a wide range of even-parity states using photon-number-resolving detectors. The contents of this chapter are theoretical ideas and have yet to be experimentally demonstrated.

4.2 Parity in fault-tolerant information encoding

We briefly discuss one particularly important application of definite parity states which is fault-tolerant information encoding. This idea is used in error-correction schemes for both classical and quantum information encodings. Consider the following example. A common error in both classical and quantum systems is the bit flip $0 \leftrightarrow 1$. A simple way to encode information in a way that is robust to the bit flip is to use a repetition code in which a logical bit is encoded as N redundant physical bits, e.g. $0 \rightarrow 00000$ for $N = 5$. If any of the physical bits suffer a bit-flip error, the definite parity is broken which signals that an error has occurred. The logical bit is taken to be the dominant value of the physical bits.

While there are numerous ways of encoding quantum information in light, the relevant method for this chapter is a continuous-variable encoding where information is encoded in the quadratures of light. Because this is an infinite dimensional space, fault-tolerance can be achieved without the need of multiple physical systems. Consider a simple example where we encode a logical qubit as the following superposition of photon-number states [138]:

$$\begin{aligned} |0_L\rangle &:= (|0\rangle + |4\rangle)/\sqrt{2} \\ |1_L\rangle &:= |2\rangle \,. \end{aligned} \tag{4.1}$$

As before, Eq. (4.1) encodes information in definite parity states. An error caused by e.g. single photon loss can be easily detected by counting an odd number of photons in the field. There are of course many types of errors that can occur besides single photon loss, and there are an infinite number of qubit encodings such as Eq. (4.1) that can be used. Developing robust and feasible quantum error correction codes is an active area of research that dates back to the 1990s [138–140] . The two leading proposals for encoding a logical qubit in a continuous-variable space are four-component Schrödinger cat states [141, 142] and Gottesman-Kitaev-Preskill states [137]. Such states have been experimentally prepared in the microwave domain with trapped-ion [143] and superconducting [144, 145] systems, but not yet in the optical domain. We now turn to our proposal which can be used to prepare a wide range of states in

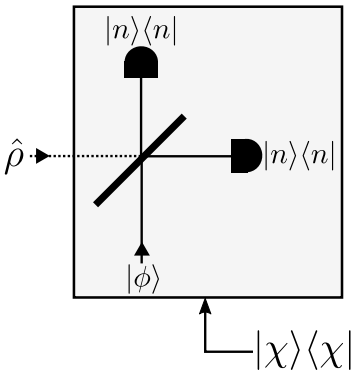

Figure 4.1: **Even-parity detector concept.** Conditioned on obtaining the detection outcome (n, n), the composite detector shown in the grey box performs the projective measurement $|\chi\rangle\langle\chi|$ on the input state $\hat{\rho}$. The state $|\chi\rangle$ contains only even photon-number terms whose amplitudes are controlled by $|\phi\rangle$.

superpositions of even-photon number states including four-component Schrödinger cats.

4.3 Concept

We begin by describing the even-parity detector which is shown in the grey box of Fig. 4.1(a). An "input" state $\hat{\rho}$ is combined with an ancillary "control" state $|\phi\rangle$ on a balanced beam splitter. We assume that $\hat{\rho}$ is arbitrary. The control state is a general pure state, which can be written in the photon-number basis as

$$|\phi\rangle = \sum_{m=0}^{\infty} c_m |m\rangle \tag{4.2}$$

with $\sum_m |c_m|^2 = 1$. The outputs of the beam splitter are then sent to photon-number-resolving detectors which we assume to have perfect efficiency for now. The joint probability to measure n photons in both output ports, i.e. the outcome (n, n), is given by

$$\mathrm{pr}(n, n) = \left\langle n, n \left| \hat{U} \left[\hat{\rho} \otimes |\phi\rangle\langle\phi| \right] \hat{U}^\dagger \right| n, n \right\rangle \tag{4.3}$$

where $\hat{U}$ is the balanced beam splitter unitary operator. Re-writing Eq. (4.3) as $\mathrm{pr}(n, n) = \langle\chi|\hat{\rho}|\chi\rangle$, it becomes clear that the measurement device is described by a projector $|\chi\rangle\langle\chi|$ acting on the input state $\hat{\rho}$ when the detection outcome is (n, n).

The unnormalized projected state $|\chi\rangle$ is given by

$$|\chi\rangle = \langle\phi|\hat{U}^\dagger|n,n\rangle = \sum_{j=0}^{2n} c^*_{2n-j} A_{j,n} |j\rangle\,, \tag{4.4}$$

where

$$\begin{aligned} A_{j,n} &= \langle j, 2n-j|\hat{U}|n,n\rangle \\ &= \begin{cases} \left(\frac{i}{2}\right)^n \frac{\sqrt{(2n-j)!(j)!}}{(j/2)!(n-j/2)!} & \text{for even } j \\ 0 & \text{for odd } j \end{cases} \end{aligned} \tag{4.5}$$

is the matrix element of the beam splitter operator [127]. As one might expect, $|\chi\rangle$ depends on the photon-number coefficients c_{2n-j} of the control state. Perhaps more surprisingly, $|\chi\rangle$ consists only of even photon-numbers. This effect can be understood by considering our device in reverse. When $|n,n\rangle$ impinges on a beam splitter, a pairing interference effect causes both output ports to only contain even-photon numbers, much like in Hong-Ou-Mandel interference [90]. This even-parity state $\hat{U}\,|n,n\rangle$ was first discussed in Ref. [146] but is commonly referred to as the Holland-Burnett state after the work of Ref. [136]. By post-selecting the detection outcome (n,n) at the beam splitter output, our even-parity detector destructively projects the two-mode input of the beam splitter onto the Holland-Burnett state with the decomposition into the photon-number basis given by $A_{j,n}$ [Eq. (4.5)].

In our case, one of the inputs of the beam splitter is the control state $|\phi\rangle$. As a result, the other input, $\hat{\rho}$, is projected onto an even-parity state $|\chi\rangle$ whose photon-number coefficients are determined by c_{2n-j} of the control state as well as $A_{j,n}$ of the Holland-Burnett state.

We now consider the effects of imperfect detection efficiency on our scheme. Suppose both photon-number-resolving detectors in Fig. 4.1(a) have an efficiency η. Following Eq. (2.1), the joint probability $\mathrm{pr}(n,n)$ [Eq. (4.3)] becomes:

$$\begin{aligned} \mathrm{pr}(n,n) = &\sum_{x=n}^{\infty}\sum_{y=n}^{\infty} \binom{x}{n}\binom{y}{n} \eta^{2n}(1-\eta)^{x-n}(1-\eta)^{y-n} \\ &\times \mathrm{Tr}\left(|x,y\rangle\langle x,y|\,\hat{U}\hat{\rho}\otimes|\phi\rangle\langle\phi|\,\hat{U}^\dagger\right) \\ \equiv &\,\mathrm{Tr}\left(\hat{\Lambda}^n(\eta)\hat{\rho}\right). \end{aligned} \tag{4.6}$$

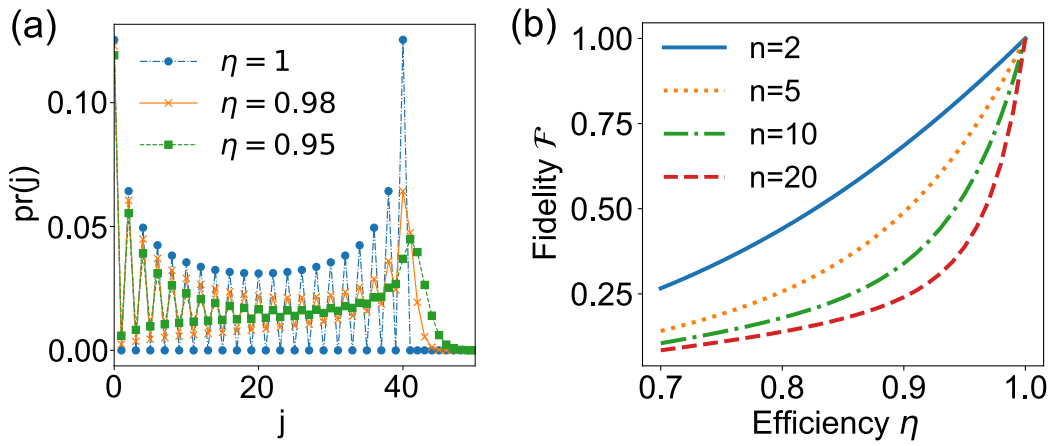

Figure 4.2: **Effect of imperfect detection efficiency.** (a) The photon-number distribution $\mathrm{pr}(j)$ of the even-parity detector when the detectors have an efficiency η, i.e. $\mathrm{pr}(j) = \langle j|\hat{\Lambda}^n(\eta)|j\rangle$. We assume $n = 20$ and $c_m \equiv 1$. For $\eta < 1$, odd photon-numbers contribute to $\mathrm{pr}(j)$. (b) The fidelity $\mathcal{F} = \langle\chi|\hat{\Lambda}^n(\eta)|\chi\rangle$ as a function of detection efficiency η for various values of n.

The even-parity detector projects the input state $\hat{\rho}$ no longer onto a single state $|\chi\rangle$, but rather onto a statistical mixture of states $\hat{\Lambda}^n(\eta)$ which is given by:

$$\hat{\Lambda}^n(\eta) = \sum_{x=n}^{\infty}\sum_{y=n}^{\infty}\binom{x}{n}\binom{y}{n}\eta^{2n}(1-\eta)^{x-n}(1-\eta)^{y-n}\,|\chi^{(x,y)}\rangle\,\langle\chi^{(x,y)}|\,, \tag{4.7}$$

where $|\chi^{(x,y)}\rangle = \langle\phi|\hat{U}^\dagger|x,y\rangle$, which is a generalization of Eq. (4.4).

In Fig. 4.2(a), we plot the photon-number distribution of the imperfect even-parity detector, $\mathrm{pr}(j) = \langle j|\hat{\Lambda}^n(\eta)|j\rangle$ when $n = 20$ and $c_m = 1$ for all m, i.e. a control state with a flat photon-number distribution. Odd photon-number terms quickly begin to contribute to $\mathrm{pr}(j)$ for $\eta < 1$. To further quantify the effect of loss, we numerically compute[1] the fidelity between $\hat{\Lambda}^n(\eta)$ and the ideal projector $|\chi\rangle\langle\chi|$ using $\mathcal{F} = \langle\chi|\hat{\Lambda}^n(\eta)|\chi\rangle$ [Fig. 4.2(b)]. We see that $\mathcal{F}$ depends strongly on detection efficiency, however less so for smaller n values. This is expected since the probability of the detectors having under-counted at least one photon scales as $(1-\eta)n$, and hence the effects of imperfect efficiency begin to kick in for $(1-\eta)n \gtrsim 1$. As a reminder, transition edge sensor detectors can detect up to ~ 20 photons with $> 95\%$ efficiency [55].

[1]For the numerical computation, we used the Python packages *Scipy* and *Qutip* [147]. We generally truncated the Hilbert space to $N = 100$.

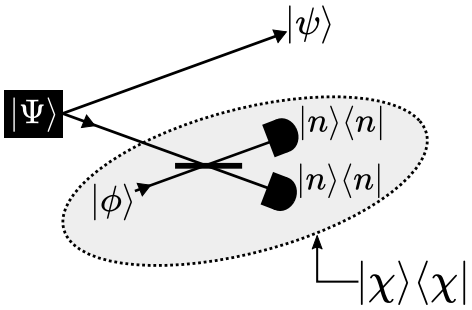

Figure 4.3: **Even-parity state engineering.** The even-parity detector (shown in grey circle) projects one of the modes of a two-mode squeezed vacuum state $|\Psi\rangle$ onto the state $|\psi\rangle = \langle\chi|\Psi\rangle$. Just like $|\chi\rangle$, $|\psi\rangle$ is an even-parity state whose photon-number amplitudes are controlled by $|\phi\rangle$. This scheme can be viewed either as remote state preparation of the state $|\chi\rangle$ or as partial teleportation of the state $|\phi\rangle$.

4.4 State engineering using the even-parity detector

In order to use the even-parity detector for quantum state engineering, we introduce an entangled resource state $|\Psi\rangle$ and apply the detector to one of its mode [Fig. 4.3]. The goal is to remotely prepare a (possibly imperfect) copy of the state $|\chi\rangle$. Consider the photon-number-correlated two-mode squeezed vacuum state,

$$|\Psi\rangle = \sqrt{1-\lambda^2}\sum_{k=0}^{\infty}\lambda^j\,|k,k\rangle\,, \tag{4.8}$$

where $\lambda = \tanh(\zeta)$ determines the squeezing parameter ζ which we assume to be positive-real without loss of generality. Such states can be prepared using various nonlinear optical processes such as spontaneous parametric down-conversion, as discussed in Sec. 2.2.3. By sending one of the modes of $|\Psi\rangle$ to the even-parity detector, the second mode is projected onto the unnormalized state

$$|\psi\rangle = \langle\chi|\Psi\rangle = \sqrt{1-\lambda^2}\sum_{j=0}^{2n}c_{2n-j}\lambda^j A^*_{j,n}\,|j\rangle\,. \tag{4.9}$$

Note that $|\psi\rangle$ is the same as $|\chi\rangle$ [Eq. (4.4)] except for the factor of λ^j inside the summation due to the finite squeezing, i.e. $\lambda \neq 1$. In some cases, it is possible to compensate this effect of finite squeezing when λ is known by changing the control state coefficients $\{c_m\}$ appropriately. In the next section, we use this idea to prepare Schrödinger cat states.

4.4.1 Two-component cats

Two-component even Schrödinger cat states (henceforth "cat states") are defined by:

$$|\text{cat}_\beta\rangle = \frac{1}{\sqrt{2(1+e^{-2|\beta|^2})}}\left(|\beta\rangle + |-\beta\rangle\right), \tag{4.10}$$

where $|\beta\rangle$ is a coherent state of amplitude β. In the limit of large β, $|\beta\rangle$ and $|-\beta\rangle$ play the role of the "alive" and "dead" cats in Schrödinger's famous Gedankenexperiment [135] in the sense that Eq. (4.10) is a superposition of two macroscopic and distinguishable classical states. Cat states have been extensively studied in quantum physics due to their foundational importance [17, 18, 148–154] and their applications in quantum information processing [144, 145, 155–159]. For example, quantum information can be encoded in the qubit $|\pm\beta\rangle$ (with non-orthogonality error $|\langle\beta|-\beta\rangle|^2 = e^{-4|\beta|^2}$) which is convenient due to the simplicity of preparing and manipulating coherent states. However, for most tasks, including computing [157], it is essential to also be able to prepare the qubit in superposition states like $|\text{cat}_\beta\rangle$.

There are a number of existing schemes in the literature for preparing cat states in the optical domain. For example, Ref. [23] showed that subtracting photons from a single mode squeezed vacuum state prepares approximate cat states for small β. This scheme was experimentally implemented by the group of P. Grangier in Ref. [160]. Shortly after, the same group showed that arbitrarily large cat states can be prepared by mixing a photon-number state $|n\rangle$ with vacuum on a beam splitter and performing a conditional homodyne measurement in one output port [161]. The size of the photon-number state n determines the size of the cat.

Besides the probabilistic measurement-based approaches mentioned above, there are also deterministic schemes employing optical nonlinearities. One of the earliest proposals to prepare a cat state is to use a Kerr nonlinearity [162], but this has yet to be experimentally demonstrated. Another scheme based on the strong coupling between an optical cavity field and a single atom has been recently demonstrated in Ref. [19].

In principle, our even-parity detector can be used to engineer cat states of arbitrary size with nearly perfect fidelity. To understand why, consider the following example.

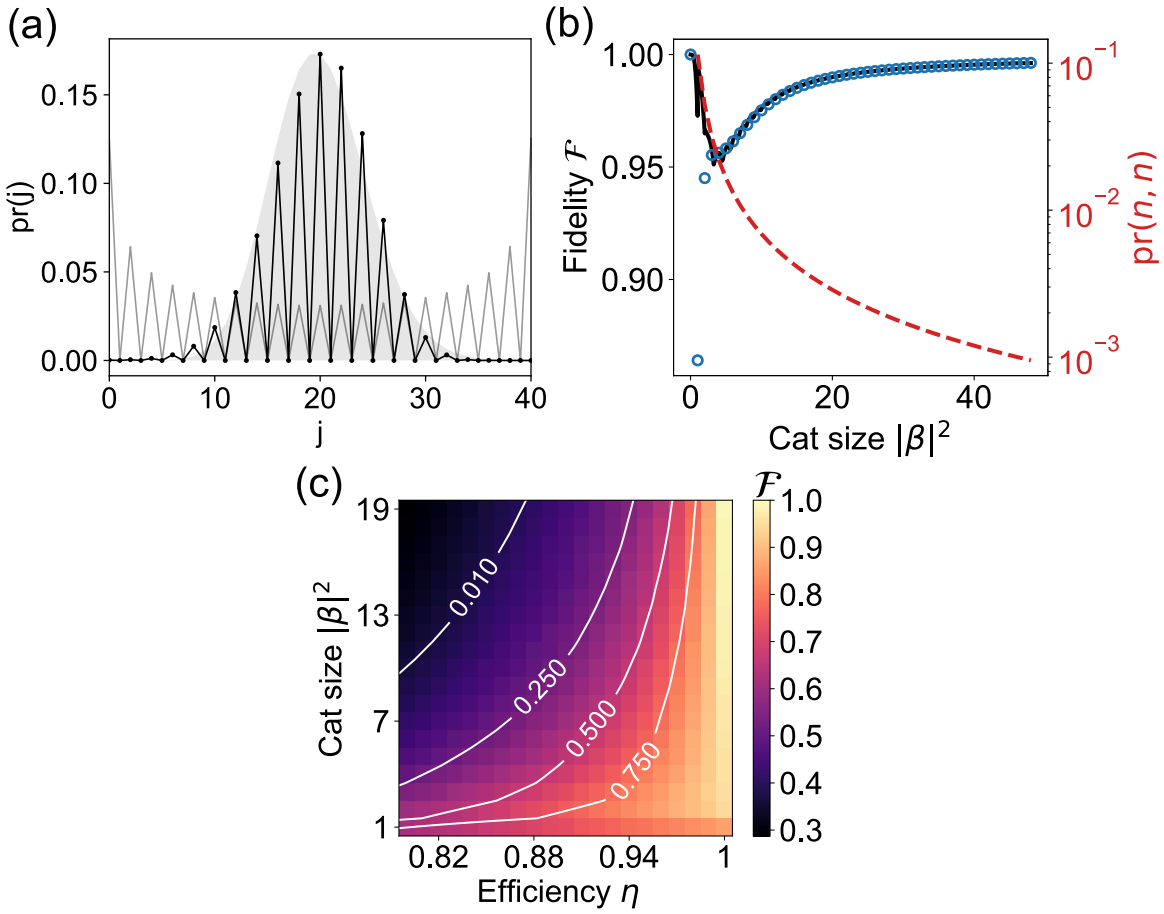

Figure 4.4: **Engineering two-component cat states.** (a) Example case of $n = 20$ and $|\phi\rangle = |\beta\rangle$, a coherent state with amplitude $\beta = \sqrt{20}$. The photon-number distribution $|\langle j|\chi\rangle|^2$ (black line) approximates that of the ancilla input $|\langle j|\phi\rangle|^2$ (grey area) with the odd photon-number terms eliminated. The grey line shows the Holland-Burnett coeffficients $|A_{j,n}|^2$ [Eq. (4.5)]. Note that the distributions are discrete and the lines are merely to guide the eye. (b) The fidelity $\mathcal{F}$ of the cat state prepared by our scheme, $|\psi_{\text{cat}}\rangle$, with respect to the ideal state $|\text{cat}_\beta\rangle$. The blue circles are obtained from Eq. (4.13) for $|\beta|^2 \in \mathbb{N}$. The continuous line is obtained from a numerical optimization of the parameters α and n used in our scheme. $\mathcal{F} \to 1$ for increasing cat size. The dip for small cats is due to the non-flatness of $A_{j,n}$ for small n. The red dashed line shows the probability $\text{pr}(n, n)$ of successfully heralding $|\psi_{\text{cat}}\rangle$ using the optimal squeezing parameter. (c) The fidelity obtained with imperfect detection efficiency η for various cat sizes when $\lambda = 0.82$ (10 dB of squeezing). White contour lines indicate the normalized volume of negativity in the prepared cat state's Wigner function, a measure of its nonclassicality (see text for details).

In Fig. 4.4(a), we plot the photon-number distribution of the detected state $|\chi\rangle$ when the control state is a coherent state $|\beta\rangle$ with $|\beta|^2 = n = 20$. Notice that $|\chi\rangle$ is approximately determined by only the even photon-number terms in $|\beta\rangle$, i.e. the odd photon-number terms vanish. This symmetrization occurs for two reasons. Firstly, the photon-number distribution of $|\beta\rangle$, i.e. $|c_j|^2 = e^{-n}n^j/j!$, is centered and localized on the flat portion of the photon-number distribution $|A_{j,n}|^2$ of the Holland-Burnett state, as shown in Fig. 4.4(a). The emergence of this flat portion can be understood by applying Stirling's approximation to Eq. (4.5):

$$\begin{aligned} A_{j,n} &\approx \frac{i^n}{\sqrt{\pi}} \frac{1}{[(j/2)(n-j/2)]^{1/4}} \\ &\approx \sqrt{\frac{2}{n\pi}} i^n \left(1 + \frac{1}{4n^2}(j-n)^2\right) + \mathcal{O}(j-n)^4, \end{aligned} \tag{4.11}$$

where in the second line we Taylor expanded $A_{j,n}$ to second order around $j = n$. In other words, for $j - n \sim \sqrt{n}$ (which is standard deviation of $|c_j|^2$), the relative variation of $A_{j,n}$ is on a scale of $1/4n$.

Secondly, $|c_j|^2$ is approximately symmetric about the detection outcome $n = 20$, i.e. $c_j \approx c_{2n-j}$. As a result, the state $|\chi\rangle$ [Eq. (4.4)] is given by eliminating the odd photon-number terms of $|\beta\rangle$ while leaving the even terms approximately unchanged. This operation results in $|\chi\rangle \approx |\beta\rangle + |-\beta\rangle$ since the even (odd) photon-number terms in $|\beta\rangle$ and $|-\beta\rangle$ have equal (opposite) signs.

While $|\chi\rangle$ closely resembles $|\text{cat}_\beta\rangle$, the remotely prepared state $|\psi\rangle$ would not have the desired photon-number distribution in the realistic scenario of finite squeezing. As mentioned earlier, one can generally compensate for this effect by carefully choosing the control state coefficients. For cat states this compensation is experimentally easy since one can simply choose the coherent control state $|\phi\rangle = |\alpha\rangle$ with the amplitude $\alpha = \beta\lambda$. In this case, given the detection outcome (n, n), we prepare the state

$$\begin{aligned} |\psi_{\text{cat}}\rangle &= \mathcal{N} \sum_{j=0}^{2n} \frac{\alpha^{2n-j}\lambda^j}{\sqrt{(2n-j)!}} A^*_{j,n} |j\rangle \\ &= \mathcal{N}\lambda^{2n} \sum_{j=0}^{2n} \frac{\beta^{2n-j}}{\sqrt{(2n-j)!}} A^*_{j,n} |j\rangle , \end{aligned} \tag{4.12}$$

where $\mathcal{N}$ is a normalization factor. To maximize the fidelity $\mathcal{F} = |\langle\psi_{\text{cat}}|\text{cat}_\beta\rangle|^2$, one should generally post-select on the detection outcome n to be the closest integer to $|\beta|^2$. This condition ensures that the photon-number distribution of $|\psi_{\text{cat}}\rangle$ is centered on the flat portion of $A_{j,n}$. In the particular case when the cat size $|\beta|^2$ is exactly an integer, i.e. $|\beta|^2 = n$, the fidelity is given by

$$\mathcal{F} = \frac{2^{2n+1}e^{-n}}{(1+e^{-2n})}\left(\sum_{k=0}^{n}\binom{n}{k}^2\frac{(2k)!}{n^{2k}}\right)^{-1}. \tag{4.13}$$

This fidelity asymptotically approaches unity with increasing cat size, as shown by blue circles in Fig. 4.4(b). For small $|\beta|^2$ (and hence small n), $A_{j,n}$ is not flat, causing the dip in the fidelity. Further improvement of the fidelity for small $|\beta|^2$ can be obtained through numerical optimization[2] of the parameters α and n. The optimized fidelity is shown by the black line in Fig. 4.4(b). The small oscillations are due to discrete nature of the parameter n.

The effect of imperfect detectors on $\mathcal{F}$ can be numerically calculated using $\hat{\Lambda}^n(\eta)$. The result is shown in Fig. 4.4(c). On the same plot, white contour lines indicate the volume of negativity V, which is a measure of nonclassicality obtained by integrating the negative regions of the state's Wigner function. For a state $\hat{\rho}$ with Wigner function $W_{\hat{\rho}}(x,p)$, V is given by [9]

$$V = \frac{1}{2}\iint dxdp\,(|W_{\hat{\rho}}(x,p)| - W_{\hat{\rho}}(x,p)) = \frac{1}{2}\iint dxdp|W_{\hat{\rho}}(x,p)| - \frac{1}{2} \tag{4.14}$$

where the second line follows from the normalization of $W_{\hat{\rho}}(x,p)$. We normalize V to that of an ideal cat state of equal size, i.e. 1 is the maximum amount of negativity for a cat state of that size, while 0 is no negativity.

Since our scheme requires post-selecting onto a single outcome (n,n), it is important to consider the scaling of the probability of successfully preparing the cat state, which is given by $\text{pr}(n,n) = \||\langle\chi|\Psi\rangle\|^2 = |\langle\psi|\psi\rangle|^2$. This probability depends on both β and λ since these parameters determine the number of photons after the beam splitter. In fact, there is an optimal choice for λ that maximizes $\text{pr}(n,n)$ given a desired

[2]The optimization algorithms used the function *optimize.minimize* (using the default Broyden–Fletcher–Goldfarb–Shanno method) from the Python package *Scipy*.

cat size $|\beta|^2$. We numerically determine this optimal λ by finding where the derivative of $\mathrm{pr}(n,n)$ with respect to λ vanishes [red dashed line in Fig. 4.4(b)]. We find that $\mathrm{pr}(n,n)$ scales as $\sim |\beta|^{-5/2}$ which sets the fundamental limit on the success rate of our scheme. Such decrease of the success rate with the cat size is a typical feature of post-selected schemes for large cat state preparation [161, 163, 164]. Note the complementarity of our scheme with respect to Ref. [161]: while the latter scheme requires a non-Gaussian photon-number input state and Gaussian homodyne measurement, our scheme requires a Gaussian input state and a non-Gaussian measurement.

4.4.2 Four-component cats

Four-component cats are superpositions of four coherent states evenly distributed in phase-space,

$$|\mu\rangle = \mathcal{N}\left(|\beta\rangle + |-\beta\rangle + (-1)^{\mu}\,|i\beta\rangle + |-i\beta\rangle\right), \tag{4.15}$$

where $\mathcal{N}$ is a normalization factor and $\mu = \{0,1\}$. These provide the logical qubit states in the "cat code" [141, 142], a quantum error correction protocol that protects $|\mu\rangle$ to photon loss. Like two-component cats, four-component cats have also been studied in the context of quantum sensing [165–168] since they can have phase-space features much smaller than Planck's constant [169]. There exist schemes for preparing four-component cat states in the microwave domain with superconducting qubits [144, 145] and in the motional state of a mechanical oscillator [168, 170]. The scheme that we present now is one of the first proposed methods to prepare four-component cats in the optical domain (see also Ref. [171] which appeared roughly at the same time).

Recall that in the preparation of two-component cats, the even-parity detector acted as a symmeterization operation by heralding a state $|\psi\rangle$ which was approximately the control state with its odd photon-number terms eliminated. This motivates concatenating even-parity detectors in order to engineer more complex even-parity states, as shown in Fig. 4.5(a). For example, if we use a displaced two-component cat state as the control for a second even-parity detector, the symmeterization should produce the desired state as in Eq. (4.15).

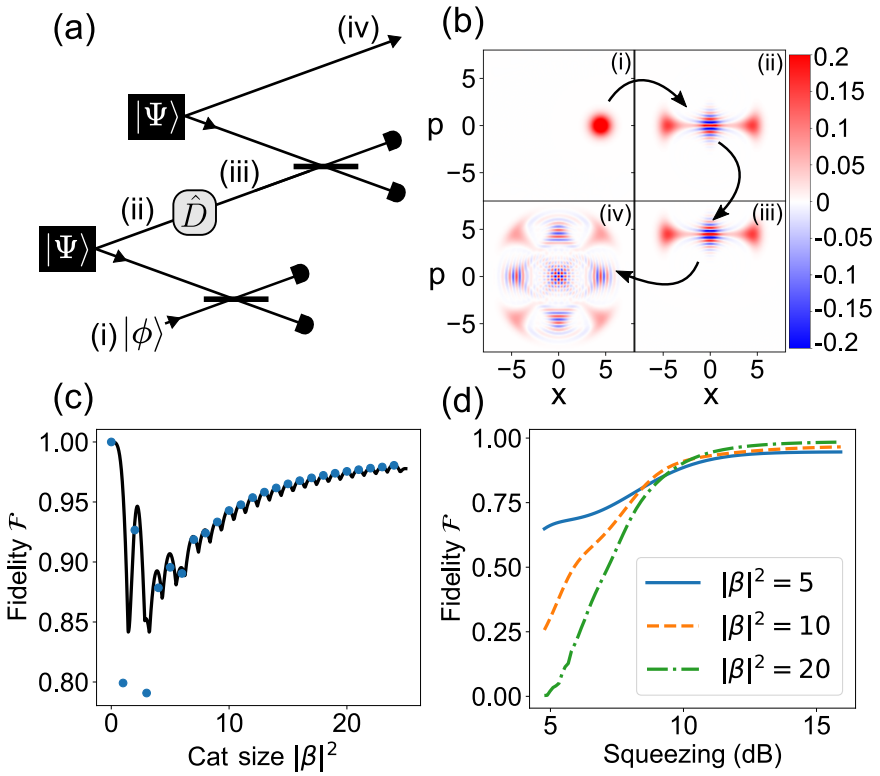

Figure 4.5: **Four-component cat states.** (a) We concatenate two instances of the even-parity detector. Between the two instances, a displacement operation $\hat{D}$ is performed. Using this concatenated scheme, we prepare a four-component cat state. (b) The Wigner functions of the signal state is displayed for different stages of the procedure (here $\beta = \sqrt{10}$). (c) Fidelity $\mathcal{F}$ of the four-component cat state with respect to the ideal state in Eq. (4.17), assuming infinite squeezing, i.e. $\lambda = 1$. The blue circles are obtained by setting $n = |\beta|^2 \in \mathbb{N}$, whereas the line is obtained from a numerical optimization of the post-selected photon numbers at both stages, the amplitude of the initial coherent state and the displacement. In this idealized case, $\mathcal{F} \to$ for increasing cat size. The dip at small cat sizes is caused by the non-flatness of $A_{j,n}$ for small n. (d) Behaviour of the fidelity for finite squeezing, i.e. $\lambda < 1$.

We begin by discussing our scheme assuming infinite squeezing, i.e. $\lambda = 1$. The finite squeezing case will be considered later. The first step is to produce a cat state $|\beta\rangle + |-\beta\rangle$ as described in the previous section. Next, we displace this cat state by β in the direction perpendicular to the axis of the cat, i.e. apply the displacement operator $\hat{D}(i\beta)$:

$$\begin{aligned} |\psi_{\text{iii}}\rangle &= \hat{D}(i\beta)\left(|\beta\rangle + |-\beta\rangle\right) \\ &= e^{i2|\beta|^2}\,|\beta + i\beta\rangle + e^{-i2|\beta|^2}\,|-\beta + i\beta\rangle\,. \end{aligned} \tag{4.16}$$

Finally, by measuring one of the modes of a fresh copy of $|\Psi\rangle$ with a second even-parity detector that uses $|\psi_{\text{iii}}\rangle$ as its control state, we should prepare a symmetrized version of $|\psi_{\text{iii}}\rangle$. Indeed, post-selecting on the outcome $(2n, 2n)$, we prepare an approximate version of the state

$$\begin{aligned} |\psi_{\text{iv}}\rangle &= |\beta - i\beta\rangle + |-\beta + i\beta\rangle \\ &\quad + e^{-i2|\beta|^2}\left(|\beta + i\beta\rangle + |-\beta - i\beta\rangle\right), \end{aligned} \tag{4.17}$$

which is the desired four-component cat state. It should be noted that the phase term $e^{-i2|\beta|^2}$ is determined by the size of the cat and cannot be independently controlled in our scheme. We numerically simulated this procedure and plot the Wigner function of the state at each step in Fig. 4.5(b).

The fidelity of the final state with $|\psi_{\text{iv}}\rangle$ as a function of its size is shown in Fig. 4.5(c). The behaviour is similar to that of the two-component cats studied above. That is, the fidelity asymptotically approaches unity with increasing $|\beta|^2$, but shows a dip for small $|\beta|^2$ due to non-flatness of the Holland-Burnett state coefficients $A_{j,n}$ for small n.

We now consider the case of finite squeezing, i.e. $\lambda < 1$. If we were able to prepare a perfect two-component cat at stage (iii), the effect of finite squeezing on $|\psi_{\text{iv}}\rangle$ could be compensated by appropriately choosing the amplitude and displacement of that cat. However, unlike the first control state, this second control state is imperfect, which prevents the compensation from working properly for the following reason. When $\lambda < 1$, the values of j corresponding to the most significant coefficients of the heralded state's photon-number decomposition [Eq. (4.9)] are shifted with respect to

the center of the control state's photon-number decomposition, towards lower j. In other words, $|\psi_{\text{iv}}\rangle$ is mainly determined by the photon-number coefficients c_{2n-j} in the tail of the distribution of $|\psi_{\text{iii}}\rangle$. While the fidelity of $|\psi_{\text{iii}}\rangle$ is determined by its most significant photon-number coefficients, and increases with its size, the errors in the tail region of the distribution remain roughly constant. As a result, the fidelity of the final state depends on the squeezing parameter, as shown in Fig. 4.5(d). That is, high-fidelity compensation appears to be possible only above a squeezing level of about 12–13 dB, independent of the cat size. Moreover, the detrimental effects of loss and detector inefficiency will be more severe than for the two-component cat [Fig. 4.4(c)] as there are two instances of the even-parity detector.

4.4.3 Other possibilities

One can engineer more complex states by concatenating further instances of even-parity detectors at the cost of a reduced heralding probability with each additional instance. For example, by varying the phase of the displacement between each instance, one can prepare states with different discrete rotational symmetries in phase-space [172] such as hypercube states [168].

Another interesting prospect is going beyond ancillas in coherent states. For example, it is straightforward to show that using a squeezed coherent state ancilla can produce a squeezed cat state. Such states have applications in quantum-enhanced interferometry [173] and are one of the ingredients for preparing Gottesman-Kitaev-Preskill states using the recipe of Ref. [174].

We also investigated preparing Gottesman-Kitaev-Preskill states directly with the even-parity detector using the idea illustrated in Fig. 4.6(c). We studied this idea numerically and found that the scheme up to step 2 works, i.e. we can prepare squeezed cat states. Unfortunately, the photon-number distribution of the displaced squeezed cat is in general asymmetric, i.e. $c_j \neq c_{2n-j}$, where n is the post-selected detection outcome. Because the j^{th} coefficient of the projected $|\chi\rangle$ state is determined by $c^*_{2n-j}A_{n,j}$ [Eq. (4.4)], this asymmetry causes $|\chi\rangle$ not to be a symmeterized version of a displaced squeezed cat, i.e. step 3 fails. This emphasizes the requirement that the

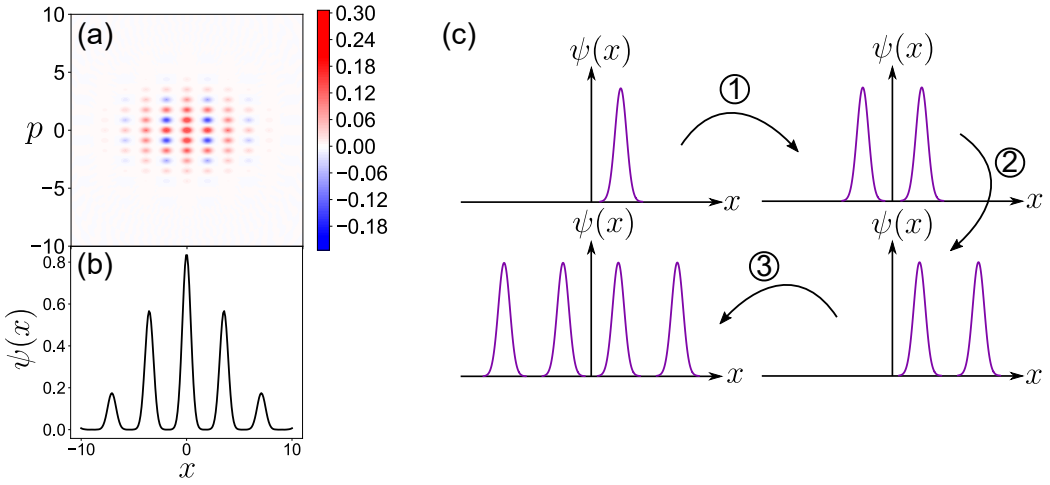

Figure 4.6: **Gottesman-Kitaev-Preskill states.** (a) The Wigner function and (b) wave function of a GKP state with $\Delta = 0.4$ and $k = 0.25$ following Eq. 1 in Ref. [174]. (c) A schematic of the recipe we considered for preparing GKP states. Step ①: Starting with a squeezed coherent state as the initial control state, apply the even-parity filter such that it approximates a symmetrization operation. Step ②: Displace the resulting state to prepare a second control state. Step ③: Using this second control state, apply the even-parity filter such that it approximates a symmetrization operation. By repeating steps 1-3, it should be possible to prepare large GKP states. Unfortunately, our numerics suggest that our even-parity filter fails to act as a symmetrization operation in step ③ due to the photon-number distribution of the second control state.

control state should have a symmetric photon-number distribution about its mean in order for the even-parity detector to implement a symmetrization operation.

Finally, it is worth noting that although our scheme prepares states of even-parity only, one can also use photon subtraction or addition operation to convert these to odd-parity states.

4.5 Experimental realizations

We briefly discuss our scheme in the context of current experimental capabilities. The requirements on the fidelity and size of the cat states ultimately depend on their desired use. For instance, Fig. 4.4(b) suggests that it is possible to prepare a cat state of size $|\beta|^2 = 20$ using transition edge sensors since these can detect up to ~ 20 photons [55]. Assuming a detection efficiency of 98%, such a large cat could be prepared with $\sim 80\%$ fidelity. In contrast, a smaller cat of size $|\beta|^2 = 3$ could be prepared with $\sim 90\%$ fidelity. The detection efficiency would need to be improved

above 99% to reach near-unity fidelities. As a point of reference, a cat state of size $|\beta|^2 = 7$ was prepared with 81% fidelity in a superconducting system [144].

Besides the detectors, another important consideration is the two-mode squeezed vacuum source. Preparing large cats in practice requires significant squeezing to obtain a reasonable heralding rate. At most 15 dB of squeezing is required to achieve the optimal heralding probability for two-component cat state of sizes up to $|\beta|^2 = 50$ [see red curve in Fig. 4.4(a)]. For example, at the 100 kHz experimental repetition rate usually used with transition edge sensors, one could herald a cat state of size $|\beta|^2 = 20$ at a rate of $\sim$ 100 Hz using 13 dB of squeezing. Such high squeezing levels are achievable in a continuous-wave experiment using an optical parametric oscillator [175, 176] and potentially in a pulsed regime using optical waveguides [177, 178]. If instead only e.g. 5 dB of squeezing is available, then one could herald a cat state of size $|\beta|^2 = 5$ at a rate of $\sim$ 1 Hz.

Imperfections such as thermal noise and modal purity of the two-mode squeezed vacuum source would also affect the performance of our scheme. While the former imperfection can be modelled with optical loss [133] [see Fig. 4.4(b)], the latter is more complicated. To minimize its effect, one would need to ensure that $|\Psi\rangle$ occupies a pair of well-defined spatio-temporal modes, one of which is well-matched to that of the control state $|\phi\rangle$.

We note that some the requirements needed to implement this scheme experimentally were achieved in the weak-field homodyne experiment of Chapter 3. In that experiment, the coherent state was produced through difference frequency generation in a KTP waveguide. While that approach was convenient to prepare a local oscillator that is well mode-matched to the two-mode squeezed vacuum source, we could not control the phase between the two lasers driving the difference frequency process. As such, the phase of the coherent state was drifting freely which would be unsuitable for preparing and characterizing the phase-sensitive cat state. A possible solution would be to phase-lock the two lasers driving the difference frequency generation. Alternatively, one can start with a single laser, tap-off some of the light for the local

oscillator, and frequency-double the remaining light to pump the down-conversion process with its second harmonic.

4.6 Conclusions

To summarize, we devised an even-parity detector by exploiting the interference phenomenon that leads to the production of Holland-Burnett states in a time-reversed fashion. The even-parity detector is controlled by varying the photon-number distribution of an ancillary control state. When this ancilla is in a coherent state, we showed that one can prepare two- and four-component Schrödinger cat states of arbitrary size with nearly perfect fidelity. In practice, the size of the cats is limited by the dynamic range of photon-number resolving detectors and the linear optical losses. Since these can detect up to ~ 20 photons with up to 95% efficiency [51], we believe our scheme provides a promising route for preparing larger-scale cats in an experiment.

Chapter 5

Interferometry with quantum states of light

5.1 Introduction

In 1881, Michelson developed an apparatus that could resolve the length difference between two optical paths with a precision of roughly 10^{-8} m [179]. His apparatus [Fig. 5.1(a)] was also used to perform one of the first phase sensing measurements: by sending light from a common source into two optical paths and recombining them, Michelson measured an interference pattern containing information about the relative phase difference between the light traveling in either paths. Michelson and Morely used this technique to test the existence of luminiferous aether which led to one the most well-known null results in physics [180].

In addition to being an indispensable tool for understanding the physical properties of light, optical interferometry has found many applications in tasks requiring

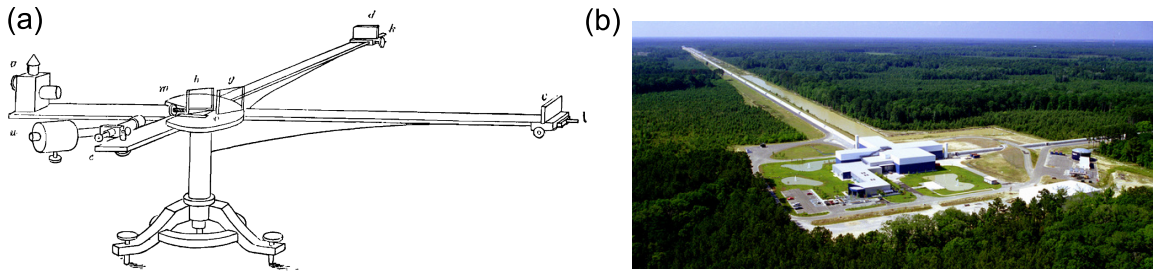

Figure 5.1: **Michelson interferometer.** (a) Michelson's sketch of one of his first interferometer designs taken from Ref. [179]. (b) Aerial photograph of the LIGO detector in Livingston, USA. Credit: Caltech/MIT/LIGO Lab.

sensitive measurements of physical quantities such as length and speed. Remarkably, 135 years after Michelson's experiment, the same interferometric technique is being used by the Laser Interferometer Gravitational-Wave Observatory (LIGO) to resolve length differences as small as 10^{-20} m [Fig. 5.1(b)]. Owing to this phenomenal precision, LIGO detected gravitational waves for the first time in 2016 [181].

There are many technical reasons for LIGO's substantial improvement in precision compared to Michelson's apparatus, such as the stability and quality of the mirrors. But ultimately the precision of an interferometer is limited by the properties of the light source. In particular, the uncertainty $\Delta\phi$ in measuring the phase difference between the two paths of an interferometer is fundamentally limited by quantum noise in light [134]. For light in a classical coherent state, such as from a laser, the phase uncertainty $\Delta\phi$ scales as $\Delta\phi \propto 1/\sqrt{N}$ due to quantum fluctuations in the number of detected photons N. This is known as the shot-noise limit. By using an extremely bright laser and power-recycling cavities, LIGO reaches very large N values to minimize shot noise relative to their signal. However, at such large N, radiation pressure noise causes fluctuations in the mirror position which also limits the precision of the interferometer. In contrast to shot noise, radiation pressure noise becomes worse as N increases. The optimal trade-off between shot noise and radiation pressure noise is known as the standard quantum limit and represents the ultimate precision achievable with laser light due to quantum noise [182].

In 1981, Caves proposed using squeezed vacuum states to surpass the standard quantum limit [134]. These states have reduced quantum fluctuations compared to a coherent state and can improve the maximal signal-to-noise ratio of an interferometer. By injecting squeezed vacuum into the interferometer, LIGO's sensitivity surpasses the standard quantum limit and detects 50% more gravitational wave events as a result of the quantum enhancement [183].

Besides gravitational wave detection, quantum-enhanced interferometery has also been used to characterize photosensitive samples [184–188]. Such systems deteriorate when exposed to light and hence it is desirable to maximize the amount of information extracted about the sample per photon. To this end, in this chapter we study quantum

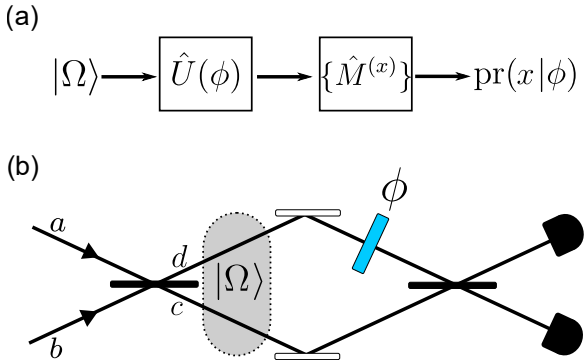

Figure 5.2: **Quantum metrology and interferometry.** (a) Idealized single parameter estimation problem. Further details found in text below. (b) The goal of optical interferometry is to determine the phase difference ϕ between the two arms of the interferometer. Here the measurement strategy consists in recombining the interferometer arms on a beam splitter and performing photon counting in both output modes.

states of light that can surpass the shot-noise limit by exploiting entanglement and nonclassical photon statistics.

5.2 Background

Interferometery can be treated as a single-parameter estimation problem in the framework of quantum metrology. The parameter being estimated is the phase difference between the two paths of the interferometer. In this section, we review some key concepts of quantum metrology including Fisher information. We then briefly review previous works in quantum-enhanced interferometry before proceeding to the proposed scheme and finally our experiment.

5.2.1 Fisher information

The task of single-parameter estimation is shown schematically in Fig. 5.2(a). A quantum state $|\Omega\rangle$, i.e. the "probe", is subject to unitary evolution $\hat{U}(\phi) = e^{i\hat{H}\phi}$ governed by a Hamiltonian $\hat{H}$ which depends on the parameter of interest ϕ. The sensitivity of $|\Omega\rangle$ to the parameter ϕ is determined by the rate at which $|\Omega(\phi)\rangle = \hat{U}(\phi)\,|\Omega\rangle$ becomes distinguishable from $|\Omega\rangle$. This sensitivity can be quantified using

the quantum Fisher information which is given by [189]

$$\begin{aligned}\mathcal{Q} &= 4\left[\langle\partial_\phi\Omega(\phi)|\partial_\phi\Omega(\phi)\rangle - |\langle\partial_\phi\Omega(\phi)|\Omega(\phi)\rangle|^2\right] \\ &= 4\left[\langle\Omega|\hat{H}^2|\Omega\rangle - \langle\Omega|\hat{H}|\Omega\rangle^2\right].\end{aligned} \tag{5.1}$$

where the second line follows from $|\partial_\phi\Omega(\phi)\rangle = \partial_\phi\left(e^{i\hat{H}\phi}|\Omega\rangle\right) = i\hat{H}|\Omega(\phi)\rangle$. A larger $\mathcal{Q}$ indicates greater sensitivity to ϕ.

While $\mathcal{Q}$ quantifies the sensitivity of the probe $|\Omega\rangle$ to ϕ, the precision with which ϕ can be estimated also depends on the measurement used to extract information about ϕ from $|\Omega(\phi)\rangle$. This measurement is in general described by a positive operator value measure $\{\hat{M}^{(x)}\}$ where x labels the measurement outcome. Repeating this measurement on identical copies of $|\Omega(\phi)\rangle$ produces a probability distribution $\mathrm{pr}(x|\phi) = \langle\Omega(\phi)|\hat{M}^{(x)}|\Omega(\phi)\rangle$. The amount of information about ϕ in $\mathrm{pr}(x|\phi)$ can be quantified using the classical Fisher information

$$\begin{aligned}\mathcal{F}(\phi) &= \sum_x \left(\partial_\phi \log\left[\mathrm{pr}(x|\phi)\right]\right)^2 \mathrm{pr}(x|\phi) \\ &= \sum_x \frac{\left[\partial_\phi \mathrm{pr}(x|\phi)\right]^2}{\mathrm{pr}(x|\phi)}\end{aligned} \tag{5.2}$$

where ∂_ϕ denotes the partial derivative with respect to ϕ. Probability distributions having a sharp dependency on ϕ contain more information about ϕ and hence score a higher $\mathcal{F}$. While the quantum Fisher information $\mathcal{Q}$ quantifies the sensitivity of the probe to ϕ independent of the measurement, the classical Fisher information $\mathcal{F}$ quantifies the amount of information about ϕ that is obtained using a particular probe and measurement strategy.

Finally, an estimator such as maximum likelihood is used to determine the value of ϕ from $\mathrm{pr}(x|\phi)$. The standard deviation $\Delta\phi$ of this estimator is bounded by [189]

$$\Delta\phi \geq 1/\sqrt{\mathcal{F}} \geq 1/\sqrt{\mathcal{Q}}. \tag{5.3}$$

The first (second) inequality is known as the (quantum) Cramer-Rao bound. Note that $\mathcal{Q} = \mathcal{F}$ is achieved when the optimal measurement strategy for a given probe is used. Furthermore, the bounds are saturated when the optimal estimator is chosen.

In the asymptotic limit of infinite measurement trials, maximum likelihood can always saturate the Cramer-Rao bound [190].

We now apply this general framework to the practical scenario shown in Fig. 5.2(b). The task is to estimate the phase difference between the two arms of the Mach-Zender interferometer. We consider probes with path symmetry, i.e. $|\Omega_{cd}\rangle = |\Omega_{dc}\rangle$, which encompasses a broad class of probes, including those prepared by injecting combinations of squeezed vacuum, coherent, or photon-number states into the interferometer [191]. The Hamiltonian generating a relative phase shift ϕ between the two arms of the interferometer is given by[1]

$$\hat{H} = \left(\hat{c}^\dagger \hat{c} - \hat{d}^\dagger \hat{d}\right)/2. \tag{5.4}$$

Our measurement consists in recombining the interferometer arms on a beam splitter and performing photon counting in both output modes. In the absence of loss, this measurement is optimal for path-symmetric probes, i.e. $\mathcal{Q} = \mathcal{F}$ [191].

Inserting the Hamiltonian of Eq. (5.4) into Eq. (5.1), we find a more suggestive form for the quantum Fisher information of Ω:

$$\mathcal{Q} = 2\left(\mathrm{Var}(\Omega) - \mathrm{Cov}(\Omega)\right) \tag{5.5}$$

with

$$\begin{aligned} \mathrm{Var}(\Omega) &= \langle(\hat{c}^\dagger \hat{c})^2\rangle - \langle \hat{c}^\dagger \hat{c}\rangle^2 = \langle(\hat{d}^\dagger \hat{d})^2\rangle - \langle \hat{d}^\dagger \hat{d}\rangle^2 \\ \mathrm{Cov}(\Omega) &= \langle \hat{c}^\dagger \hat{c} \hat{d}^\dagger \hat{d}\rangle - \langle \hat{c}^\dagger \hat{c}\rangle \langle \hat{d}^\dagger \hat{d}\rangle . \end{aligned} \tag{5.6}$$

Eq. (5.5) highlights the role of two different types of quantum correlations in Ω, namely intramode and intermode correlations [173]. Intramode correlations, quantified by $\mathrm{Var}(\Omega)$, are enhanced by probes exhibiting super-Poissonian statistics, $\mathrm{Var}(\Omega) > N$, such as squeezed vacuum. Intermode correlations, quantified by $\mathrm{Cov}(\Omega)$, are enhanced by path-entanglement such as with N00N states $(|N,0\rangle + |0,N\rangle)/\sqrt{2}$. For such path-entangled states, $\mathrm{Cov}(\Omega) < 0$ which increases $\mathcal{Q}$ and hence increases the phase sensitivity of the probe.

[1]Note that using $\hat{H} = \hat{c}^\dagger \hat{c}$ can lead to an extra factor of 2 in $\mathcal{Q}$ due to a subtle issue having to do with phase references [192]. To avoid this issue, we consider the relative phase shift between the two arms of the interferometer, i.e. $\phi \equiv \phi_c - \phi_d$.

Name	$\|\Omega\rangle$	$\mathcal{Q}(\eta_s = 1)$	$\mathcal{Q}(\eta_s)/N$	Definite photon number?
Classical	$\hat{U}_{\text{BS}} \|\alpha, 0\rangle$	$\|\alpha\|^2$	η_s	✗
Caves [194]	$\hat{U}_{\text{BS}} \|\alpha, \zeta\rangle$	$\|\alpha\|^2 e^{2\zeta} + \sinh^2 \zeta$	$e^{2\|\zeta\|^2}$[2] $(\eta_s = 1)$ [195]	✗
Holland-Burnett [136]	$\hat{U}_{\text{BS}} \|n, n\rangle$	$2n^2 + 2n$	$(N/2+1)\eta_s^{N/2+1}$ [196]	✓
N00N [197]	$\|n, 0\rangle + \|0, n\rangle$	n^2	$N\eta_s^N$ [196]	✓
Squeezed vacuum [198]	$\|\zeta, \zeta\rangle$	$\sinh^4 \zeta + 2\sinh^2 \zeta$	$\frac{(N+2)\eta_s^2}{\eta_s + N(1-\eta_s)\eta_s^2}$ [199]	✗

Table 5.1: A selection of probes $|\Omega\rangle$ that have been proposed for quantum-enhanced interferometry. $|\Omega\rangle$ labels the state inside the interferometer and is not necessarily normalized. $\mathcal{Q}(\eta_s)/N$ is the quantum Fisher information per photon as a function of the efficiency η_s of the interferometer which is assumed to be equal in both modes. $\hat{U}_{\text{BS}}$ is a balanced beam splitter transformation, N is the total average photon number before losses, $|\alpha\rangle$ is a coherent state, $|n\rangle$ is a Fock state, and $|\zeta\rangle$ is a squeezed vacuum state.

In Table 5.1, we list some proposed probes and their quantum Fisher information. These either have definite photon number or indefinite photon number. In both cases, the ultimate scaling in sensitivity is determined by the Heisenberg limit $\Delta\phi \propto N^{-1}$ or equivalently $\mathcal{Q}/N \propto N$. This limit is determined by the linear dependence of Eq. (5.4) on photon number [193].

5.2.2 Decoherence

An important issue which has not yet been addressed is decoherence. The main source of decoherence in optical interferometry is loss, which can play a detrimental role in all three stages of an interferometry experiment, namely (i) in the preparation of the probe, (ii) inside the interferometer (e.g. absorption in a sample), (iii) in the measurement [200]. It is also possible for the input probe to occupy more than one spatiotemporal mode. Such sources of decoherence are treated by extending the quantum Fisher information formalism to mixed states and general quantum channels [201]. The sensitivity of probe after decoherence will always be less than that of the ideal probe due to the convexity of $\mathcal{Q}$. Moreover, photon counting is

[2]This holds when $|\alpha|^2 \gg \sinh^2 \zeta$, i.e. there are many more photons in the coherent state than in the squeezed vacuum, which is the regime in which LIGO operates.

generally no longer the optimal measurement strategy in the presence of decoherence.

Certain probes are more susceptible to loss than others. In Table 5.1, we list $\mathcal{Q}(\eta_s)/N$ where η_s is the efficiency of the interferometer which is assumed to be equal in both arms and N is the total average photon number before losses. Although the N00N state is the optimal definite photon-number state in the absence of loss, the Holland-Burnett state has better sensitivity in the regime of loss obtainable in most experiments [200]. This is because the loss of a single photon is sufficient to collapse the N00N state superposition to a phase-insensitive mixture.

5.2.3 Optimality

Largely speaking, quantum-enhanced interferometry is motivated by applications that fall into one of two different regimes. The first is the high photon flux regime where the goal is to maximize the absolute precision of an interferometer, as in gravitational wave detectors. In this first regime, the Caves probe and homodyne detection was shown to be optimal strategy [202], even in the presence of loss [203]. The second is a low photon flux regime where the goal is to maximize phase sensitivity per photon inside the interferometer, which is the regime of interest in this thesis. This regime is useful for characterizing delicate photosensitive samples, in which case the relevant resource is the number of times a photon interacts with the sample [184–188]. In this case, one metric to consider is the quantum Fisher information divided by the average number of photons inside the interferometer, $\mathcal{Q}/N$.

Finding the probe with the optimal $\mathcal{Q}/N$ in the low flux regime is a thorny problem. In the absence of loss, the optimal definite photon-number states are the N00N states. With loss, the optimal definite photon-number states were studied in Ref. [204] and experimentally demonstrated in Ref. [205] for $N = 2$. The probes which we propose and experimentally prepare later in the chapter approximate these optimal states. While the optimal Gaussian state is squeezed vacuum [198], the optimal non-Gaussian state is not known, even in the absence of loss. One notable example of such a state is the squeezed Schrödinger cat which has been shown to be more phase-sensitive than both squeezed vacuum and N00N states [173].

5.2.4 Previous experiments

In the high photon flux regime, squeezed vacuum is currently being injected into gravitational wave detectors to improve their sensitivity beyond the standard quantum limit, see e.g. Ref. [183].

Many experiments in the low photon flux regime focused on preparing N00N states. Initial works focused on demonstrating "super-resolution" fringes which oscillate N times faster than classical fringes due to the path-entanglement of the probe. Up to $N = 5$ N00N states and super-resolution fringes have been experimentally demonstrated [206–211]. These demonstrations employed post-selection to prepare and detect the N00N states, i.e. they only measured a subset of the photons that were inside the interferometer. However, for many practical applications the relevant resource is the number of photons inside the interferometer, in which case it is important to also account for undetected photons [212, 213]. By avoiding post-selection and employing high efficiency detectors, Ref. [214] achieved an improvement of 14% to the shot-noise limit using a $N = 2$ N00N state while accounting for all photons. Besides N00N states, a number of works also studied more loss-tolerant probes [205, 215] such as Holland-Burnett states [200, 213, 216–219], though these works had insufficient detection efficiency to unconditionally surpass the shot-noise limit. With indefinite photon-number probes, a 15% unconditional improvement was achieved in a continuous-wave regime using squeezed vacuum and homodyne detection [220, 221].

Scaling to larger quantum states would enable greater enhancements in sensitivity, but this requires (i) probe states that are tolerant to realistic levels of loss, (ii) sources that can generate these probes at a reasonable rate, and (iii) detectors that can efficiently resolve higher photon numbers. In the next section, we present a scheme that addresses these challenges using a novel definite photon-number probe.

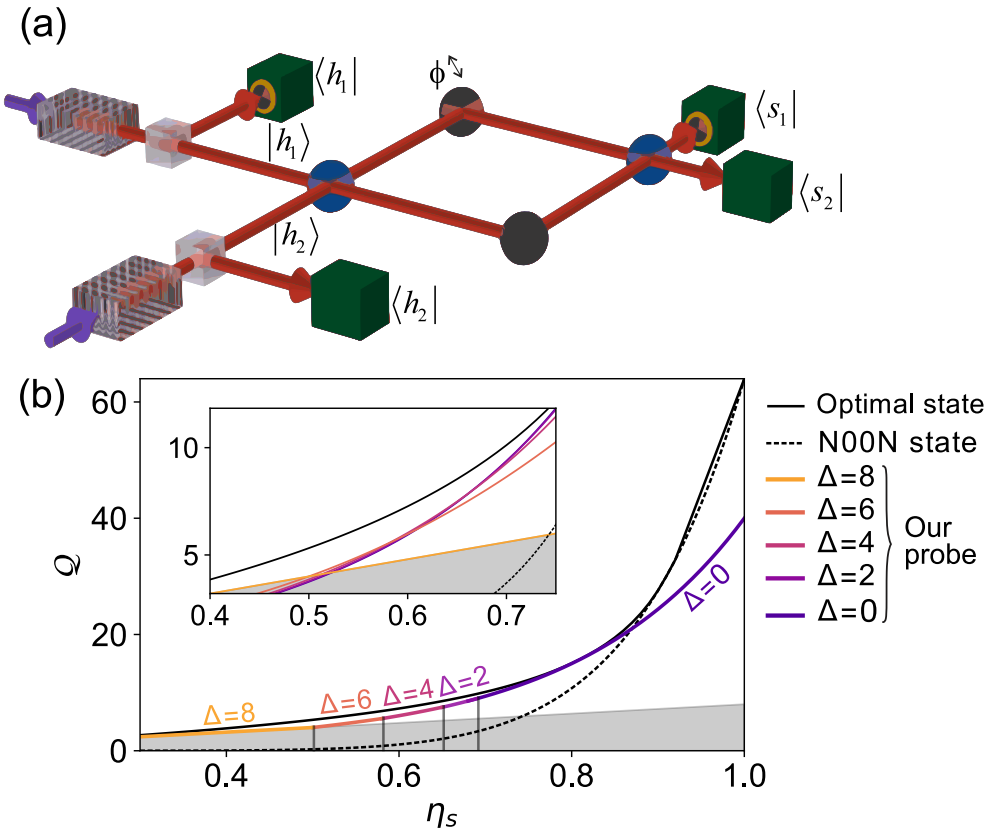

Figure 5.3: **Interferometric scheme**. (a) Two type-II parametric down-conversion sources each produce orthogonally-polarized pairs of beams that are separated using polarizing beam splitters. By measuring one of the beams of each source with an ideal photon-number-resolving detector, we herald a pair of photon-number states $|h_1, h_2\rangle$. We inject this probe into an interferometer and perform photon counting at the output to estimate the unknown phase difference ϕ. (b) Quantum Fisher information $\mathcal{Q}$ calculated for 8-photon ($N = h_1 + h_2 = 8$) probes inside the interferometer as a function of the signal transmissivity η_s which is assumed to be equal in both interferometer modes. Coloured curve in the main figure plots $\mathcal{Q}$ of the probe with the optimal $\Delta = |h_1 - h_2|$ for a given η_s, while the inset show the full curves of each probe for $\eta_s \in [0.4, 0.75]$. Our probe approximates the performance of the optimal state [black line] and surpasses that of the N00N state [dashed line] for efficiencies below $\sim 90\%$. The grey filled region indicates performance below the shot-noise limit.

5.3 Interferometry with photon-number states

The idea is illustrated in Fig. 5.3(a). Two type-II SPDC sources each produce a two-mode squeezed vacuum state:

$$|\Psi\rangle = \sqrt{1-\lambda^2}\sum_{n=0}^{\infty}\lambda^n\,|n,n\rangle\,. \tag{5.7}$$

where λ is a parameter that determines the average number of photons in each beam, $\langle n\rangle = \lambda^2/(1-\lambda^2)$. Measuring one of the beams with an ideal lossless photon-number-resolving detector projects the second beam to a known photon-number state $|h_1\rangle$. Duplicating this procedure with a second independent source and detector, we herald pairs of photon-number states that are not necessarily equal, $|h_1, h_2\rangle$. When these states are combined on the first beam splitter, multiphoton interference generates a path-entangled probe inside the interferometer [146, 222].

We quantify the phase-sensitivity of the probe inside the interferometer by calculating the quantum Fisher information $\mathcal{Q}$. In Appendix D, we show that in the absence of loss, $\mathcal{Q} = 2h_1h_2 + h_1 + h_2$, which exhibits Heisenberg scaling ($\mathcal{Q} \sim N^2$) and generalizes the case of Holland-Burnett states ($h_1 = h_2$). We also numerically study the robustness of our probe to losses. In Fig. 5.3(b), we plot $\mathcal{Q}$ of 8-photon probes ($N = h_1 + h_2 = 8$) having different $\Delta = |h_1 - h_2|$ as a function of the signal transmissivity η_s (assumed to be equal in both interferometer modes). Probes with a small Δ provide a greater advantage over the shot-noise limit but are more sensitive to losses. Since the probe is heralded in our scheme, one can choose the optimal Δ for a given η_s.

Also shown in Fig. 5.3(b) is $\mathcal{Q}$ for the optimal state that maximizes $\mathcal{Q}$ for a given N and η_s [204]. For the loss-free case ($\eta_s = 1$), the optimal state is the N00N state. However, for efficiencies below $\sim 90\%$, our probes significantly surpass the N00N state in terms of $\mathcal{Q}$, exhibiting performance close to optimal. Moreover, in contrast to the N00N and Holland-Burnett states, the probe with $\Delta = N$ performs at least as well as the shot-noise limit for any amount of loss.

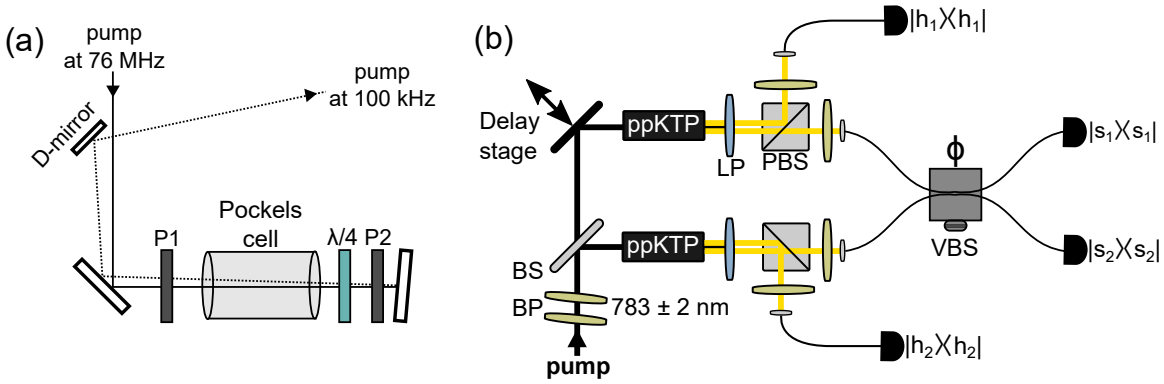

Figure 5.4: **Experimental setup.** (a) Pulse picker for pump. P1/P2: Glan-Thompson polarizers, $\lambda/4$: quarter-wave plate. (b) A schematic of the experimental setup. BS: beam splitter, BP: bandpass filter, ppKTP: periodically-poled potassium titanyl phosphate (waveguide), LP: longpass filter, PBS: polarizing beam splitter, VBS: variable beam splitter.

5.3.1 Experimental setup

In contrast to the experiment in Chapter 3, the pump laser is a titanium sapphire oscillator without the regenerative amplifier[3]. The oscillator produces 150 fs pulses at a 76 MHz repetition rate which is too fast for the TESs. We use a Pockels-cell-based pulse picker to reduce its repetition rate to 100 kHz, as shown in Fig. 5.4(a). The Pockels cell uses a 4 mm long RTP crystal and is driven by a high-voltage switch. The pulse picker consists of the Pockels cell between a pair of cross-polarized Glan-Thompson polarizers. Every 10 μs, a $\sim$ 2 kV voltage is applied across the RTP crystal for 5 ns which modifies its retardance through the nonlinear electro-optic effect and rotates the polarization of the incident pump pulse, ideally by $\pi/2$. A quarter-wave plate is necessary to compensate the natural birefringence of the RTP crystal. Given that we only want one in every 760 pump pulses, the pulse picker requires a large extinction ratio. We use high-quality polarization optics and double-passed the pump through the pulse picker to obtain an extinction ratio of 50 dB and a signal-to-noise ratio of $\sim$ 130. The total transmission of the pulse picker is 72%.

The 100 kHz pulse train is filtered with a pair of angle-tuned bandpass filters (783 $\pm$ 2 nm) and split into two paths that are matched in length using a translation stage.

[3]This is because we replaced the oscillator used in the experiment of Chapter 3 with a new one which was not compatible with the regenerative amplifier.

In each path, we pump a ppKTP waveguide. At the exit of the waveguide, the pump light is rejected with a longpass filter and the orthogonally-polarized down-converted modes are separated using a polarizing beam splitter. Each down-converted mode is filtered with a bandpass filter whose bandwidth is chosen to transmit the main feature of the down-converted spectrum but reject its side-lobes. The herald modes (1566 ± 7 nm) are coupled into single-mode fibers and sent directly to the detectors. All four detectors are transition edge sensors. The signal modes (1567 ± 7 nm) are coupled into polarization-maintaining single-mode fibers and sent into the interferometer. The spectra of the sources are shown in Fig. 2.8(c)-(e).

The interferometer is a fiber-based variable beam splitter (Newport F-CPL-1550-P-FP). This device coherently distributes light from two input fibers into two output fibers according to some splitting ratio and thus implements the same transformation as an interferometer with a fixed phase difference [223]. The splitting ratio can be adjusted by controlling the distance between two evanescently-coupled fibers using a micrometer. The mapping between the splitting ratio and interferometer phase is made explicit below.

5.3.2 Results

We measure $\mathrm{pr}_{s_1,s_2,h_1,h_2}(\phi)$, the joint photon-number probability per pump pulse to obtain the herald outcome (h_1, h_2) and measure (s_1, s_2) at the output of the interferometer when the phase difference is ϕ. We will refer to this as the (s_1, s_2, h_1, h_2) rate.

During data acquisition, we scan the distance x between the two evanescently-coupled fibers. To display our data as a function of the interferometer phase, we first calculate the transmission coefficient $T(x)$ of the variable beam splitter using the measured $(s_1, s_2, h_1, h_2) = (1, 0, 1, 0)$ and $(0, 1, 1, 0)$ rates:

$$T(x) = \frac{\mathrm{pr}_{1,0,1,0}(x)}{\mathrm{pr}_{1,0,1,0}(x) + \mathrm{pr}_{0,1,1,0}(x)}. \tag{5.8}$$

At low powers, we find that the quantity $T(x)$ typically varies within $[0.02, 0.98]$. To

obtain the corresponding phase, we correct for the imperfect visibility:

$$T_{\text{corr}}(x) = \frac{T(x) - \min\left[T(x)\right]}{\max\left[T(x)\right] - \min\left[T(x)\right]} \tag{5.9}$$

such that $T_{\text{corr}}(x)$ varies between [0,1]. For a single photon injected into a Mach-Zender type interferometer with phase difference ϕ between its two arms, one expects $T_{\text{corr}}(x) = [1 - \cos(\phi)]/2$. Solving for ϕ, we find:

$$\phi(x) = \arccos\left(2T_{\text{corr}}(x) - 1\right). \tag{5.10}$$

To quantify the phase sensitivity of the rates measured with a particular herald outcome (h_1, h_2), we calculate the Fisher information [Eq. (5.2)]:

$$\mathcal{F}_{h_1,h_2}(\phi) = \sum_{s_1,s_2} \frac{\left[\partial_\phi \tilde{\text{pr}}_{s_1,s_2,h_1,h_2}(\phi)\right]^2}{\tilde{\text{pr}}_{s_1,s_2,h_1,h_2}(\phi)}, \tag{5.11}$$

where $\tilde{\text{pr}}_{s_1,s_2,h_1,h_2}(\phi)$ is a model fitted to the measured rates (see Appendix C). Our primary figure of merit is the Fisher information per detected signal photon conditioned on measuring (h_1, h_2) at the heralding detectors,

$$\tilde{\mathcal{F}}_{h_1,h_2}(\phi) = \mathcal{F}_{h_1,h_2}(\phi) / \langle \tilde{n} \rangle ,$$

where

$$\langle \tilde{n} \rangle = \sum_{s_1,s_2} (s_1 + s_2) \tilde{\text{pr}}_{s_1,s_2,h_1,h_2}(\phi) \tag{5.12}$$

is the total number of detected signal photons. Injecting a coherent state into our interferometer would in principle yield the Fisher information $\mathcal{F} = \langle \tilde{n} \rangle$ when the detected mean photon is $\langle \tilde{n} \rangle$ [200]. Thus, our figure of merit can be easily compared to the shot-noise limit which corresponds to $\tilde{\mathcal{F}}_{h_1,h_2}(\phi) = 1$.

We measured the total efficiency of the heralding and signal modes to be between $47 - 55\%$ using the method outline in Sec. 2.3.3. This includes $\sim 60\%$ mode coupling efficiency into fibers, 90% interferometer transmission, and $\gtrsim 95\%$ detector efficiency. Due to the latter two losses, the detected $\langle \tilde{n} \rangle$ is 10-15% smaller than the mean photon number inside the interferometer. As such, the Fisher information per photon inside

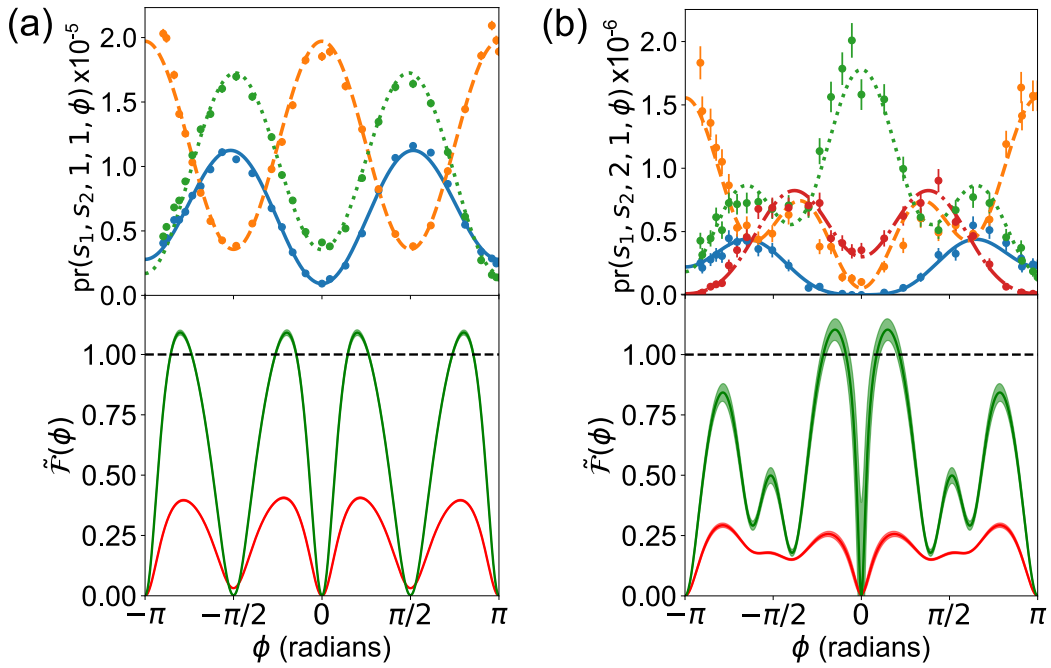

Figure 5.5: **The weak gain regime**. (a) Rates measured with the probe $|1,1\rangle$: $(s_1, s_2, h_1, h_2) = (2,0,1,1)$ [blue], $(1,1,1,1)$ [orange], $(0,2,1,1)$ [green]. (b) Rates measured with the probe $|2,1\rangle$: $(3,0,2,1)$ [blue], $(2,1,2,1)$ [orange], $(1,2,2,1)$ [green], $(0,3,2,1)$ [red]. Error bars are one standard deviation assuming Poissonian counting statistics. Lines are a fitted model $\tilde{\mathrm{pr}}(\phi)$. Bottom panels show the normalized Fisher information $\tilde{\mathcal{F}}(\phi)$ calculated using two methods: (i) post-selecting on events where $s_1 + s_2 = h_1 + h_2$ [green] and (ii) using all events [red]. Line thicknesses show 1σ confidence intervals obtained by fitting 50 simulated data sets that are calculated with a Monte Carlo method. The dashed black line indicates the shot-noise limit.

the interferometer (which is the relevant resource when e.g. probing a delicate sample) is about 10-15% smaller than $\tilde{\mathcal{F}}_{h_1,h_2}(\phi)$.

We begin with low pump power to test our setup in the weak gain regime ($\lambda \sim 0.25$, 10 μW per source). In Fig. 5.5, we show results for two different probes, (a) $|1,1\rangle$, the well-studied $N = 2$ N00N or Holland-Burnett state, and (b) $|2,1\rangle$, a probe studied here for the first time. We calculate $\tilde{\mathcal{F}}(\phi)$ using two methods. In the first, we discard events in which we know photons were lost by only including rates where $s_1 + s_2 = h_1 + h_2$ in the sums of Eqs. (5.11) and (5.12). These rates are shown in the top panels of Fig. 5.5. Using this first method, $\tilde{\mathcal{F}}(\phi)$ [green curves] surpasses the shot-noise limit by 0.09 ± 0.01 for $|1,1\rangle$ and 0.10 ± 0.04 for $|2,1\rangle$ at its highest point. In the second method, we include all measured events. Note that this may include events where $s_1 + s_2 < h_1 + h_2$ due to loss in the signal modes, but also $s_1 + s_2 > h_1 + h_2$ due to loss in the herald modes. Conditioned on obtaining the herald outcome (h_1, h_2), the probability of the latter occurring can be minimized by reducing the pump power and hence λ. This increases the purity of the probe at the cost of reducing its heralding rate. Without post-selection, $\tilde{\mathcal{F}}(\phi)$ [red curves] drops below the shot-noise limit mainly due to losses.

In addition to loss, the spectral purity and distinguishability of our photons are also sources of decoherence that reduce the contrast of the fringes and hence diminish $\tilde{\mathcal{F}}(\phi)$. Consider the probe $|1,1\rangle$, for example. For $\phi = \pm\pi/2$, the whole interferometer acts as a balanced beam splitter in which case Hong-Ou-Mandel interference should lead to a complete suppression in coincidences at its output. However, as can be seen in the orange $(1,1,1,1)$ fit in Fig. 5.5(a), the visibility of this interference effect is $\sim 75\%$. In addition to spectral mismatch between the signal modes, the visibility is degraded by uncorrelated background photons ($\sim 5\%$ of detected photons) and the slight multi-mode nature of our sources, both of which reduce the purity of our heralded photons. The finite detector energy resolution also plays a small role as the detectors have a $\sim 1\%$ chance to mislabel an event by ± 1 photon [55].

Next, we increase the pump power to reach a high-gain regime ($\lambda \sim 0.75$, 135 μW per source) in which we can herald large photon numbers. We detect 16-photon events

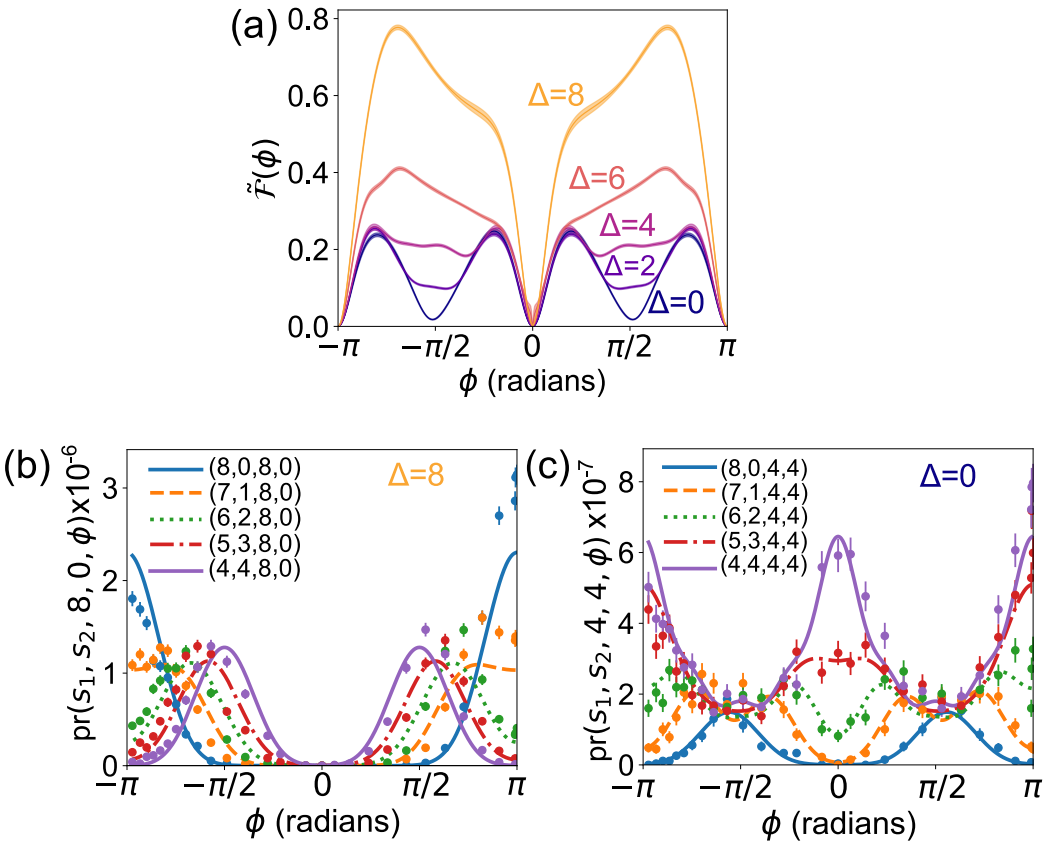

Figure 5.6: **The high gain regime**. (a) $\tilde{\mathcal{F}}(\phi)$ of 8-photon probes ($N = 8$) parameterized by $\Delta = |h_1 - h_2|$. Curves are calculated using Eqs. (5.11) and (5.12) without post-selection. Probes with a larger Δ have a larger $\tilde{\mathcal{F}}(\phi)$ and hence greater phase sensitivity due to their increased robustness to loss. Line thicknesses show 1σ confidence intervals obtained by fitting 50 simulated data sets that are calculated with a Monte Carlo method. (b) and (c) show a subset of rates for the probe with $\Delta = 8$ and $\Delta = 0$, respectively. The lines are a fitted model $\tilde{\text{pr}}(\phi)$. Error bars are one standard deviation assuming Poissonian counting statistics.

at a rate of roughly 7 Hz, which is much higher than the state-of-the-art achievable with bulk crystal SPDC sources [224] or quantum dots [225]. In Fig. 5.6(a), we plot $\tilde{\mathcal{F}}(\phi)$ calculated without post-selection for all probes with $N = 8$. As expected given the regime of loss in our experiment, probes with larger Δ are more phase sensitive due to their increased robustness to loss. In particular, the sensitivity of the $\Delta = N$ probe should be shot-noise limited regardless of losses. This is because with the $\Delta = N$ probe, all photons injected into the interferometer should originate from one source. As such, imperfections such as spectral purity and mode matching do not affect the performance of the probe. However, in practice, the herald detection of 0 photons could occur due to photon loss in the corresponding herald mode. This results in the contamination of the signal with photons from the second source and degrades the performance of the $\Delta = 8$ probe [yellow curve in Fig. 5.6(a)]. This issue is easily circumvented by blocking one of the sources, in which case shot-noise limited performance is recovered. In Fig. 5.7(a), we plot $\tilde{\mathcal{F}}(\phi)$ for the $\Delta = N = 5$ probe calculated without post-selection. We performed the measurement with a single source blocked and with both sources unblockled. In the latter case, we find that $\tilde{\mathcal{F}}(\phi)$ reaches 0.991 ± 0.001 at its highest point, demonstrating shot-noise limited performance. Note that the shot-noise limit is determined by the total number of detected photons, i.e. we did not account for the $< 10\%$ interferometer and detector losses.

5.3.3 Discussion

The fringes produced by our probes exhibit a number of different features compared to those measured with N00N or Holland-Burnett states. For example, with these two states, the expected signature of N-photon interference are fringe oscillations that vary as $\cos(N\phi)$. While our measured fringes do not exhibit such oscillations in the high gain regime, they do exhibit sharper features than classical fringes. We show this explicitly by comparing our rates to those measured with distinguishable photons. This is achieved by temporally delaying photons coming from the top source with respect to photons coming from the bottom source by more than their coherence

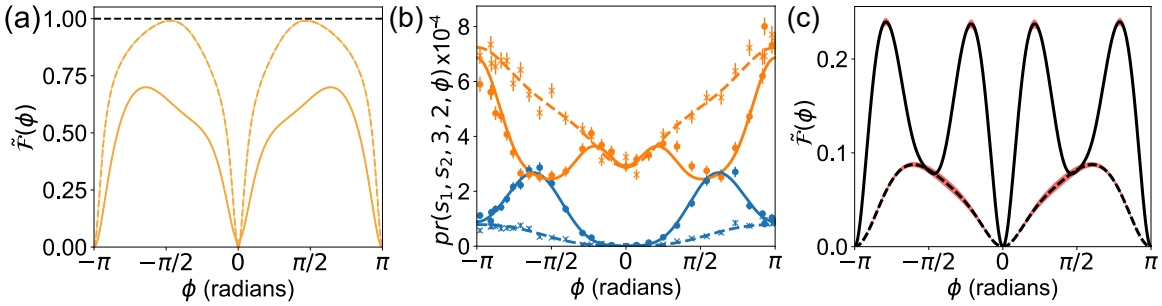

Figure 5.7: **Additional data.** (a) We calculate $\tilde{\mathcal{F}}(\phi)$ using rates measured with the $\Delta = N = 5$ probe without post-selection. Bold line shows result with both sources unblocked, whereas dashed line is result with one of the sources blocked. Line thicknesses show 1σ confidence intervals obtained by fitting 50 simulated experiments. Dashed black line is the shot-noise limit. (b) Two sets of rates [blue: $(5, 0, 3, 2)$, orange: $(3, 2, 3, 2)$] measured when the photons are injected inside the interferometer at the same time (data: circles, theory: bold lines) or at different times (data: crosses, theory: dashed line). In the latter case, the photons are well modelled by classical distinguishable particles. Error bars are one standard deviation assuming Poissonian counting statistics. (c) $\tilde{\mathcal{F}}(\phi)$ shows a significant improvement in sensitivity in the former case (bold line) compared to the latter case (dashed line), demonstrating that multiphoton improved the sensitivity of our probe. Red shaded how 1σ confidence intervals obtained by fitting 50 simulated data sets that are calculated with a Monte Carlo method.

time. As an example, we consider the probe $|3, 2\rangle$ in Fig. 5.7(b). When the photons are injected inside the interferometer at the same time, the fringe contrast is significantly higher than when they are temporally delayed [Fig. 5.7(b)]. Likewise, when we calculate $\tilde{\mathcal{F}}_{3,2}(\phi)$ without post-selection, we find an improvement in the probe's sensitivity in the former case [Fig. 5.7(c)]. This demonstrates that the probe sensitivity derives from multiphoton interference even at high photon numbers.

With any finite amount of loss, $\tilde{\mathcal{F}}_{h_1,h_2}(\phi)$ vanishes when all fringes share a common turning point such as at $\phi = 0$. In the case of Holland-Burnett ($\Delta = 0$) and N00N states, there are also common turning points at $\phi = \pm\pi/2$ which causes the reduction in $\tilde{\mathcal{F}}_{h_1,h_2}(\phi)$ around these phase values [Fig. 5.6(c)]. In contrast, the probes with $\Delta = 4, 6, 8$ do not have a dip in $\tilde{\mathcal{F}}_{h_1,h_2}(\pm\pi/2)$. The origin of this effect for $\Delta = 8$ can be seen directly in the rates shown in Fig. 5.6(b). The region of the fringe with high sensitivity to ϕ (i.e. large gradient) is different for different values of $|s_1 - s_2|$. This feature of $\tilde{\mathcal{F}}_{h_1,h_2}(\phi)$ allows the estimation of ϕ without prior knowledge of the range in which it lies, as is required for N00N or Holland-Burnett states, and thus provides

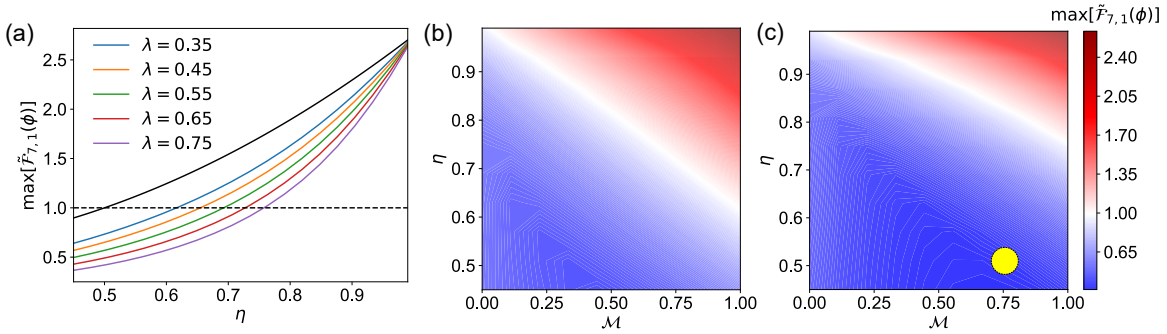

Figure 5.8: (a) Effect of squeezing strength on imperfect heralding. We plot $\max[\tilde{\mathcal{F}}_{7,1}(\phi)]$ as a function of the efficiency η (equal in all four modes) for various SPDC gain parameters λ and assuming $\mathcal{M} = 1$. Black line shows the perfect heralding case ($\eta_{h_1} = \eta_{h_2} = 1$). Dashed line shows the shot-noise limit. (b) and (c) plots $\max[\tilde{\mathcal{F}}_{7,1}(\phi)]$ as a function of η and $\mathcal{M}$ for $\lambda = 0.35$ and $\lambda = 0.75$, respectively. Blue (red) indicates a parameter regime where expected performance is below (above) the shot-noise limit. The yellow circle in (c) shows roughly the parameter regime achieved in the experiment.

a means for global phase estimation without using an adaptive protocol [217, 226].

5.3.4 Improvements required to surpass shot-noise limit without post-selection

Since our probes have $\tilde{\mathcal{F}}_{h_1,h_2}(\phi) < 1$ without post-selecting, our results do not unconditionally surpass the shot-noise limit. We employ the model developed in Appendix C to estimate the required improvements in order to achieve an advantage to the shot-noise limit using our $N = 8$ probes. In particular, we focus on $\Delta = 6$ [i.e. $(h_1, h_2) = (7, 1)$] as this is the most loss-tolerant probe that can surpass the shot-noise limit in our scheme [4]. For simplicity, we assume equal efficiency η in all four modes of the experiment and equal SPDC gain parameters λ. There are three main experimental parameters to consider: (i) the efficiency η, (ii) the distinguishability $\mathcal{M}$ of photons between the top and bottom sources, (iii) the SPDC gain λ. Given these parameters, we estimate the sensitivity of the probe by calculating $\tilde{\mathcal{F}}_{7,1}(\phi)$. Since this quantity generally depends on ϕ, we focus on region in phase with the largest possible sensitivity, i.e. $\max[\tilde{\mathcal{F}}_{7,1}(\phi)]$.

[4] In practice one could ensure that this is the only probe injected into the interferometer by placing a shutter in each signal mode. The shutters can be programmed to open and unblock the beams only when the herald outcome is $\Delta = 6$.

We first focus on the effect of the SPDC gain λ and assume $\mathcal{M} = 1$ for now. As shown in Fig. 5.8(a), a smaller λ provides a larger $\max[\tilde{\mathcal{F}}_{7,1}(\phi)]$. This is because lowering λ increases the photon-number purity of the heralded probe in the presence of loss in the heralding arms, i.e. it reduces the probability that the herald detectors under-counted the true number of photon pairs produced by the sources. As a reference, we include the perfect heralding case which is shown by the black line. While reducing λ minimizes the detrimental effects of imperfect heralding, it also drastically decreases the heralding rate. For example, assuming $\eta = 0.5$ and a 100 kHz laser repetition rate, $\lambda = 0.75$ would produce a $N = 8$ probe roughly once per second whereas $\lambda = 0.35$ would produce such a probe only about once per day. Thus, reducing λ is likely not a practical method to improve $\max[\tilde{\mathcal{F}}_{7,1}(\phi)]$, which places a stringent requirement on the efficiency needed to surpass the shot-noise limit.

Next we consider the combined effect of imperfect distinguishability and efficiency. In Fig. 5.8(b) [(c)], we plot $\max[\tilde{\mathcal{F}}_{7,1}(\phi)]$ as a function of η and $\mathcal{M}$ for $\lambda = 0.35$ [$\lambda = 0.75$]. The approximate region achieved in our experiment is shown in yellow. Improvements in both η and $\mathcal{M}$ are necessary to unconditionally surpass the shot-noise limit. As a reference point, a distinguishability of $\mathcal{M} \sim 0.85$ was achieved in Ref. [222] using the same type of high-gain PDC sources as used in our experiment. With such a distinguishability, the efficiency would need to be improved to $\sim 70\%$ [$\sim 80\%$] when using $\lambda = 0.35$ [$\lambda = 0.75$].

Finally, we note that although we do not attain these parameters in our experiment, our results do demonstrate the robustness of our probes to losses despite their large size. For example, the Fisher information per photon calculated without post-selection for the $N = 8$ probe with $\Delta = 6$ [Fig. 5.6(a)] is slightly higher than that of the $N = 2$ N00N state [Fig. 5.5(a)]. This contradicts the usual expectation that large entangled probes will necessarily be more fragile to noise and loss.

5.4 Conclusions

In summary, we proposed and experimentally demonstrated a scheme for quantum-enhanced interferometry that exploits high-gain two-mode squeezed vacuum sources and photon-number-resolving detectors. We measured interference fringes involving up to 16 photons which is significantly higher than the previous state-of-the-art [224, 227]. Crucially, our scheme prepares probes that are nearly optimally robust to losses and hence addresses one of the principal challenges when scaling-up to large entangled photonic states. With further improvements in the quality (i.e. coupling efficiency into optical fiber and purity) of bright two-mode squeezed vacuum sources compatible with transition edge sensors [228, 229], we believe our loss-tolerant scheme provides a promising route towards achieving an appreciable advantage over the shot-noise limit using entangled photonic states.

Chapter 6

Summary and outlook

This thesis presented three projects that developed strategies for characterizing and preparing quantum states of light using photon-number-resolving detectors.

In the first project, we built a weak-field homodyne detector that can fully tune between performing photon counting and quadrature measurements. We demonstrated this tunability experimentally with nonclassical signals containing up to 11 photons and determined the minimum local oscillator strength needed to perform quadrature measurements. We also performed a proof-of-principle demonstration of state engineering using the weak-field homodyne detector.

In the second project, we further theoretically investigated the state engineering capabilities of weak-field homodyne. In doing so, we developed a scheme for heralding a wide range of definite parity states, including two- and four-component Schrödinger cat states.

Finally, we considered a specific application of nonclassical states of light which is quantum-enhanced interferometry. We proposed a scheme that exploits the capabilities of photon-number-resolving detectors and high-gain sources of squeezed vacuum. Although our experimentally achieved precision did not unconditionally surpass the shot-noise limit, we increased the size of the entangled states inside the interferometer compared to previous works and demonstrated that these states are robust to losses despite their larger size. Our proposed scheme will enable quantum-enhanced interferometry with large entangled states if the heralding efficiency and purity of the squeezed vacuum source can be improved.

One of the themes in this thesis has been scaling quantum optics experiments to larger photon numbers, e.g. developing a scheme to prepare Schrödinger cats of higher amplitude and increasing the size of the entangled states for quantum-enhanced interferometery. This scaling is enabled by two technologies: high-gain sources of squeezed vacuum such as the KTP waveguides and transition edge sensors. Our experiments were mostly limited by the heralding efficiency and purity of the squeezed vacuum sources rather than by the detectors. This points towards a need to develop squeezed vacuum sources compatible with transition edge sensors that simultaneously achieve high modal purity, efficiency, and squeezing. Efforts are underway to improve pulsed sources, e.g. by developing ridge waveguides [92]. However, it should be noted that improving such sources is a challenging task due to unwanted effects caused by the large intensities of pulsed light [230]. In fact, there have not been substantial improvements in measured pulsed squeezing levels since the 5.8 dB obtained in Ref. [231] in 1994. In the short term, it could be fruitful to interface transition edge sensors with continuous-wave sources of squeezed vacuum (e.g. as in Ref. [229]) as these currently perform better than pulsed sources in terms of squeezing and efficiency [232, 233].

Appendix A

Marginal photon statistics of a spectrally correlated two-mode squeezed vacuum source

Here we derive the photon statistics of the signal or idler mode of a spectrally correlated two-mode squeezed vacuum source. The state of the signal or idler mode produced by such a source is obtained by tracing over either mode in Eq. (2.12) and is given by:

$$\hat{\rho} = \bigotimes_{k=0}^{\infty} \sqrt{1-\lambda_k^2} \sum_{n_k=0}^{\infty} \lambda_k^{2n_k} |n_k\rangle \langle n_k| \tag{A.1}$$

where k denotes a spectral mode. As a reminder, $\langle n_k \rangle = \lambda_k^2/(1-\lambda_k^2)$ (where $\lambda_k = \tanh(c_k\zeta)$) is the average number of photons in the kth mode, and $K = \left(\sum_k |c_k|^4\right)^{-4}$ is the Schmidt number which determines the effective number of modes. We will assume that c_k is small for $k > K$ and truncate the product state above at $k = K$.

Each spectral mode k has thermal photon statistics, i.e. $\mathrm{pr}_k(n) = \mathrm{Tr}_k(\hat{\rho} |n_k\rangle \langle n_k|) = (1-\lambda_k^2)\lambda_k^{2n}$. However, photodetectors such as transition edge sensors cannot resolve between the different spectral modes. As such, the measured photon statistics $\mathrm{pr}(n)$ are a convolution of the statistics of every spectral mode:

$$\mathrm{pr}(n) = \sum_{\Theta \in n \vdash K} \prod_{k=0}^{K} (1-\lambda_k^2)\lambda_k^{2\Theta}. \tag{A.2}$$

where Θ is a variable defined to perform the convolution: $n \vdash K$ is the set of all partitions of n photons in K modes [234].

Generally, Eq. (A.2) is difficult to evaluate. However, if $\langle n_k \rangle$ (and hence λ_k) is equal in all modes, then the convolution takes a simple form. Firstly, we re-write Eq. (A.2) in terms of $\langle n_k \rangle$ using the fact that $\lambda_k^2 = \langle n_k \rangle / (1 + \langle n_k \rangle)$ and obtain:

$$\mathrm{pr}(n) = \sum_{\Theta \in n \vdash K} \prod_{k=0}^{K} \frac{1}{(1 + \langle n_k \rangle)(1 + 1/\langle n_k \rangle)^{\Theta}}. \tag{A.3}$$

Since $\langle n_k \rangle$ is independent of K, the total average photon-number is $\langle n \rangle = K \langle n_k \rangle$ and we get:

$$\mathrm{pr}(n) = \sum_{\Theta \in n \vdash K} \frac{1}{(1 + \langle n \rangle / K)^{K} (1 + K/\langle n \rangle)^{K\Theta}}. \tag{A.4}$$

On average, the n measured photons are equally partitioned across the K modes, i.e. there are n_k photons in each mode where $n = K n_k$. Using this fact and some combinatorics, the above sum can be evaluated (see page 680 of Ref. [235]) to arrive at the result:

$$\mathrm{pr}(n) = \frac{(n + K - 1)!}{(K - 1)! n!} \frac{1}{(1 + \langle n \rangle / K)^{K} (1 + K/\langle n \rangle)^{n}}, \tag{A.5}$$

which describes a multi-mode thermal distribution with K modes and mean photon number $\langle n \rangle$, where we assumed each mode had equal mean photon-number.

The variance of Eq. (A.5) is evaluated in Ref. [235] and is given by:

$$\begin{aligned} \langle (\Delta n)^2 \rangle &= \sum_{n=0}^{\infty} \mathrm{pr}(n)(n - \langle n \rangle)^2 \\ &= \langle n \rangle \left(1 + \frac{\langle n \rangle}{K} \right). \end{aligned} \tag{A.6}$$

In the limit $K \to \infty$, $\langle (\Delta n)^2 \rangle = \langle n \rangle$ and hence the photon statistics $\mathrm{pr}(n)$ are Poissonian. We can also evaluate the normalized second-order correlation function:

$$\begin{aligned} g^{(2)} &= 1 + \frac{\langle (\Delta n)^2 \rangle - \langle n \rangle}{\langle n \rangle^2} \\ &= 1 + \frac{1}{K} \end{aligned} \tag{A.7}$$

which is directly related to the number of spectral modes K.

Appendix B

Detailed model for weak-field homodyne difference statistics

Here we expand the idealized model described in Sec. 3.3.1. We start by considering the effect of mode mismatch (e.g. spatial, temporal, spectral, and polarization mismatch) between the signal $\hat{\rho}_a$ and phase reference $|\alpha_b\rangle$. In principle, both $\hat{\rho}_a$ and $|\alpha_b\rangle$ can occupy several spatio-temporal modes, thus making a full treatment of mode mismatch quite involved [236]. However, we found that the simpler approach of decomposing the problem into two effective orthogonal modes is sufficient to model our data. This sort of heuristic model has been used and studied elsewhere, see e.g. Refs. [160, 237]. Through a Gram-Schmidt process, $|\alpha_b\rangle$ can be decomposed in the following way [238]:

$$|\alpha_b\rangle \rightarrow |\sqrt{\mathcal{M}}\alpha_{||}\rangle \otimes |\sqrt{1-\mathcal{M}}\alpha_{\perp}\rangle\,, \tag{B.1}$$

where $||$ denotes the same mode as the signal, $\perp$ denotes a mode orthogonal to the signal, and $\mathcal{M} \in [0,1]$ is a mode overlap parameter. Since $|\alpha_b\rangle$ remains a coherent state when it is split across the modes $||$ and $\perp$, its amplitude is simply scaled by $\sqrt{\mathcal{M}}$ and $\sqrt{1-\mathcal{M}}$, respectively. We wish to determine the joint probability of measuring the outcome (m,n) when $\mathcal{M} \neq 1$, i.e. $\mathrm{pr}_{\mathcal{M}}^{(j,\alpha)}(m,n)$. We treat the detector as mode-insensitive, and so we convolve the joint probabilities of measuring the outcome (m,n) in mode $||$ and mode $\perp$:

$$\mathrm{pr}_{\mathcal{M}}^{(j,\alpha)}(m,n) = \mathrm{pr}^{(j,\sqrt{\mathcal{M}}\alpha)}(m,n) * \mathrm{pr}^{(0,\sqrt{1-\mathcal{M}}\alpha)}(m,n), \tag{B.2}$$

where $*$ denotes a convolution operation. The term $\mathrm{pr}^{(j,\sqrt{\mathcal{M}}\alpha)}(m,n)$ is the joint probability of measuring the outcome (m,n) in the mode of the signal $||$. Similarly, the term $\mathrm{pr}^{(0,\sqrt{1-\mathcal{M}}\alpha)}(m,n)$ is the joint probability of measuring the outcome (m,n) in the mode orthogonal to the signal, i.e. $\perp$ (hence the reason why the signal is vacuum in this mode, i.e. $j=0$). Both terms are evaluated using Eq. (3.7).

Next we include the effect of optical loss in all three modes using Eq. (2.1). The joint probability after losses becomes:

$$\mathrm{pr}^{(j,\alpha)}_{\mathcal{M},\eta_h,\eta_c,\eta_d}(m,n) = \sum_{x=m}^{\infty}\sum_{y=n}^{\infty}\sum_{z=j}^{\infty}\binom{z}{j}\binom{x}{m}\binom{y}{n} \times \eta_h^j\eta_c^m\eta_d^n(1-\eta_h)^{z-j}(1-\eta_c)^{x-m}(1-\eta_d)^{y-n}\lambda^{2z}\mathrm{pr}^{(z,\alpha)}_{\mathcal{M}}(x,y). \tag{B.3}$$

The difference photon-number statistics are obtained by summing over all possible combinations of (m,n) resulting in a difference of Δn:

$$\mathrm{pr}^{(j,\alpha)}_{\mathcal{M},\eta_h,\eta_c,\eta_d}(\Delta n) = \sum_{m=\max(0,\Delta n)}^{\infty}\mathrm{pr}^{(j,\alpha)}_{\mathcal{M},\eta_h,\eta_c,\eta_d}(m,m-\Delta n). \tag{B.4}$$

Eq. (B.4) is used to calculate the red lines in Fig. 3.5.

We use a similar approach to generalize the classical field approximation model. The effect of imperfect mode matching is given by

$$p^{(j,\alpha)}_{\mathcal{M}}(\Delta n) = p^{(j,\sqrt{\mathcal{M}}\alpha)}(\Delta n) * p^{(0,\sqrt{1-\mathcal{M}}\alpha)}(\Delta n). \tag{B.5}$$

where $p^{(j,\alpha)}$ is given in Eq. (3.9) where it is referred to as $\mathrm{pr}^{(j,\alpha)}_{\mathrm{classical}}(\Delta n)$ (we switch notation here for convenience). Unlike in the fully quantum model above, the effect of imperfect detection efficiency in the signal modes has a closed expression when the classical field approximation is invoked. In conventional homodyne, detection loss convolves the signal with the difference statistics of the vacuum state. For potentially imbalanced losses, this results in [126]:

$$p^{(j,\alpha)}_{\mathcal{M},\eta_c,\eta_d}(\Delta n) = p^{(j,g)}_{\mathcal{M}}(\Delta\tilde{n}) * \frac{1}{\sqrt{2\pi}\sigma}e^{-\Delta\tilde{n}^2/2\sigma^2}, \tag{B.6}$$

where $g=\eta\alpha$, $\Delta\tilde{n}=\Delta n-\alpha^2(\eta_d-\eta_c)/2$, $\sigma=\sqrt{g^2(1-\eta)/\eta}$, and $\eta=(\eta_c+\eta_d)/2$. Finally, the effect of the imperfect heralding efficiency is treated in the same way as

before:

$$p^{(j,\alpha)}_{\mathcal{M},\eta_h\eta_c,\eta_d}(\Delta n) = \sum_{f=j}^{\infty} \binom{f}{j} \eta_h^j (1-\eta_h)^{f-j} \lambda^{2f} p^{(f,\alpha)}_{\mathcal{M},\eta_c,\eta_d}(\Delta n). \tag{B.7}$$

Eq. (B.7) is used to calculate the blue regions in Fig. 3.5.

The efficiencies and parametric gain values for both the classical and quantum models were determined using the Klyshko measurement described in Sec. 2.3.3. The values are: $\eta_h = 0.395 \pm 0.002$, $\eta_c = 0.274 \pm 0.001$, $\eta_d = 0.352 \pm 0.002$, $\lambda = 0.797 \pm 0.001$. The mode overlap value, $\mathcal{M} = 0.82$, was determined from the visibility of an interference signal (see Sec. 3.3.2).

Appendix C

Model for interference rates

Here we describe the model $\tilde{\mathrm{pr}}(s_1, s_2, h_1, h_2, \phi)$ used to fit the experimentally measured rates. We model optical loss by placing fictitious beam splitters (see Fig. C.1) and tracing over the reflected modes. For now, we assume $\eta_{d_1} = \eta_{d_2} = 1$ and will treat the effect of detection losses at the end.

Each source produce s two-mode squeezed vacuum state:

$$|\Psi_i\rangle = \sqrt{1-\lambda_i^2} \sum_{n=0}^{\infty} \lambda_i^n \, |n, n\rangle \,, \tag{C.1}$$

where $i = 1, 2$ represent sources 1 and 2, respectively. The joint photon-number distribution of this two-mode squeezed vacuum state after the losses is given by [Eq. (2.19)]:

$$\tilde{\mathrm{pr}}_i(x, y) = (1-\lambda_i^2) \sum_{n=\max(x,y)}^{\infty} \binom{n}{x} \binom{n}{y} \lambda_i^{2n} \eta_{h_i}^x \eta_{s_i}^y (1-\eta_{h_i})^{n-x} (1-\eta_{s_i})^{n-y}. \tag{C.2}$$

In principle, n can range up to ∞, but in practice it suffices to truncate this sum at

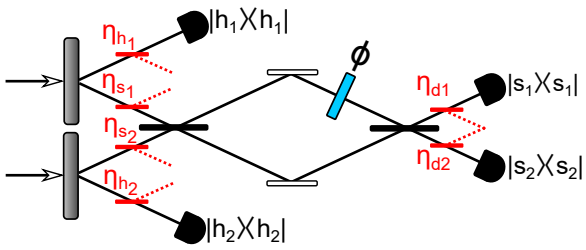

Figure C.1: Losses are modelled by placing fictitious beam splitters in all four modes. The coefficients in red show the transmission of the beam splitters, i.e. the efficiency of the mode.

some value where $(1-\lambda_i)^2\lambda_i^{2n}$ becomes small. In our numerics, we truncate the sum at $n = 50$.

If we obtain the herald outcome (h_1, h_2), then the unnormalized state that is injected into the interferometer is given by:

$$\hat{\rho} = \sum_{m,n=0}^{\infty} \tilde{\mathrm{pr}}_1(h_1, m)\tilde{\mathrm{pr}}_2(h_2, n) \left|m, n\right\rangle \left\langle m, n\right| . \tag{C.3}$$

Losses occurring inside the interferometer can be absorbed into η_s or η_d if they are equal in both interferometer modes, which was approximately the case in our experiment. Thus, the interferometer transformation can be described by a unitary operator $\hat{U}(\phi)$ which depends on the phase difference ϕ between both arms. The probability that we wish to calculate is given by:

$$\tilde{\mathrm{pr}}(s_1, s_2, h_1, h_2, \phi) = \langle s_1, s_2|\hat{U}(\phi)\hat{\rho}\hat{U}^\dagger(\phi)|s_1, s_2\rangle . \tag{C.4}$$

Knowing that there are a total of $s_1 + s_2$ photons before the interferometer, we can constrain $n = s_1 + s_2 - m$ and truncate the sum at $s_1 + s_2$ in Eq. (C.3). Thus, we obtain:

$$\tilde{\mathrm{pr}}(s_1, s_2, h_1, h_2, \phi) = \sum_{m=0}^{s_1+s_2} \tilde{\mathrm{pr}}_1(h_1, m)\tilde{\mathrm{pr}}_2(h_2, s_1{+}s_2{-}m) \left|\langle s_1, s_2|\hat{U}(\phi)|m, s_1 + s_2 - m\rangle\right|^2 . \tag{C.5}$$

The matrix element $\left|\langle s_1, s_2|\hat{U}(\phi)|m, s_1 + s_2 - m\rangle\right|^2$ is derived in Ref. [8] and is given by:

$$\left|\langle s_1, s_2|\hat{U}(\phi)|m, s_1 + s_2 - m\rangle\right|^2 = \frac{m!(s_1 + s_2 - m)!}{s_1!s_2!}(\sin[\phi/2])^{2(s_1+m)}(\cos[\phi/2])^{2(s_2-m)} \times \left(\sum_{k=0}^{s_1} \binom{s_1}{k}\binom{s_2}{s_2 + k - m}(-1)^k \tan[\phi/2]^{-2k}\right)^2 . \tag{C.6}$$

The model for temporally distinguishable photons follows the same approach as above. While the description below focuses on temporal distinguishability, the same equations are valid to describe distinguishability in any other degree of freedom. We adopt a heuristic approach (e.g. as in Ref [239]) in which the temporal mode of the photons produced in the top source is decomposed into a component completely

indistinguishable ($\|$) to the temporal mode of the bottom source photons as well as a component completely distinguishable ($\perp$). With this decomposition, Eq. C.3 becomes:

$$\begin{aligned}\hat{\rho}^{dist} = \sum_{m,n=0}^{\infty}\sum_{l=0}^{m}\binom{m}{l}\mathcal{M}^l(1-\mathcal{M})^{m-l}\tilde{\text{pr}}_1(h_1,m)\tilde{\text{pr}}_2(h_2,n) \\ \times |l,n\rangle_{\|}\langle l,n|_{\|}\otimes|m-l,0\rangle_{\perp}\langle m-l,0|_{\perp}\,.\end{aligned} \tag{C.7}$$

where $\mathcal{M}\in[0,1]$ is a mode overlap parameter characterizing the distinguishability of the photons. For $\mathcal{M}=0$ ($\mathcal{M}=1$), the photons from top and bottom sources are completely distinguishable (indistinguishable). Since our detectors cannot resolve the time difference between $\perp$ and $\|$, they convolve the probabilities for the photons to have originated from either temporal mode. This measurement is described by the following incoherent sum of projectors:

$$\hat{\Pi} = \sum_{x=0}^{s_1}\sum_{y=0}^{s_2}|s_1-x,s_2-y\rangle_{\|}\langle s_1-x,s_2-y|_{\|}\otimes|x,y\rangle_{\perp}\langle x,y|_{\perp}\,. \tag{C.8}$$

Many of the terms in the sum of Eq. C.8 can be eliminated due to constraints on the photon numbers. For example, a total of $m-l$ photons are produced in mode $\perp$ and so $x+y=m-l$. Moreover, $s_1+s_2=m+n$. After applying these constraints, the final joint probability is given by:

$$\begin{aligned}\tilde{\text{pr}}^{dist}(s_1,s_2,h_1,h_2,\phi) &= \text{Tr}\left(\hat{\Pi}\hat{U}(\phi)\hat{\rho}^{dist}\hat{U}^{\dagger}(\phi)\right) \\ &= \sum_{m=0}^{s_1+s_2}\sum_{l=0}^{m}\sum_{x=\max(0,m-s_2)}^{\min(s_1,m-l)}\binom{m}{l}\mathcal{M}^l(1-\mathcal{M})^{m-l} \\ &\quad\times\tilde{\text{pr}}_1(h_1,m)\tilde{\text{pr}}_2(h_2,s_1+s_2-m) \\ &\quad\times\left|\langle s_1-x,l+s_2-m+x|\hat{U}(\phi)|l,s_1+s_2-m\rangle\right|^2 \\ &\quad\times\left|\langle x,m-l-x|\hat{U}(\phi)|m-l,0\rangle\right|^2.\end{aligned} \tag{C.9}$$

Finally, we can now consider the effect of the losses just before the detectors. These losses can be modelled with a transformation analogous to Eq. (C.2). Applying this transformation on Eq. (C.5), we obtain:

$$\begin{aligned}\tilde{\text{pr}}(s_1,s_2,h_1,h_2,\phi;\eta_{d_1},\eta_{d_2}) = \sum_{j=s_1}^{\infty}\sum_{k=s_2}^{\infty}\binom{j}{s_1}\binom{k}{s_2}\eta_{d_1}^{s_1}\eta_{d_2}^{s_2}(1-\eta_{d_1})^{j-s_1}(1-\eta_{d_1})^{k-s_2} \\ \times\tilde{\text{pr}}(j,k,h_1,h_2,\phi)\end{aligned} \tag{C.10}$$

The same method is used for the distinguishable photons model, i.e. replace $\tilde{\text{pr}}(j,k,h_1,h_2,\phi)$ with $\tilde{\text{pr}}^{dist}(j,k,h_1,h_2,\phi)$ in Eq. (C.10). In our numerics, we truncate the sums in Eq. (C.10) to only include the effect of losing a few photons, which is a good approximation given the high efficiency of our number-resolving detectors.

The equations above are evaluated numerically and fitted to the experimentally measured $\text{pr}(s_1,s_2,h_1,h_2,\phi)$ by varying the fit parameters $\eta_{h_1},\eta_{h_2},\eta_{s_1},\eta_{s_2},\eta_{d_1},\eta_{d_2},\lambda_1,\lambda_2$. Fitting is performed using the Python package lmfit with a least squares method. Note that, for the sake of increasing the speed of the fitting, we used $\mathcal{M}=1$ for all data except in Fig. 5.7(b) where we used $\mathcal{M}=0$. Thus, the fit parameters generally did not correspond to the measured efficiencies and squeezing parameters. Instead, the fitting procedure converged on larger λ values and smaller η values to emulate the effect of imperfect interference (i.e. reduced fringe visibility). We tested the full model (i.e. including $\mathcal{M}$) by fitting a subset of rates measured in the high gain regime and found the fit parameters: $\eta_{h_1}=0.50$, $\eta_{h_2}=0.50$, $\eta_{s_1}=0.61$, $\eta_{s_2}=0.50$, $\eta_{d_1}=0.9$, $\eta_{d_2}=0.99$, $\lambda_1=0.68$, $\lambda_2=0.68$, and $\mathcal{M}=0.73$. These efficiency values are within error to the measured values, and $\mathcal{M}=0.73$ is roughly consistent with the measured $\sim 75\%$ quantum interference visibility of the $(1,1,1,1)$ rate.

Appendix D

Quantum Fisher information of generalized Holland-Burnett states

This derivation was first performed by M.E. Mycroft [240]. We wish to calculate $\mathcal{Q}$ [Eq. (5.5)] for the probe $|\Omega\rangle = \hat{U}_{\rm BS}\,|h_1, h_2\rangle$ where $\hat{U}_{\rm BS}$ is the balanced beam splitter unitary transformation. Let $\hat{a}$ and $\hat{b}$ denote the annihilation operators at the input of the interferometer (i.e. before the beam splitter), while $\hat{c}$ and $\hat{d}$ denote the annihilation operators inside the interferometer. We first calculate $\langle\Omega|\hat{n}_c^2|\Omega\rangle$:

$$\begin{aligned}
\langle\Omega|\hat{n}_c^2|\Omega\rangle &= \langle h_1, h_2|\hat{U}_{\rm BS}^\dagger c^\dagger c c^\dagger c\,\hat{U}_{\rm BS}|h_1, h_2\rangle \\
&= \langle h_1, h_2|\left(\hat{U}_{\rm BS}^\dagger c^\dagger \hat{U}_{\rm BS}\,\hat{U}_{\rm BS}^\dagger c \hat{U}_{\rm BS}\right)^2|h_1, h_2\rangle \\
&= \langle h_1, h_2|\left(\frac{a^\dagger + b^\dagger}{\sqrt{2}}\right)^2\left(\frac{a+b}{\sqrt{2}}\right)^2|h_1, h_2\rangle \\
&= \frac{1}{4}\langle h_1, h_2|(a^\dagger + b^\dagger)^2(a+b)^2|h_1, h_2\rangle \\
&= \frac{1}{4}\langle h_1, h_2|a^\dagger a a^\dagger a + b^\dagger b b^\dagger b + 4a^\dagger a b^\dagger b + a^\dagger a + b^\dagger b|h_1, h_2\rangle \\
&= \frac{1}{4}(h_1^2 + h_2^2 + 4h_1h_2 + h_1 + h_2).
\end{aligned} \tag{D.1}$$

We then calculate $\langle\Omega|\hat{n}_c\hat{n}_d|\Omega\rangle$ in a similar manner:

$$\begin{aligned}
\langle\Omega|\hat{n}_c\hat{n}_d|\Omega\rangle &= \langle h_1, h_2|\hat{U}_{\rm BS}^\dagger c^\dagger c d^\dagger d\hat{U}_{\rm BS}|h_1, h_2\rangle \\
&= \langle h_1, h_2|\left(\frac{a^\dagger + b^\dagger}{\sqrt{2}}\right)\left(\frac{a+b}{\sqrt{2}}\right)\left(\frac{a^\dagger - b^\dagger}{\sqrt{2}}\right)\left(\frac{a-b}{\sqrt{2}}\right)|h_1, h_2\rangle \\
&= \frac{1}{4}\langle h_1, h_2|(a^\dagger a + b^\dagger a + b a^\dagger + b^\dagger b)(a^\dagger a - b^\dagger a - b a^\dagger + b^\dagger b)|h_1, h_2\rangle \\
&= \frac{1}{4}\langle h_1, h_2|a^\dagger a a^\dagger a + b^\dagger b b^\dagger b - a^\dagger a - b^\dagger b|h_1, h_2\rangle \\
&= \frac{1}{4}(h_1^2 + h_2^2 - h_1 - h_2).
\end{aligned} \tag{D.2}$$

Finally, we evaluate $\mathcal{Q}$ using Eq. (5.5) and the fact that $\langle \hat{n}_c \rangle = \langle \hat{n}_d \rangle$:

$$\begin{aligned} \mathcal{Q} &= 2\left(\langle \hat{n}_c^2 \rangle - \langle \hat{n}_c \hat{n}_d \rangle\right) \\ &= \frac{1}{2}(4h_1h_2 + 2h_1 + 2h_2) \\ &= 2h_1h_2 + h_1 + h_2. \end{aligned} \tag{D.3}$$

Bibliography

[1] M. Planck, Ann. Phys. **309**, 553 (1901).

[2] A. Einstein, Ann. Phys. **322**, 132 (1905).

[3] C. Gerry and P. Knight, *Introductory Quantum Optics* (Cambridge University Press, 2004).

[4] R. J. Glauber, Phys. Rev. **130**, 2529 (1963).

[5] R. J. Glauber, Phys. Rev. **131**, 2766 (1963).

[6] E. C. G. Sudarshan, Phys. Rev. Lett. **10**, 277 (1963).

[7] E. Wolf, *Introduction to the Theory of Coherence and Polarization of Light* (Cambridge University Press, 2007).

[8] U. Leonhardt, *Essential quantum optics: from quantum measurements to black holes* (Cambridge University Press, 2010).

[9] A. Kenfack and K. Życzkowski, J. Opt. B: Quantum Semiclass. Opt. **6**, 396 (2004).

[10] S. L. Braunstein and P. van Loock, Rev. Mod. Phys. **77**, 513 (2005).

[11] C. Weedbrook, S. Pirandola, R. García-Patrón, N. J. Cerf, T. C. Ralph, J. H. Shapiro, and S. Lloyd, Rev. Mod. Phys. **84**, 621 (2012).

[12] S. Lloyd and S. L. Braunstein, Phys. Rev. Lett. **82**, 1784 (1999).

[13] R. Raussendorf, D. E. Browne, and H. J. Briegel, Phys. Rev. A **68**, 022312 (2003).

[14] H. J. Kimble, M. Dagenais, and L. Mandel, Phys. Rev. Lett. **39**, 691 (1977).

[15] P. Michler, A. Kiraz, C. Becher, W. Schoenfeld, P. Petroff, L. Zhang, E. Hu, and A. Imamoglu, Science **290**, 2282 (2000).

[16] C. Kurtsiefer, S. Mayer, P. Zarda, and H. Weinfurter, Phys. Rev. Lett. **85**, 290 (2000).

[17] S. Haroche, Rev. Mod. Phys. **85**, 1083 (2013).

[18] D. J. Wineland, Rev. Mod. Phys. **85**, 1103 (2013).

[19] B. Hacker, S. Welte, S. Daiss, A. Shaukat, S. Ritter, L. Li, and G. Rempe, Nat. Photonics **13**, 110 (2019).

[20] R. W. Boyd, *Nonlinear optics* (Elsevier, 2003).

[21] M. S. Kim, W. Son, V. Bužek, and P. L. Knight, Phys. Rev. A **65**, 032323 (2002).

[22] Y. I. Bogdanov, K. G. Katamadze, G. V. Avosopiants, L. V. Belinsky, N. A. Bogdanova, A. A. Kalinkin, and S. P. Kulik, Phys. Rev. A **96**, 063803 (2017).

[23] M. Dakna, T. Anhut, T. Opatrný, L. Knöll, and D.-G. Welsch, Phys. Rev. A **55**, 3184 (1997).

[24] C. K. Hong and L. Mandel, Phys. Rev. Lett. **56**, 58 (1986).

[25] N. Quesada, L. G. Helt, J. Izaac, J. M. Arrazola, R. Shahrokhshahi, C. R. Myers, and K. K. Sabapathy, Phys. Rev. A **100**, 022341 (2019).

[26] D. Su, C. R. Myers, and K. K. Sabapathy, Phys. Rev. A **100**, 052301 (2019).

[27] T. Gerrits, S. Glancy, T. S. Clement, B. Calkins, A. E. Lita, A. J. Miller, A. L. Migdall, S. W. Nam, R. P. Mirin, and E. Knill, Phys. Rev. A **82**, 031802 (2010).

[28] K. T. McCusker and P. G. Kwiat, Phys. Rev. Lett. **103**, 163602 (2009).

[29] T. J. Bartley, G. Donati, J. B. Spring, X.-M. Jin, M. Barbieri, A. Datta, B. J. Smith, and I. A. Walmsley, Phys. Rev. A **86**, 043820 (2012).

[30] R. J. Birrittella, M. El Baz, and C. C. Gerry, J. Opt. Soc. Am. B **35**, 1514 (2018).

[31] M. Eaton, R. Nehra, and O. Pfister, New J. Phys. **21**, 113034 (2019).

[32] A. Migdall, S. V. Polyakov, J. Fan, and J. C. Bienfang, *Single-photon generation and detection: physics and applications* (Academic Press, 2013).

[33] G. Zambra, M. Bondani, A. S. Spinelli, F. Paleari, and A. Andreoni, Rev. Sci. Instrum. **75**, 2762 (2004).

[34] M. Bondani, A. Allevi, A. Agliati, and A. Andreoni, J. Mod. Opt. **56**, 226 (2009).

[35] D. Achilles, C. Silberhorn, C. Śliwa, K. Banaszek, and I. A. Walmsley, Opt. Lett. **28**, 2387 (2003).

[36] M. J. Fitch, B. C. Jacobs, T. B. Pittman, and J. D. Franson, Phys. Rev. A **68**, 043814 (2003).

[37] L. A. Jiang, E. A. Dauler, and J. T. Chang, Phys. Rev. A **75**, 062325 (2007).

[38] K. Yamamoto, K. Yamamura, K. Sato, T. Ota, H. Suzuki, and S. Ohsuka, in *2006 IEEE Nuclear Science Symposium Conference Record*, Vol. 2 (IEEE, 2006) pp. 1094–1097.

[39] E. Waks, K. Inoue, W. D. Oliver, E. Diamanti, and Y. Yamamoto, IEEE J. Sel. Top. Quantum Electron. **9**, 1502 (2003).

[40] E. Waks, E. Diamanti, B. C. Sanders, S. D. Bartlett, and Y. Yamamoto, Phys. Rev. Lett. **92**, 113602 (2004).

[41] L. Pezzé, A. Smerzi, G. Khoury, J. F. Hodelin, and D. Bouwmeester, Phys. Rev. Lett. **99**, 223602 (2007).

[42] M. Fujiwara and M. Sasaki, Opt. Lett. **31**, 691 (2006).

[43] M. Fujiwara and M. Sasaki, Appl. Opt. **46**, 3069 (2007).

[44] M. A. Rowe, E. Gansen, M. Greene, R. Hadfield, T. Harvey, M. Su, S. W. Nam, R. Mirin, and D. Rosenberg, App. Phys. Lett **89**, 253505 (2006).

[45] E. Gansen, M. A. Rowe, M. Greene, D. Rosenberg, T. E. Harvey, M. Su, R. Hadfield, S. W. Nam, and R. P. Mirin, Nat. Photonics **1**, 585 (2007).

[46] A. Divochiy, F. Marsili, D. Bitauld, A. Gaggero, R. Leoni, F. Mattioli, A. Korneev, V. Seleznev, N. Kaurova, O. Minaeva, *et al.*, Nat. Photonics **2**, 302 (2008).

[47] C. Cahall, K. L. Nicolich, N. T. Islam, G. P. Lafyatis, A. J. Miller, D. J. Gauthier, and J. Kim, Optica **4**, 1534 (2017).

[48] K. L. Nicolich, C. Cahall, N. T. Islam, G. P. Lafyatis, J. Kim, A. J. Miller, and D. J. Gauthier, Phys. Rev. Appl. **12**, 034020 (2019).

[49] J. Gao, M. Vissers, M. Sandberg, F. Da Silva, S. W. Nam, D. Pappas, D. Wisbey, E. Langman, S. Meeker, B. Mazin, *et al.*, Appl. Phys. Lett. **101**, 142602 (2012).

[50] W. Guo, X. Liu, Y. Wang, Q. Wei, L. Wei, J. Hubmayr, J. Fowler, J. Ullom, L. Vale, M. Vissers, *et al.*, Appl. Phys. Lett. **110**, 212601 (2017).

[51] A. E. Lita, A. J. Miller, and S. W. Nam, Opt. Express **16**, 3032 (2008).

[52] D. Fukuda, G. Fujii, T. Numata, K. Amemiya, A. Yoshizawa, H. Tsuchida, H. Fujino, H. Ishii, T. Itatani, S. Inoue, *et al.*, IEEE Trans. Appl. Supercond. **21**, 241 (2010).

[53] G. Brida, L. Ciavarella, I. P. Degiovanni, M. Genovese, L. Lolli, M. G. Mingolla, F. Piacentini, M. Rajteri, E. Taralli, and M. G. Paris, New J. Phys. **14**, 085001 (2012).

[54] L. Lolli, E. Taralli, and M. Rajteri, J. Low Temp. Phys. **167**, 803 (2012).

[55] P. C. Humphreys, B. J. Metcalf, T. Gerrits, T. Hiemstra, A. E. Lita, J. Nunn, S. W. Nam, A. Datta, W. S. Kolthammer, and I. A. Walmsley, New J. Phys. **17**, 103044 (2015).

[56] M. Jönsson and G. Björk, Phys. Rev. A **99**, 043822 (2019).

[57] K. Irwin, Appl. Phys. Lett. **66**, 1998 (1995).

[58] B. Cabrera, R. Clarke, A. Miller, S. W. Nam, R. Romani, T. Saab, and B. Young, Physica B Condens. Matter **280**, 509 (2000).

[59] B. J. Metcalf, *Silica-on-silicon waveguide circuits and superconducting detectors for integrated quantum information processing*, Ph.D. thesis, University of Oxford (2014).

[60] G. Turin, IEEE Trans. Inf. Theory **6**, 311 (1960).

[61] E. Figueroa-Feliciano, B. Cabrera, A. Miller, S. Powell, T. Saab, and A. Walker, Nucl. Instrum. Methods Phys. Res **444**, 453 (2000).

[62] M. O. Scully and W. E. Lamb, Phys. Rev. **179**, 368 (1969).

[63] T. Kiss, U. Herzog, and U. Leonhardt, Phys. Rev. A **52**, 2433 (1995).

[64] A. Eckstein, *Mastering quantum light pulses with nonlinear waveguide interactions*, Ph.D. thesis, Universität Erlangen-Nürnberg, Erlangen (2012).

[65] W. P. Grice and I. A. Walmsley, Phys. Rev. A **56**, 1627 (1997).

[66] W. P. Grice, A. B. U'Ren, and I. A. Walmsley, Phys. Rev. A **64**, 063815 (2001).

[67] P. J. Mosley, J. S. Lundeen, B. J. Smith, P. Wasylczyk, A. B. U'Ren, C. Silberhorn, and I. A. Walmsley, Phys. Rev. Lett. **100**, 133601 (2008).

[68] F. Graffitti, J. Kelly-Massicotte, A. Fedrizzi, and A. M. Brańczyk, Phys. Rev. A **98**, 053811 (2018).

[69] M. Fiorentino, S. M. Spillane, R. G. Beausoleil, T. D. Roberts, P. Battle, and M. W. Munro, Opt. Express **15**, 7479 (2007).

[70] M. M. Weston, H. M. Chrzanowski, S. Wollmann, A. Boston, J. Ho, L. K. Shalm, V. B. Verma, M. S. Allman, S. W. Nam, R. B. Patel, *et al.*, Opt. Express **24**, 10869 (2016).

[71] A. B. U'Ren, C. Silberhorn, K. Banaszek, and I. A. Walmsley, Phys. Rev. Lett. **93**, 093601 (2004).

[72] A. Eckstein, A. Christ, P. J. Mosley, and C. Silberhorn, Phys. Rev. Lett. **106**, 013603 (2011).

[73] W. Wasilewski, A. I. Lvovsky, K. Banaszek, and C. Radzewicz, Phys. Rev. A **73**, 063819 (2006).

[74] N. Quesada and J. E. Sipe, Phys. Rev. A **90**, 063840 (2014).

[75] G. Triginer, M. D. Vidrighin, N. Quesada, A. Eckstein, M. Moore, W. S. Kolthammer, J. E. Sipe, and I. A. Walmsley, Phys. Rev. X **10**, 031063 (2020).

[76] I. Jizan, B. Bell, L. Helt, A. C. Bedoya, C. Xiong, and B. J. Eggleton, Opt. Lett. **41**, 4803 (2016).

[77] J.-P. W. MacLean, J. M. Donohue, and K. J. Resch, Phys. Rev. Lett. **120**, 053601 (2018).

[78] A. O. C. Davis, V. Thiel, M. Karpiński, and B. J. Smith, Phys. Rev. Lett. **121**, 083602 (2018).

[79] M. Liscidini and J. E. Sipe, Phys. Rev. Lett. **111**, 193602 (2013).

[80] A. Valencia, M. V. Chekhova, A. Trifonov, and Y. Shih, Phys. Rev. Lett. **88**, 183601 (2002).

[81] M. Avenhaus, A. Eckstein, P. J. Mosley, and C. Silberhorn, Opt. Lett. **34**, 2873 (2009).

[82] A. Christ, K. Laiho, A. Eckstein, K. N. Cassemiro, and C. Silberhorn, New J. Phys. **13**, 033027 (2011).

[83] M. Avenhaus, K. Laiho, M. V. Chekhova, and C. Silberhorn, Phys. Rev. Lett. **104**, 063602 (2010).

[84] D. Klyshko, Sov. J. Quantum Electron. **10**, 1112 (1980).

[85] A. Worsley, H. Coldenstrodt-Ronge, J. Lundeen, P. Mosley, B. Smith, G. Puentes, N. Thomas-Peter, and I. Walmsley, Opt. Express **17**, 4397 (2009).

[86] A. Ourjoumtsev, R. Tualle-Brouri, and P. Grangier, Phys. Rev. Lett. **96**, 213601 (2006).

[87] E. Bimbard, N. Jain, A. MacRae, and A. I. Lvovsky, Nat. Photonics **4**, 243 (2010).

[88] M. Cooper, L. J. Wright, C. Söller, and B. J. Smith, Opt. Express **21**, 5309 (2013).

[89] J. Tiedau, T. J. Bartley, G. Harder, A. E. Lita, S. W. Nam, T. Gerrits, and C. Silberhorn, Phys. Rev. A **100**, 041802 (2019).

[90] C. K. Hong, Z. Y. Ou, and L. Mandel, Phys. Rev. Lett. **59**, 2044 (1987).

[91] I. Walmsley, Science **358**, 1001 (2017).

[92] C. Eigner, M. Santandrea, L. Padberg, M. F. Volk, C. E. Rüter, H. Herrmann, D. Kip, and C. Silberhorn, Opt. Express **26**, 28827 (2018).

[93] J. Shapiro, H. Yuen, and A. Mata, IEEE Trans. Inf. Theory **25**, 179 (1979).

[94] D. T. Smithey, M. Beck, M. G. Raymer, and A. Faridani, Phys. Rev. Lett. **70**, 1244 (1993).

[95] A. I. Lvovsky and M. G. Raymer, Rev. Mod. Phys. **81**, 299 (2009).

[96] S. L. Braunstein and H. J. Kimble, Phys. Rev. Lett. **80**, 869 (1998).

[97] N. C. Menicucci, P. van Loock, M. Gu, C. Weedbrook, T. C. Ralph, and M. A. Nielsen, Phys. Rev. Lett. **97**, 110501 (2006).

[98] U. Leonhardt and H. Paul, Phys. Rev. A **47**, R2460 (1993).

[99] R. S. Kennedy, Quarterly Progress Report **108**, 219 (1973).

[100] S. J. Dolinar, Research Laboratory of Electronics, MIT, Quarterly Progress Report **11**, 115 (1973).

[101] R. L. Cook, P. J. Martin, and J. M. Geremia, Nature **446**, 774 (2007).

[102] F. Becerra, J. Fan, G. Baumgartner, J. Goldhar, J. Kosloski, and A. Migdall, Nat. Photonics **7**, 147 (2013).

[103] F. Becerra, J. Fan, and A. Migdall, Nat. Photonics **9**, 48 (2015).

[104] A. Royer, Phys. Rev. A **15**, 449 (1977).

[105] S. Deleglise, I. Dotsenko, C. Sayrin, J. Bernu, M. Brune, J.-M. Raimond, and S. Haroche, Nature **455**, 510 (2008).

[106] D. Leibfried, D. M. Meekhof, B. E. King, C. Monroe, W. M. Itano, and D. J. Wineland, Phys. Rev. Lett. **77**, 4281 (1996).

[107] K. Laiho, K. N. Cassemiro, D. Gross, and C. Silberhorn, Phys. Rev. Lett. **105**, 253603 (2010).

[108] G. Harder, C. Silberhorn, J. Rehacek, Z. Hradil, L. Motka, B. Stoklasa, and L. L. Sánchez-Soto, Phys. Rev. Lett. **116**, 133601 (2016).

[109] M. Bohmann, J. Tiedau, T. Bartley, J. Sperling, C. Silberhorn, and W. Vogel, Phys. Rev. Lett. **120**, 063607 (2018).

[110] R. Nehra, A. Win, M. Eaton, N. Sridhar, R. Shahrokhshahi, T. Gerrits, A. Lita, S. W. Nam, and O. Pfister, arXiv preprint arXiv:1906.02093 (2019).

[111] J. Sperling, D. S. Phillips, J. F. F. Bulmer, G. S. Thekkadath, A. Eckstein, T. A. W. Wolterink, J. Lugani, S. W. Nam, A. Lita, T. Gerrits, W. Vogel, G. S. Agarwal, C. Silberhorn, and I. A. Walmsley, Phys. Rev. Lett. **124**, 013605 (2020).

[112] G. Puentes, J. S. Lundeen, M. P. A. Branderhorst, H. B. Coldenstrodt-Ronge, B. J. Smith, and I. A. Walmsley, Phys. Rev. Lett. **102**, 080404 (2009).

[113] L. Zhang, H. B. Coldenstrodt-Ronge, A. Datta, G. Puentes, J. S. Lundeen, X.-M. Jin, B. J. Smith, M. B. Plenio, and I. A. Walmsley, Nat. Photonics **6**, 364 (2012).

[114] G. Donati, T. J. Bartley, X.-M. Jin, M.-D. Vidrighin, A. Datta, M. Barbieri, and I. A. Walmsley, Nat. Commun. **5**, 5584 (2014).

[115] K. Banaszek and K. Wódkiewicz, Phys. Rev. A **58**, 4345 (1998).

[116] P. Grangier, M. J. Potasek, and B. Yurke, Phys. Rev. A **38**, 3132 (1988).

[117] A. Kuzmich, I. A. Walmsley, and L. Mandel, Phys. Rev. Lett. **85**, 1349 (2000).

[118] T. Tyc and B. C. Sanders, J. Phys. A **37**, 7341 (2004).

[119] M. Skotiniotis, W. Dür, and P. Sekatski, Quantum **1**, 34 (2017).

[120] S. D. Bartlett, B. C. Sanders, S. L. Braunstein, and K. Nemoto, Phys. Rev. Lett. **88**, 097904 (2002).

[121] A. Mari and J. Eisert, Phys. Rev. Lett. **109**, 230503 (2012).

[122] N. C. Menicucci, Phys. Rev. Lett. **112**, 120504 (2014).

[123] C. S. Hamilton, R. Kruse, L. Sansoni, S. Barkhofen, C. Silberhorn, and I. Jex, Phys. Rev. Lett. **119**, 170501 (2017).

[124] A. Allevi, M. Bina, S. Olivares, and M. Bondani, Int. J. Quantum Inf **15**, 1740016 (2017).

[125] S. Olivares, A. Allevi, G. Caiazzo, M. G. Paris, and M. Bondani, New J. Phys. **21**, 103045 (2019).

[126] W. Vogel and J. Grabow, Phys. Rev. A **47**, 4227 (1993).

[127] U. Leonhardt, *Measuring the Quantum State of Light* (Cambridge University Press, 1997).

[128] M. C. Tichy, Phys. Rev. A **91**, 022316 (2015).

[129] S. L. Braunstein, Phys. Rev. A **42**, 474 (1990).

[130] U. L. Andersen, J. S. Neergaard-Nielsen, P. van Loock, and A. Furusawa, Nat. Phys. **11**, 713 (2015).

[131] T. Lipfert, J. Sperling, and W. Vogel, Phys. Rev. A **92**, 053835 (2015).

[132] S.-W. Ji, J. Kim, H.-W. Lee, M. S. Zubairy, and H. Nha, Phys. Rev. Lett. **105**, 170404 (2010).

[133] A. I. Lvovsky, Photonics: Scientific Foundations, Technology and Applications **1**, 121 (2015).

[134] C. M. Caves, Phys. Rev. D **23**, 1693 (1981).

[135] E. Schrödinger, Naturwissenschaften **23**, 823 (1935).

[136] M. J. Holland and K. Burnett, Phys. Rev. Lett. **71**, 1355 (1993).

[137] D. Gottesman, A. Kitaev, and J. Preskill, Phys. Rev. A **64**, 012310 (2001).

[138] I. L. Chuang, D. W. Leung, and Y. Yamamoto, Phys. Rev. A **56**, 1114 (1997).

[139] P. W. Shor, Phys. Rev. A **52**, R2493 (1995).

[140] A. M. Steane, Phys. Rev. Lett. **77**, 793 (1996).

[141] Z. Leghtas, G. Kirchmair, B. Vlastakis, R. J. Schoelkopf, M. H. Devoret, and M. Mirrahimi, Phys. Rev. Lett. **111**, 120501 (2013).

[142] M. Mirrahimi, Z. Leghtas, V. V. Albert, S. Touzard, R. J. Schoelkopf, L. Jiang, and M. H. Devoret, New J. Phys. **16**, 045014 (2014).

[143] C. Flühmann, T. L. Nguyen, M. Marinelli, V. Negnevitsky, K. Mehta, and J. P. Home, Nature **566**, 513 (2019).

[144] B. Vlastakis, G. Kirchmair, Z. Leghtas, S. E. Nigg, L. Frunzio, S. M. Girvin, M. Mirrahimi, M. H. Devoret, and R. J. Schoelkopf, Science **342**, 607 (2013).

[145] N. Ofek, A. Petrenko, R. Heeres, P. Reinhold, Z. Leghtas, B. Vlastakis, Y. Liu, L. Frunzio, S. Girvin, L. Jiang, *et al.*, Nature **536**, 441 (2016).

[146] R. A. Campos, B. E. A. Saleh, and M. C. Teich, Phys. Rev. A **40**, 1371 (1989).

[147] J. R. Johansson, P. D. Nation, and F. Nori, Comput. Phys. Commun. **184**, 1234 (2013).

[148] W. Schleich, M. Pernigo, and F. L. Kien, Phys. Rev. A **44**, 2172 (1991).

[149] B. C. Sanders, Phys. Rev. A **45**, 6811 (1992).

[150] J. Wenger, M. Hafezi, F. Grosshans, R. Tualle-Brouri, and P. Grangier, Phys. Rev. A **67**, 012105 (2003).

[151] H. Jeong, W. Son, M. S. Kim, D. Ahn, and C. Brukner, Phys. Rev. A **67**, 012106 (2003).

[152] M. Stobińska, H. Jeong, and T. C. Ralph, Phys. Rev. A **75**, 052105 (2007).

[153] B. Vlastakis, A. Petrenko, N. Ofek, L. Sun, Z. Leghtas, K. Sliwa, Y. Liu, M. Hatridge, J. Blumoff, L. Frunzio, *et al.*, Nat. Commun. **6**, 8970 (2015).

[154] C. Wang, Y. Y. Gao, P. Reinhold, R. W. Heeres, N. Ofek, K. Chou, C. Axline, M. Reagor, J. Blumoff, K. Sliwa, *et al.*, Science **352**, 1087 (2016).

[155] S. J. van Enk and O. Hirota, Phys. Rev. A **64**, 022313 (2001).

[156] H. Jeong, M. S. Kim, and J. Lee, Phys. Rev. A **64**, 052308 (2001).

[157] T. C. Ralph, A. Gilchrist, G. J. Milburn, W. J. Munro, and S. Glancy, Phys. Rev. A **68**, 042319 (2003).

[158] A. Gilchrist, K. Nemoto, W. J. Munro, T. C. Ralph, S. Glancy, S. L. Braunstein, and G. J. Milburn, J. Opt. B: Quantum Semiclass. Opt. **6**, S828 (2004).

[159] A. P. Lund, T. C. Ralph, and H. L. Haselgrove, Phys. Rev. Lett. **100**, 030503 (2008).

[160] A. Ourjoumtsev, R. Tualle-Brouri, J. Laurat, and P. Grangier, Science **312**, 83 (2006).

[161] A. Ourjoumtsev, H. Jeong, R. Tualle-Brouri, and P. Grangier, Nature **448**, 784 (2007).

[162] B. Yurke and D. Stoler, Phys. Rev. Lett. **57**, 13 (1986).

[163] J. Etesse, M. Bouillard, B. Kanseri, and R. Tualle-Brouri, Phys. Rev. Lett. **114**, 193602 (2015).

[164] D. V. Sychev, A. E. Ulanov, A. A. Pushkina, M. W. Richards, I. A. Fedorov, and A. I. Lvovsky, Nat. Photonics **11**, 379 (2017).

[165] G. S. Agarwal and P. K. Pathak, Phys. Rev. A **70**, 053813 (2004).

[166] D. A. Dalvit, R. de Matos Filho, and F. Toscano, New J. Phys. **8**, 276 (2006).

[167] U. Roy, S. Ghosh, P. K. Panigrahi, and D. Vitali, Phys. Rev. A **80**, 052115 (2009).

[168] L. A. Howard, T. J. Weinhold, F. Shahandeh, J. Combes, M. R. Vanner, A. G. White, and M. Ringbauer, Phys. Rev. Lett. **123**, 020402 (2019).

[169] W. H. Zurek, Nature **412**, 712 (2001).

[170] M. Ringbauer, T. J. Weinhold, L. Howard, A. White, and M. Vanner, New J. Phys. **20**, 053042 (2018).

[171] J. Hastrup, J. S. Neergaard-Nielsen, and U. L. Andersen, Opt. Lett. **45**, 640 (2020).

[172] A. L. Grimsmo, J. Combes, and B. Q. Baragiola, Phys. Rev. X **10**, 011058 (2020).

[173] P. A. Knott, T. J. Proctor, A. J. Hayes, J. P. Cooling, and J. A. Dunningham, Phys. Rev. A **93**, 033859 (2016).

[174] H. M. Vasconcelos, L. Sanz, and S. Glancy, Opt. Lett. **35**, 3261 (2010).

[175] T. Eberle, V. Händchen, and R. Schnabel, Opt. Express **21**, 11546 (2013).

[176] H. Vahlbruch, M. Mehmet, K. Danzmann, and R. Schnabel, Phys. Rev. Lett. **117**, 110801 (2016).

[177] Y. Eto, A. Koshio, A. Ohshiro, J. Sakurai, K. Horie, T. Hirano, and M. Sasaki, Opt. Lett. **36**, 4653 (2011).

[178] G. Harder, T. J. Bartley, A. E. Lita, S. W. Nam, T. Gerrits, and C. Silberhorn, Phys. Rev. Lett. **116**, 143601 (2016).

[179] A. A. Michelson, Am. J. Sci. **22**, 120 (1881).

[180] A. A. Michelson and E. W. Morley, Am. J. Sci. **34**, 333 (1887).

[181] B. P. Abbott *et al.*, Phys. Rev. Lett. **116**, 061102 (2016).

[182] V. B. Braginsky, Y. I. Vorontsov, and K. S. Thorne, Science **209**, 547 (1980).

[183] M. Tse *et al.*, Phys. Rev. Lett. **123**, 231107 (2019).

[184] A. Crespi, M. Lobino, J. C. Matthews, A. Politi, C. R. Neal, R. Ramponi, R. Osellame, and J. L. O'Brien, Appl. Phys. Lett. **100**, 233704 (2012).

[185] F. Wolfgramm, C. Vitelli, F. A. Beduini, N. Godbout, and M. W. Mitchell, Nat. Photonics **7**, 28 (2013).

[186] M. A. Taylor, J. Janousek, V. Daria, J. Knittel, B. Hage, H.-A. Bachor, and W. P. Bowen, Nat. Photonics **7**, 229 (2013).

[187] M. A. Taylor and W. P. Bowen, Phys. Rep. **615**, 1 (2016).

[188] V. Cimini, M. Mellini, G. Rampioni, M. Sbroscia, L. Leoni, M. Barbieri, and I. Gianani, Opt. Express **27**, 35245 (2019).

[189] S. L. Braunstein and C. M. Caves, Phys. Rev. Lett. **72**, 3439 (1994).

[190] V. Giovannetti, S. Lloyd, and L. Maccone, Nat. Photonics **5**, 222 (2011).

[191] H. F. Hofmann, Phys. Rev. A **79**, 033822 (2009).

[192] M. Jarzyna and R. Demkowicz-Dobrzański, Phys. Rev. A **85**, 011801 (2012).

[193] M. Napolitano, M. Koschorreck, B. Dubost, N. Behbood, R. Sewell, and M. W. Mitchell, Nature **471**, 486 (2011).

[194] C. M. Caves, Phys. Rev. D **23**, 1693 (1981).

[195] L. Pezzé and A. Smerzi, Phys. Rev. Lett. **100**, 073601 (2008).

[196] P. C. Humphreys, *Experimental and theoretical techniques for quantum-enhanced metrology and optical quantum information processing*, Ph.D. thesis, University of Oxford (2015).

[197] J. J. . Bollinger, W. M. Itano, D. J. Wineland, and D. J. Heinzen, Phys. Rev. A **54**, R4649 (1996).

[198] P. M. Anisimov, G. M. Raterman, A. Chiruvelli, W. N. Plick, S. D. Huver, H. Lee, and J. P. Dowling, Phys. Rev. Lett. **104**, 103602 (2010).

[199] X.-X. Zhang, Y.-X. Yang, and X.-B. Wang, Phys. Rev. A **88**, 013838 (2013).

[200] A. Datta, L. Zhang, N. Thomas-Peter, U. Dorner, B. J. Smith, and I. A. Walmsley, Phys. Rev. A **83**, 063836 (2011).

[201] R. Demkowicz-Dobrzański, M. Jarzyna, and J. Kołodyński, in *Progress in Optics*, Vol. 60 (Elsevier, 2015) pp. 345–435.

[202] M. D. Lang and C. M. Caves, Phys. Rev. Lett. **111**, 173601 (2013).

[203] R. Demkowicz-Dobrzański, K. Banaszek, and R. Schnabel, Phys. Rev. A **88**, 041802 (2013).

[204] U. Dorner, R. Demkowicz-Dobrzanski, B. J. Smith, J. S. Lundeen, W. Wasilewski, K. Banaszek, and I. A. Walmsley, Phys. Rev. Lett. **102**, 040403 (2009).

[205] M. Kacprowicz, R. Demkowicz-Dobrzański, W. Wasilewski, K. Banaszek, and I. Walmsley, Nat. Photonics **4**, 357 (2010).

[206] M. W. Mitchell, J. S. Lundeen, and A. M. Steinberg, Nature **429**, 161 (2004).

[207] P. Walther, J.-W. Pan, M. Aspelmeyer, R. Ursin, S. Gasparoni, and A. Zeilinger, Nature **429**, 158 (2004).

[208] T. Nagata, R. Okamoto, J. L. O'Brien, K. Sasaki, and S. Takeuchi, Science **316**, 726 (2007).

[209] H. Kim, H. S. Park, and S.-K. Choi, Opt. Express **17**, 19720 (2009).

[210] I. Afek, O. Ambar, and Y. Silberberg, Science **328**, 879 (2010).

[211] A. E. Ulanov, I. A. Fedorov, D. Sychev, P. Grangier, and A. Lvovsky, Nat. Commun. **7**, 11925 (2016).

[212] K. J. Resch, K. L. Pregnell, R. Prevedel, A. Gilchrist, G. J. Pryde, J. L. O'Brien, and A. G. White, Phys. Rev. Lett. **98**, 223601 (2007).

[213] N. Thomas-Peter, B. J. Smith, A. Datta, L. Zhang, U. Dorner, and I. A. Walmsley, Phys. Rev. Lett. **107**, 113603 (2011).

[214] S. Slussarenko, M. M. Weston, H. M. Chrzanowski, L. K. Shalm, V. B. Verma, S. W. Nam, and G. J. Pryde, Nat. Photonics **11**, 700 (2017).

[215] J. C. Matthews, X.-Q. Zhou, H. Cable, P. J. Shadbolt, D. J. Saunders, G. A. Durkin, G. J. Pryde, and J. L. O'Brien, npj Quantum Inf. **2**, 1 (2016).

[216] F. Sun, B. Liu, Y. Gong, Y. Huang, Z. Ou, and G. Guo, EPL **82**, 24001 (2008).

[217] G.-Y. Xiang, B. L. Higgins, D. Berry, H. M. Wiseman, and G. Pryde, Nat. Photonics **5**, 43 (2011).

[218] G. Xiang, H. Hofmann, and G. Pryde, Sci. Rep. **3**, 2684 (2013).

[219] R.-B. Jin, M. Fujiwara, R. Shimizu, R. J. Collins, G. S. Buller, T. Yamashita, S. Miki, H. Terai, M. Takeoka, and M. Sasaki, Sci. Rep. **6**, 36914 (2016).

[220] H. Yonezawa, D. Nakane, T. A. Wheatley, K. Iwasawa, S. Takeda, H. Arao, K. Ohki, K. Tsumura, D. W. Berry, T. C. Ralph, H. M. Wiseman, E. H. Huntington, and A. Furusawa, Science **337**, 1514 (2012).

[221] A. A. Berni, T. Gehring, B. M. Nielsen, V. Händchen, M. G. Paris, and U. L. Andersen, Nat. Photonics **9**, 577 (2015).

[222] M. Stobińska, A. Buraczewski, M. Moore, W. Clements, J. J. Renema, S. Nam, T. Gerrits, A. Lita, W. Kolthammer, A. Eckstein, *et al.*, Sci. Adv. **5**, eaau9674 (2019).

[223] J. Flórez, N. J. Carlson, C. H. Nacke, L. Giner, and J. S. Lundeen, Rev. Sci. Instrum. **89**, 023108 (2018).

[224] X.-L. Wang, L.-K. Chen, W. Li, H.-L. Huang, C. Liu, C. Chen, Y.-H. Luo, Z.-E. Su, D. Wu, Z.-D. Li, H. Lu, Y. Hu, X. Jiang, C.-Z. Peng, L. Li, N.-L. Liu, Y.-A. Chen, C.-Y. Lu, and J.-W. Pan, Phys. Rev. Lett. **117**, 210502 (2016).

[225] H. Wang, J. Qin, X. Ding, M.-C. Chen, S. Chen, X. You, Y.-M. He, X. Jiang, L. You, Z. Wang, C. Schneider, J. J. Renema, S. Höfling, C.-Y. Lu, and J.-W. Pan, Phys. Rev. Lett. **123**, 250503 (2019).

[226] S. Daryanoosh, S. Slussarenko, D. Berry, H. Wiseman, and G. Pryde, Nat. Commun. **9**, 2041 (2018).

[227] W.-B. Gao, C.-Y. Lu, X.-C. Yao, P. Xu, O. Gühne, A. Goebel, Y.-A. Chen, C.-Z. Peng, Z.-B. Chen, and J.-W. Pan, Nat. Phys. **6**, 331 (2010).

[228] G. Harder, T. J. Bartley, A. E. Lita, S. W. Nam, T. Gerrits, and C. Silberhorn, Phys. Rev. Lett. **116**, 143601 (2016).

[229] V. Vaidya, B. Morrison, L. Helt, R. Shahrokhshahi, D. Mahler, M. Collins, K. Tan, J. Lavoie, A. Repingon, M. Menotti, *et al.*, arXiv preprint arXiv:1904.07833 (2019).

[230] A. La Porta and R. E. Slusher, Phys. Rev. A **44**, 2013 (1991).

[231] C. Kim and P. Kumar, Phys. Rev. Lett. **73**, 1605 (1994).

[232] A. Schönbeck, F. Thies, and R. Schnabel, Opt. Lett. **43**, 110 (2018).

[233] N. Takanashi, W. Inokuchi, T. Serikawa, and A. Furusawa, Opt. Express **27**, 18900 (2019).

[234] W. Mauerer, M. Avenhaus, W. Helwig, and C. Silberhorn, Phys. Rev. A **80**, 053815 (2009).

[235] L. Mandel and E. Wolf, *Optical coherence and quantum optics* (Cambridge University Press, 1995).

[236] M. G. Raymer, J. Cooper, H. J. Carmichael, M. Beck, and D. T. Smithey, J. Opt. Soc. Am. B **12**, 1801 (1995).

[237] R. Tualle-Brouri, A. Ourjoumtsev, A. Dantan, P. Grangier, M. Wubs, and A. S. Sørensen, Phys. Rev. A **80**, 013806 (2009).

[238] M. C. Tichy, J. Phys. B **47**, 103001 (2014).

[239] P. M. Birchall, J. Sabines-Chesterking, J. L. O'Brien, H. Cable, and J. C. Matthews, arXiv preprint arXiv:1603.00686 (2016).

[240] G. S. Thekkadath, M. E. Mycroft, B. A. Bell, C. G. Wade, A. Eckstein, D. S. Phillips, R. B. Patel, A. Buraczewski, A. E. Lita, T. Gerrits, *et al.*, npj Quantum Inf. **6**, 89 (2020).